Vortices in a Bose-Einstein Condensate

by

Paul C. Haljan

B.Sc.(Hons.), University of Alberta, 1997

A thesis submitted to the
Faculty of the Graduate School of the
University of Colorado in partial fulfillment
of the requirements for the degree of
Doctor of Philosophy
Department of Physics
2003

This thesis entitled:
Vortices in a Bose-Einstein Condensate
written by Paul C. Haljan
has been approved for the Department of Physics

Prof. Eric A. Cornell

Prof. Deborah S. Jin

Date

The final copy of this thesis has been examined by the signatories, and we find that both the content and the form meet acceptable presentation standards of scholarly work in the above mentioned discipline.

Haljan, Paul C. (Ph.D., Physics)

Vortices in a Bose-Einstein Condensate

Thesis directed by Prof. Eric A. Cornell

Since the advent of Bose-Einstein condensation in the dilute alkalis, there has been considerable interest in observing effects in atomic condensates akin to the hallmark effects associated with superfluidity and superconductivity. In particular, the study of quantized vortices and vortex lattices represents an important connection between the traditional "super" systems such as liquid Helium and this new atomic system.

This thesis explores some of the first vortex experiments in a condensate of magnetically trapped Rubidium-87. Single vortex lines and rings are created using a wavefunction engineering technique, which is an ideal starting point to study the dynamical behavior of vortices within the condensate. An entirely different approach of "intrinsic nucleation" has been developed to create rapidly rotating condensates with large amounts of vorticity. A novel variation of forced evaporation is used to simultaneously cool and spin up an ultracold gas. In this way, condensates can be formed that contain large, extraordinarily regular lattices of well over 100 vortices. Direct detection of the vortex cores makes it possible to study the microscopic structure of the vortex arrangements both at equilibrium and under dynamical conditions where severe applied stresses distort the lattice far from its equilibrium configuration.

In conclusion, the techniques developed in this thesis have opened up a new area of rotating condensate physics and, in the future, may lead to regimes of extreme rotation and quantum Hall physics.

Dedication

To my parents and my two brothers, for a level of support that continues to baffle and amaze me.

Acknowledgements

First, I would like to thank my supervisor, Eric Cornell, who more than anyone has been responsible for making my graduate experience a positive one. Fortunate to have been one of his students, I have learnt a tremendous amount about physics and benefited from his teaching, advice and enthusiasm.

Thanks are also due to Carl Wieman and Debbie Jin, who as surrogate supervisors have provided helpful suggestions and advice on topics both scientific and career-related.

I have had the opportunity over the past 5 years to get to know and work with some wonderful people. Jason Ensher, David Hall and Mike Matthews gave me my start in the lab. As I was assuming a senior role in the lab, Brian Anderson arrived. A fantastic postdoc, he taught me a considerable amount of experimental physics. In the past couple of years I have had the privilege of working with another great postdoc Peter Engels and a great graduate student Ian Coddington. Volker Schweikhard recently joined the group and these three guys are already moving far ahead. I'm terribly jealous of the fun experiments they are pursuing! I have learnt a considerable amount from each person and count each one as a colleague and friend; hopefully, I have offered something in return.

The electronics staff, including Paul Beckingham, Mike Whitmore, James Fung-A-Fat and Terry Brown, contributed significantly to this thesis as did the machine shop, in particular Dave Alchenberger, Hans Green and Hans Rohner. Thanks to Pam Leland for all her help. The support staff is why JILA is a fantastic place to work.

A number of theorists have contributed directly to this thesis work. I appreciated the chance to interact personally with Charles Clark, David Feder, Anthony Fetter, Murray Holland, Anatoly Svidzinsky, Sandro Stringari, Jamie Williams, and Francesca Zambelli. Their help and ideas have made the practice of science a pleasure.

Thanks to all the “degenerates” for making the Cornell-Jin-Wieman group such an interesting atmosphere to work in. Thanks especially to Kurt Miller, Heather Lewandowski and Jeremy Richardson for the lunches and study sessions during comprehensives. Those laughs were therapeutic. Thanks to Neil Claussen for a great trip and summer school in Corsica, and Tara Fortier for her friendship through the years. Last of all, thanks to Emily Gibson and Quentin Diot for bolstering me through some tough times at the end.

Finally, I would like to recognize some great teachers who set me on my way and encouraged me early on: John Beamish, John Macdonald and Leo Radzihovsky. Misha Ivanov and Paul Corkum at the NRC in Canada gave me my first gainful physics employment, taught me a great deal of science in two summers and encouraged me to pursue a graduate career. Finally, thanks are due to the NSERC program for helping to fund my doctoral studies.

Contents

Chapter

Figures

Figure

Chapter 1

Introduction

1.1 Bose-Einstein condensation and the “super” systems

The phenomenon of Bose-Einstein condensation(BEC) has a rich history over the past century [155], beginning with the recognition of two classes of particles in nature, bosons and fermions, obeying Bose-Einstein and Fermi-Dirac statistics respectively: In a system of indistiguishable particles, an arbitrary number of bosons may occupy a single quantum state whereas fermions are restricted by the Pauli exclusion principle to a single particle per state. Remarkably, according to the “spin statistics theorem,” particles in nature with integer spin are bosons while those with half-integer spin are fermions. The different particle statistics have fundamental and far-reaching physical consequences; however, effects become evident only at low[1] temperatures where particles gather in the lowest energy states of a system and the average occupation of a state approaches unity. Early in the 1900s, theory by Bose [56] and Einstein [76] predicted that if a gas of ideal(non-interacting) bosons is cooled down, a quantum phase transition will occur at a critical temperature $T = T_C$, below which a macroscopic population “condenses” into the ground state of the system. At $T = 0$, the condensate fraction reaches one. It certainly is not surprising that all the particles end up in the ground state at $T = 0$ since it is the state with the lowest energy. Significantly, however, the macroscopic

---

[1] A “low” temperature is defined relative to the characteristic spacing of a system’s energy levels and need not be low in any particular absolute terms.

occupation persists at finite temperatures up to the critical temperature.

Following the theory of Bose and Einstein, London [115] was the first to suggest that BEC could account for the experimentally observed superfluid transition in liquid ^{4}He, even though the strong interatomic interactions in the liquid clearly put the system far from the concept of an ideal Bose gas. Implicit in this discussion is the fact that ^{4}He, although composed of fermions (electrons, protons, neutrons), is nevertheless a composite boson, the constituent spins of which add up to give a total integer spin. The original motivations of London are not delved into here; instead, some of the relevant consequences are pointed out. In a liquid helium sample, the condensate is associated with the superfluid component. As a macroscopically occupied quantum state, it has an associated wavefunction or order parameter $\Psi = \sqrt{\rho(\vec{r})}e^{i\mathcal{S}(\vec{r})}$. As Tilley points out [155], this fact in itself made London's proposal a bold suggestion. After all, wavefunctions were associated at the time with the microscopic quantum world of atoms but London was suggesting that a continuous wavefunction exists over the scale of a bucket of liquid helium!

Given the existence of an order parameter, currents of the superfluid or "superflows" are associated quantum mechanically with gradients in the phase $\mathcal{S}$. As originally emphasized by Onsager [131] and Feynman [85], this has a direct bearing on the meaning of a rotating quantum fluid. Since the order parameter needs to be single valued, the phase around a closed loop must return on itself or, if there is a hole in the superfluid, it can increment by an integer multiple of 2π. The latter case describes the multiply-connected topology of a superfluid pierced by one or many quantized vortex cores. The connection between quantum mechanical phase and velocity is a rather strong statement permitting rotation to enter a superfluid *only* in the form of quantized vortices. In the "rotating bucket" experiments with liquid helium, a rotating normal fluid is cooled below the superfluid transition. Above a critical rotation rate Ω_C, singly-quantized vortices are nucleated at the edge of the superfluid and migrate inwards. Higher rotation rates lead to the nucleation of more vortices, which come to form stationary arrays in the rotating frame. In 1979, Yarmchuk and Packard [160] reported the direct observation of individual vortex cores in arrays of up to eleven vortices. The visual observation of vortex lattices, together with the quantization of vortex circulation as first demonstrated by Vinen [156], represents one of the hallmarks of superfluidity.

Following superfluid ^{4}He, the list of physical systems exhibiting a macroscopically occupied quantum state grew to include superfluid ^{3}He, superconductors and lasers. The latter two systems have resulted in countless technological advances. In the case of superconductors, conduction electrons pair up to form composite bosons which produce persistent supercurrents, directly analogous to the superflows in liquid Helium II. Magnetic fields play the role of rotation in a superconductor. Thus, above a critical applied magnetic field, Abrikosov lattices of magnetic flux quanta are observed [1], having the same triangular structure predicted for vortex lattices in superfluid ^{4}He.

In 1995, the newest member of the macroscopic quantum states was demonstrated experimentally - BEC in a trapped dilute alkali gas. There are currently in excess of 30 gaseous BEC experiments around the world using several different atoms (Cs, H, He*, Li, K, Na, Rb ...). With a density 10^{-6} less than that of air at STP, a dilute-gas condensate involves interatomic interactions that are relatively weak compared those in helium liquid (although this is an evolving frontier [62]). The result is a theoretical description that is more tractable. The dilute nature of the gas also means that the ground state fraction is large, essentially 100% compared with $\sim$10% in Helium II, where the interactions deplete the ground state [155]. A novel feature in the atomic vapour experiments is the ability to directly see the density profile of the condensate's wavefunction with optical imaging, central in fact to the results of this thesis. For this reason in particular, dilute gas condensation as a visually accessible phenomenon has become synonymous with the concept of ”BEC”.

One of the most interesting (and fun) aspects of atomic BEC is the interplay it has with other areas of physics, be it quantum optics or condensed matter. For example, a significant amount of evidence has been amassed to connect superfluidity in ^{4}He to the phenomenon of Bose-Einstein condensation. One may ask though: is dilute-gas BEC a superfluid? The question is more than just semantics. To answer it, one arguably should demonstrate the canonical experimental properties that *define* superfluidity [114], such as the rotating bucket experiments mentioned above, although the choice of experiments ends up being somewhat subjective. It is useful to try to distill the basic features of a condensate that contribute to its superfluid character. Consider rotation properties specifically. The existence of a macroscopic wavefunction alone leads to the quantization of circulation characteristic of a superfluid; however, equally crucial is the role of repulsive interactions in the condensate since they are responsible for the “persistence” of quantized vortices as stable topological objects in the fluid. Garcia-Ripoll *et al.* [88] refer to this as the “structural stability” of a vortex, which may be understood as follows: A quantized vortex cannot disappear from the condensate wavefunction by “spinning down.” The multiply-connected topology of a wavefunction containing a vortex core, like a rubber sheet with a hole in it, can be destroyed only by cutting the density of the condensate along a radial line from its edge to the vortex core. Since the repulsive interatomic interactions give the condensate a finite compressibility, the suppression of the condensate density along a radial line entails an energy cost. It is this energy cost which makes a quantized vortex a structurally stable topological feature. In the absence of sufficiently strong repulsive interactions, an asymmetry introduced in the condensate’s confining potential would presumably destabilize the vortex [88]. An analogous situation has been experimentally demonstrated for an optical vortex contained in a laser beam propagating in free space [125]. Under an asymmetric perturbation from a cylindrical lens, the optical vortex dynamically inverts its topological charge, which is thus clearly not a stable quantity.

1.2 Rotating Bose-Einstein condensates

This thesis addresses the experimental creation of quantized vortices, from one to many, in a dilute-gas condensate of ^{87}Rb. Concurrent with the results presented here, a number of other experimental groups have also addressed the rotational behaviour of a condensate, including studies of vortices [118, 48, 104, 103, 75] and the measurement of a condensate's non-classical moment of inertia [119, 100]. The overall body of work, both theoretical and experimental, is already sizeable, making rotating condensates its own little sub-field of gaseous BEC.

A general BEC workshop took place at JILA in 1999 near the outset of this thesis work. At the time, there was considerable discussion and uncertainty how a vortex could be nucleated into a condensate. The discussion centered around the analog of the "rotating bucket" experiment for trapped gases. The prime question related to the nature of the energy barrier that a vortex would need to overcome to be nucleated into the condensate. This whole issue was initially circumvented when Williams and Holland proposed a novel way to *directly* create a condensate containing a vortex with wavefunction engineering [159]. Based on earlier experimental work in this group with coupled two-component condensates, the wavefunction engineering technique led to the first creation of a (single) vortex in a dilute-gas condensate [122]. At about the same time, the ENS group was successful at nucleating vortex lattices by stirring the condensate in a deformed confining potential [118]. In very rapid succession, there were results from several groups providing different methods of nucleation and elucidating vortex behaviour. Vortices, it seemed, were "everywhere." In retrospect, it seems strange that there was any uncertainty at all in 1999 about vortex nucleation in a condensate! The field was and continues to be extremely active, which has made it a fascinating area to work in.

The wavefunction engineering technique, with its ability to introduce a vortex into a condensate "artificially" with reproducible initial conditions, has proven to be a useful method to study a wide variety of vortex dynamics in a $T = 0$ condensate [Chapter 3]. Additionally, the technique allows the creation of two-component vortices in which the vortex state is composed of one internal spin state of ^{87}Rb while the core is filled with fluid composed of another simultaneously trapped spin state. The mutually repulsive interaction between the two components opens up the possibility to study vortex dynamics in mixtures of interacting superfluids, where the vortex angular momentum need not be confined to one component.

As a general technique, wavefunction engineering has even been extended to make dark solitons in a condensate. The dark soliton, which is the matter wave equivalent of the optical phenomenon, corresponds to a nodal plane cutting across the condensate and an associated π phase discontinuity. Unlike vortices, solitons are not topological features in the condensate wavefunction. Indeed, after their creation, the solitons are observed to rapidly decay to vortex rings in our spherical trapping geometry. Although interesting in its own right, this decay process can be considered an example of wavefunction engineering whereby an unstable precursor state decays to a desired target state, the vortex ring. This may prove useful in the future for making more complicated topological structures in the condensate.

The vortex work based on wavefunction engineering focused on the "quantum limit" of single vortices in a condensate essentially at zero temperature. The variety of experiments not only provided some interesting vortex physics but, perhaps most importantly, led to the acquisition of a number of experimental techniques for the manipulation and detection of vortices. These techniques have continued to prove useful as the experimental direction has moved from the creation and study of condensates with single vortices to the opposite limit of highly rotating condensates containing large lattices of a hundred or more vortices.

The route to large vortex lattices in a condensate ultimately involves the mechanical addition of angular momentum to the trapped gas, just as for the original liquid helium experiments. Coming full circle with the 1999 workshop, a point of controversy has been the exact nature of the vortex nucleation mechanism, this time in the context of experimental results. The group at ENS and later those at MIT and Oxford have nucleated vortex lattices by directly addressing the condensate with a stirring potential. In this "extrinsic" nucleation technique, the stirring action of the potential has been found to drive surface waves on the condensate to instability. The crests of the waves break, nucleating vortices in the resulting turbulence of the "surf". The approach to vortex nucleation taken in this thesis [Chapter 4] has followed a somewhat different route, which at the time offered the possibility of a different physical mechanism for nucleation. In this new method, an ultracold gas above T_C is first brought into rotation and then evaporatively cooled to quantum degeneracy. Above a critical rotation rate, vortices are nucleated into the condensate. This "intrinsic" nucleation is due only to the interaction of the normal cloud with the condensate since the trapping potential is left static (and rotationally symmetric to conserve angular momentum) throughout the evaporation. After a flurry of discussion in the literature, the nucleation mechanism appears to be due again to surface-wave instabilities, driven not by a rotating trap roughness but instead by thermal fluctuations from the rotating normal cloud.

Nevertheless, a significant benefit of the intrinsic nucleation method is the generation of large amounts of vorticity in a condensate. A key feature of the evaporative technique is that it is designed to simultaneously cool and spin up a trapped gas to higher rotation rates. As a result, highly rotating condensates of a million or more atoms can be formed containing 130 or more singly quantized vortices. They are crystallized in remarkably ordered lattices, spanning ten or more lattice constants across the condensate. In a particular sense, these vortex lattices are very much the opposite of the "quantum" limit of a single vortex. For the large numbers of vortices in the condensate, the correspondence principle would suggest that the rotation field, coarse grained over the vortex structure, should go over to the classical limit of rigid-body rotation. In fact, the condensate does centrifugally distend like a rotating classical gas. From the distortion to the condensate shape, an effective rigid-body rotation rate as high as 95% of the centrifugal limit has be inferred (and this value is rising even higher in current experiments). The large rotation rates and condensate number have been brought to the point of reproducibility that the BEC machine is now truly a *vortex machine*.

The reproducible production of highly rotating condensates containing large, equilibrium vortex lattices is an ideal spring board for a number of different experiments. In the first instance, a study has been made of the non-equilibrium lattice dynamics induced when large amplitude shape deformations are applied to the condensate. The anisotropic stress of the shape deformations induces a variety of strain responses in the vortex lattice including shifting of lattice planes, changes of lattice structure, and the formation of sheet-like structures in which individual vortices appear to have merged.

Finally, it was mentioned above how in presence of large amounts of vorticity a condensate attains the classical limit of rigid-body rotation. However, in the limit of truly extreme rotation rates one approaches what may be called the "true quantum limit" where the amount of vorticity approaches the number of particles within the condensate. Under these circumstances, recent theory [63, 133, 101, 146] predicts the transformation of a condensate from a vortex lattice state to a strongly correlated quantum system, analogous to the quantum Hall regime in condensed matter physics. Given the versatile set of experimental tools that can be brought to bear on the condensate, it is a possibility more than a hope that quantum Hall physics will be accessed in dilute-gas BEC in the near future.

1.3 JILA Mark III: keeps on going, and going ...

Underlying all the physics explored in this thesis is a BEC apparatus, JILA Mark III, originally constructed by previous members of the group as a "next generation" machine [78, 120]. Diode laser technology and a vacuum system without moving parts have made this experiment extraordinarily reliable as far as experiments go. Consider that the glass cells have been under continuous high vacuum since their construction in 1996. The original ^{87}Rb dispenser is still being used with several more available in-chamber. Having a cycle time of $\sim$1min, the machine has produced about a half-million condensates during the time of this thesis and averaged two successful experiments per year. Admittedly, the apparatus has undergone a gradual overhaul with time. Lasers have been changed and several more added. There are now at least as many lasers devoted to manipulating and probing the condensate as there are ones devoted to its production. Although practically every part of the setup has undergone modification, the same basic apparatus underlies it all (if you can still see it under the optics and coils!) Only now is the experiment beginning to suffer from some limitations, particularly in optical access, leaving room for plenty of ingenuity.

Chapter 2

Phase-contrast imaging

2.1 Introduction

A quick look through the JILA theses on atom trapping and cooling shows that every one covers the topic of optical imaging in one way or another; this thesis is no exception. The reason is obvious: essentially all experimental data on an atom cloud derives from images formed by scattering probe laser light off it. Every new imaging technique opens up new experimental possibilities. Phase-contrast imaging [2], allowing the non-destructive measurement of condensate samples *in situ* [52], has proven to be a particularly useful and general technique for our experimental apparatus, especially for the vortex experiments detailed in this thesis. Because phase-contrast imaging has become the workhorse for condensate assay in our experiment, more than the usual detail is devoted here to outlining a proper quantitative model of the technique.

The imaging of an atom cloud can make use of the absorption or refractive index properties of the atoms. For absorptive imaging, spontaneous photon scattering by the atoms leaves a shadow imprint of the cloud on the probe beam: $I = I_0 e^{-D(\vec{r})}$. The optical depth $D(\vec{r})$ gives quantitative access to the density profile of the cloud integrated down the line of sight. There are a number of reasons why absorptive imaging is not particularly useful in-trap. Optical depths for on-resonant probe light ($D_0 \sim 10^2 - 10^3$) far exceed the limitations of imaging setups with a maximum observable optical depth of ~ 3 or so [120]. Detuning the probe from resonance to reduce the optical depth only leads to another problem, image distortions due to lens-like refraction by the atom cloud [120]. From the perspective of non-destructiveness, the average recoil energy of an atom following spontaneous emission ($E_r \sim 45$nK for ^{87}Rb) is comparable to the temperature of Bose-condensed samples and thus results in the loss of the atom from the condensate. Since sample sizes are small ($10^4 - 10^6$ atoms), obtaining an image with good signal-to-noise involves scattering a photon or more per atom. After a single absorption image a condensate will be mostly melted if not blown away.

The alternative to absorption imaging is to use an off-resonant phase-contrast technique sensitive to the phase shift induced by the cloud. A *nondestructive* image is possible because the spontaneous scattering rate Γ dies out more quickly away from resonance than the phase shift ξ. (For a probe detuned δ from resonance, $\Gamma \propto 1/\delta^2$ versus $\xi \propto 1/\delta$). The high on-resonant optical depth D_0 of a trapped condensate in particular allows for large probe detunings that significantly suppress spontaneous scattering while still maintaining a good imaging signal ($\xi \sim D_0/\delta \sim 1$). In the last part of this chapter, the "nondestructive" nature of phase-contrast imaging will be characterized in a little more detail, including the ultimate limit of a quantum nondemolition (QND) measurement for number.

2.2 Phase-contrast technique

To measure the phase shift induced by the atom cloud, an interference technique is needed. One way to do this would be to have an interferometer with the atom cloud in one arm. Phase-contrast imaging, which uses Fourier optics techniques, works in a very similar way. As shown in Figure 2.1, a probe laser beam detuned from resonance is incident on the atom cloud. The cloud acts as a phase object, diffracting (elastically scattering) some of the incident light. In analogy to the interferometer, the unscattered component forms the reference beam while the forward-scattered component carries the object information. The components are collected by an imaging lens and spatially

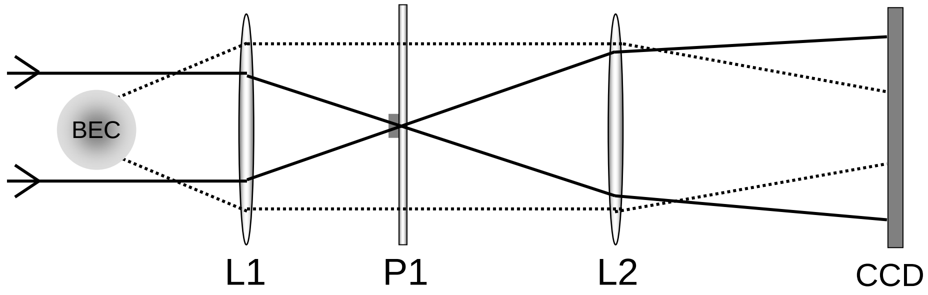

Figure 2.1: Phase-contrast imaging, using imaging lens L1, phase plate P1 in the back Fourier plane of L1 and magnification lens L2. A CCD records the images.

separated in the back focal plane due to the Fourier transforming effect of the lens [143]. This allows a small dielectric dot mounted on a glass substrate to selectively shift the phase of the unscattered component by ϕ_0. A second magnification lens recombines the two light components, which interfere at the image plane to form a phase-contrast image of the atom cloud. A phase dot shift of $\phi_0 = \pi/2$ maximizes the contrast signal for small phase shifts.

The phase plate is a 1/16" thick, 1" diameter glass substrate with a small MgFl_2 dot at the center of one face. The dot, with a diameter of 100μm and a thickness of $\lambda/4(n-1) = 513$nm corresponding to a phase shift of $\pi/2$, was deposited onto the substrate through a thin, stainless steel mask composed of a purchased optical pinhole. The opposite surface of the phase plate was then anti-reflection coated for 780nm to reduce fringes. An issue which arose in the deposition process was the crater-like appearance of the pinhole (due to the laser ablation used in its manufacture). In initial tests, the crater edges resulted in a non-uniform dot, presumably due to shadowing effects. This was solved by carefully polishing the thin steel around the hole to a flat finish.

The diameter of the dot was chosen based on typical condensate and probe beam sizes. The waist size for the probe beam incident on the atom cloud is 1mm compared to 30μm for the condensate radius; therefore, in the Fourier plane of the imaging lens($f \sim$100mm), the focused probe beam is 30μm compared with 1mm for the diffracted light. A 100μm diameter dot is large enough to include most of the focused probe beam, yet small enough to avoid significantly affecting the scattered light.

2.3 3-D imaging

There are a few points of interest relating to our imaging setup. The probe lasers for phase contrast are typically detuned up to several GHz from resonance. Furthermore, the detuning is changed often depending on the signal-to-noise and non-destructiveness desired. External cavity diode lasers with a DAVLL frequency lock [65] provide the versatility for probing both near and far from resonance. A Fabry-Perot cavity is rather useful to monitor the probe frequency relative to the well-defined frequency of a laser under saturation absorption lock [72].

To satisfy our insatiable desire for more and more information, three orthogonal axes of (nondestructive) imaging are simultaneously available to probe an atom cloud (see Fig. 2.2). The horizontal axes share a single CCD array, which is more than large enough to have side-by-side images of the atom cloud. The vertical imaging axis is integrated into an optical path normally occupied by one of the beams used for magneto-optical trapping [78]. As a result, some beam switching is required during the experimental cycle (see Fig. 2.2, side-view). All the complication of assembling a 3-D puzzle of extraordinarily dense optics around a fragile glass vacuum cell is well worth it, as each imaging direction has proven crucial to the vortex experiments discussed in subsequent chapters.

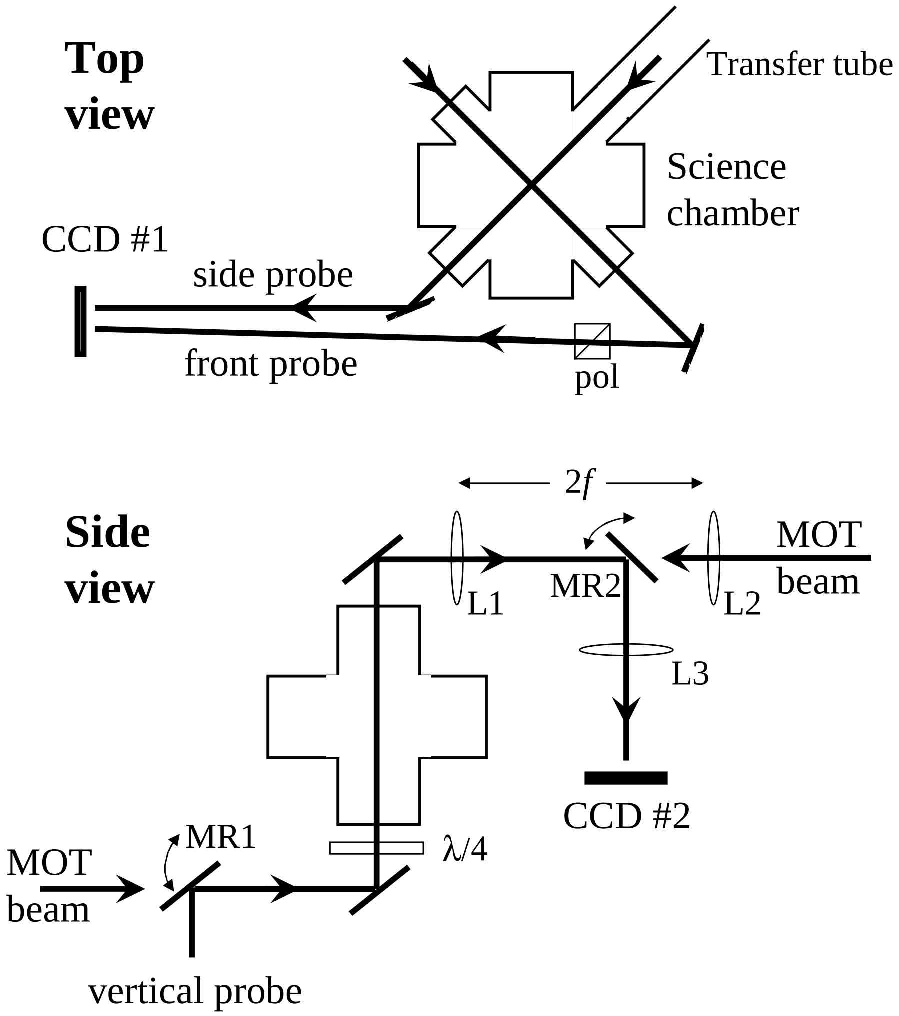

Figure 2.2: Experimental setup for 3-axis imaging. The top view shows the two horizontal imaging axes combined onto a single CCD camera. The more detailed side view shows the vertical axis, which is integrated into a MOT beam path. New Focus flipper mounts MR1 and MR2 rotate into place to permit imaging. Lenses L1 ($f = 120$mm) and L3 ($f = 700$mm) form the vertical imaging microscope. The matched pair of lenses L1 and L2 form a one-to-one telescope for the MOT beam.

2.4 Detailed calculation of imaging process

2.4.1 Overview of calculation

The purpose of this section is to provide a quantitative analysis of phase-contrast imaging, divided into the effect of the atom cloud ("object formation"), the optics ("image formation"), and image processing ("signal inversion"). The only real effort is to calculate the effect of probe laser propagation through the atomic cloud; the rest of the imaging system involves basic Fourier optics and is straight forward. Condensates as well as cold thermal clouds that are fairly dense can be imaged. For the purposes of imaging, a condensate is well approximated as a classical gas of independent quantum absorbers [126], in other words, a dielectric. Therefore, in order to understand object formation we simply need to calculate the refractive index and absorption for a generic atom cloud. The extra twist is that the magnetic confining potential for the atoms provides an ambient bias field that breaks the symmetry of the system. As in anisotropic crystals, the susceptibility of the atom cloud becomes a tensor quantity and the eigenmodes of propagation are no longer the simple free-space ones. As an additional complication, the TOP trap [78] used in this thesis work has a time-varying magnetic bias field which can be oriented in any direction in the horizontal plane. With three axes of imaging having three different polarizations constrained by optical access [Fig. 2.3], it is useful to investigate the effect of the bias field changing during a time-sequence of non-destructive pictures. Finally, in pushing the limits of imaging, for example in the analysis of the shape of an atom cloud, it is also useful to understand any nonlinear behaviour in phase-contrast imaging that will distort the image.

In calculating the optical response of an atom cloud, several references are useful [144, 143, 124] but the information is fairly scattered. Hopefully the expressions and techniques collected here will prove useful for other trapping experiments, including ones using absorption imaging.

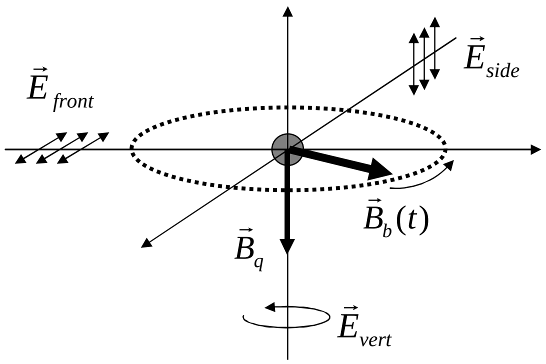

Figure 2.3: Probe polarizations for the three orthogonal axes of imaging. Also shown are the contributions to the magnetic bias field seen by atoms trapped in the TOP trap: (i) the rotating bias field B_b and (ii) a possible static component B_q depending on the position of the atoms in the quadrupole trap.

2.4.2 Atomic susceptibility

The starting point for light propagation in an atom cloud ("the medium") is the Maxwell wave equation in a nonpermeable (zero magnetization) dielectric medium

$$\begin{aligned} \nabla^2\vec{E} - \nabla(\nabla\cdot\vec{E}) - \mu_o\frac{\partial^2}{\partial t^2}\vec{D} &= 0 \\ \nabla\cdot\vec{D} &= 0 \end{aligned} \tag{2.1}$$

where $\vec{D} = \epsilon_0\vec{E} + \vec{\mathcal{P}}$ with $\vec{\mathcal{P}}$ being the induced polarization of the medium, $\vec{E}$ the light's electric field, and ϵ_0 and μ_0 the permittivity and permeability of free space respectively.

The polarization $\vec{\mathcal{P}}(\vec{r},t)$ of an ultracold trapped cloud of atoms (including a condensate) is simply $n(\vec{r})\langle\vec{d}\rangle$, where $n(\vec{r})$ is the number density and $\langle\vec{d}\rangle = -\langle e\vec{r}\rangle$ is the induced dipole moment of a stationary atom in the presence of the probe laser field. Velocity effects are negligible for the trapped clouds in our experiment. Note that the spatial dependence of the polarization arises only from the density distribution.

We want to consider the optical probing of a ^{87}Rb cloud in a particular ground hyperfine state $5S_{1/2}|F, m_F\rangle$. Available transitions are the D1 and D2 lines reaching the $5P_{1/2}$ and $5P_{3/2}$ electronic states respectively. We use the D2 line at $\lambda = 780$nm, with hyperfine structure resolved, as shown in Fig. 2.4. Contributions from all allowed transitions to the upper hyperfine manifold must be included when calculating the dipole response.

We focus on a single pair of states, labeled $\{|g\rangle, |e\rangle\}$ with associated resonant frequency ω_{eg} and linewidth γ. The state $|g\rangle$ ($|e\rangle$) is in the ground(excited) hyperfine manifold.

The incident probe laser with frequency ω has an electric field,

$$\vec{E}(\vec{r},t) = \frac{\vec{E}}{2} e^{i\omega t - ik_0 z} + c.c. \tag{2.2}$$

The steady-state solution for probe durations $\tau \gg 1/\gamma$ is discussed in many places [124, 144]. In the dipole approximation ($e^{ik_0 z} \sim 1$) and the rotating wave approximation ($\omega - \omega_{eg} \ll \omega$), the dipole moment of an atom can be written as

$$\langle \hat{d}(t) \rangle = -\frac{i}{\hbar} \frac{\vec{d}_{ge} \cdot \vec{E}(t)}{\gamma/2 + i\delta_{eg}} \vec{d}_{eg} + c.c. \tag{2.3}$$

where $\delta_{eg} = \omega - \omega_{eg}$ is the detuning and $\vec{d}_{eg}$ is the dipole matrix element $\langle e|\vec{d}|g\rangle$. Saturation effects [124] are justifiably ignored in phase-contrast imaging since probe detunings are many linewidths and probe intensities are low, typically $100 - 200 \mu W/cm^2$ compared to the saturation intensity $I_S = 1.6 mW/cm^2$ for Rubidium.

The main numerator dependence $(\vec{d} \cdot \vec{E})\vec{d}$ of the dipole moment can be reordered as

$$(\vec{d}_{eg}^{\dagger} \vec{E})\vec{d}_{eg} = \vec{d}_{eg}(\vec{d}_{eg}^{\dagger} \vec{E}) = (\vec{d}_{eg}\vec{d}_{eg}^{\dagger})\vec{E} \tag{2.4}$$

where $\vec{d}_{eg}\vec{d}_{eg}^{\dagger}$ is a 3×3 (Hermitian) matrix (as opposed to $\vec{d}_{eg}^{\dagger}\vec{d}_{eg}$, which is a number). This allows us to write the polarization as $\vec{\mathcal{P}} = \overset{\leftrightarrow}{\chi}_{eg} \vec{E}$ where the susceptibility $\overset{\leftrightarrow}{\chi}_{eg}$ is:

$$\overset{\leftrightarrow}{\chi}_{eg} = \frac{-i}{\hbar} \frac{\vec{d}_{eg}\vec{d}_{eg}^{\dagger}}{\gamma/2 + i\delta_{eg}} n(\vec{r}) \tag{2.5}$$

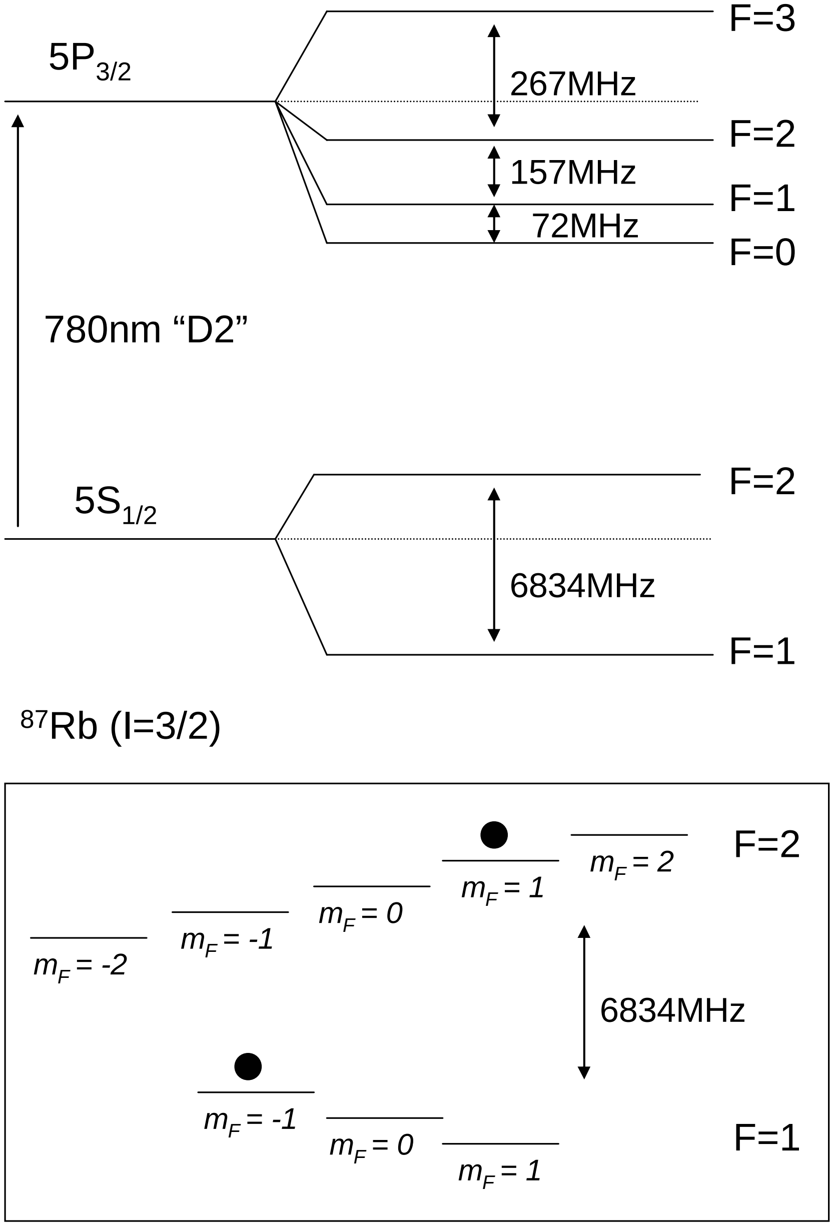

Figure 2.4: Relevant ^{87}Rb level structure showing the D2 optical transition with ground and excited hyperfine manifolds resolved. Also shown in the boxed region is the Zeeman sub-structure for the ground hyperfine states with filled circles identifying the two magnetically trapped states used in the experiment.

To include all hyperfine states $|e\rangle \in |F', m_{F'}\rangle$ in the upper manifold, we sum up their contributions $\overleftrightarrow{\chi}_{eg}$ to the total susceptibility. The dipole decay rate from the upper hyperfine states is γ, independent of $m_{F'}$ sublevel; therefore, the excited state dependence in $\overleftrightarrow{\chi}_{eg}$ is through the detuning and dipole matrix $\vec{d}_{eg}\vec{d}_{eg}^{\dagger}$ only.

It is very useful to define a dipole matrix normalized to the cycling transition matrix element as follows:

$$\overleftrightarrow{C}(e,g) = \frac{\vec{d}_{eg}\vec{d}_{eg}^{\dagger}}{|\vec{d}_{cyc}|^2} \tag{2.6}$$

Thus the net expression for the susceptibility of an atom cloud in ground hyperfine state $|g\rangle$ is:

$$\overleftrightarrow{\chi} = -i \sum_{e \in \{F', m_{F'}\}} \frac{n\sigma}{k_0} \frac{\overleftrightarrow{C}(e,g)}{1 + i\frac{2\delta_{eg}}{\gamma}} \tag{2.7}$$

where the sum is over all excited states $\{|e\rangle\}$. If more than one ground state is occupied, the susceptibility should also be averaged over all of them. The value of σ is the standard crosssection for a cycling transition

$$\sigma = \frac{3\lambda^2}{2\pi} \tag{2.8}$$

In obtaining Eqn. 2.7, the standard relation for the linewidth of a cycling transition was also used

$$\gamma = \frac{\omega^3 |\vec{d}_{cyc}|^2}{3\pi\epsilon_0 \hbar c^3} \tag{2.9}$$

We could express the susceptibility tensor in Cartesian co-ordinates; however, the natural basis to use is the spherical tensor one defined as:

$$\hat{\epsilon}_{\pm} = \mp\frac{1}{\sqrt{2}}(\hat{x} \pm i\hat{y}), \ \hat{\epsilon}_0 = \hat{z} \tag{2.10}$$

If we further choose to use "atom co-ordinates", where the direction of the magnetic bias field lies along the $\hat{z}$-axis, then dipole selection rules cause the $\overleftrightarrow{C}(e,g)$ matrix [Eqn. 2.6] to be diagonal for each of the terms in the susceptibility sum [Eqn. 2.7]. The total susceptibility is, as a result, also diagonal in this basis with value:

$$\overleftrightarrow{\chi} = \begin{pmatrix} \chi_+ & 0 & 0 \\ 0 & \chi_0 & 0 \\ 0 & 0 & \chi_- \end{pmatrix} \tag{2.11}$$

where

$$\chi_q = -i \sum_{e \in \{F', m_{F'}\}} \frac{n\sigma}{k_0} \frac{c_q(e,g)}{1 + i\frac{2\delta_{eg}}{\gamma}} \tag{2.12}$$

The Clebsch-Gordan type terms $c_q(e,g)$ are the diagonal elements of $\overleftrightarrow{C}(e,g)$ in the atom basis [124]:

$$\begin{aligned} c_q(F, m_F; F', m_{F'}) &= \frac{1}{N} \frac{|\hat{\epsilon}_q \cdot \vec{d}_{eg}|^2}{|\vec{d}_{cyc}|^2} \\ &= \frac{1}{N}(2J+1)(2J'+1)(2F+1)(2F'+1) \\ &\quad \times \left| \begin{Bmatrix} L' & J' & S \\ J & L & 1 \end{Bmatrix} \begin{Bmatrix} J' & F' & I \\ F & J & 1 \end{Bmatrix} \begin{pmatrix} F & 1 & F' \\ m_F & q & -m_{F'} \end{pmatrix} \right|^2 \end{aligned} \tag{2.13}$$

The curly-(round-)bracketed terms are 6-j (3-j) symbols, easily evaluated in Mathematica for example. The normalization N is chosen such that $c_q = 1$ for the cycling transition, namely $|2,2\rangle \rightarrow |3,3\rangle$ for ^{87}Rb. The normalized values for the D2 line of ^{87}Rb (I=3/2) can be found listed in a previous thesis [120].

The contribution from each transition to the susceptibility in Eqn. 2.12 may be written as the sum of a real and imaginary part, $\chi'_q(e,g) + i\chi''_q(e,g)$ with values:

$$\begin{aligned} \chi'_q(e,g) &= \frac{2\delta_{eg}}{\gamma} \chi''_q(e,g) \\ \chi''_q(e,g) &= -\frac{n\sigma}{k_0} \frac{c_q(e,g)}{1 + \left(\frac{2\delta_{eg}}{\gamma}\right)^2} \end{aligned} \tag{2.14}$$

where the imaginary part is responsible for absorption and the real part for the refractive index. Clearly for large detunings ($\delta_{eg} \gg \gamma$) the real part dominates.

2.4.3 Object formation

With the polarizability in hand, we can proceed with the effect of light propagation through the atom cloud. Returning to the wave equation [Eqn. 2.1] and assuming a probe laser frequency ω, we obtain an equation for the laser's electric field $\vec{E}(\vec{r})$ inside the medium:

$$\nabla^2 \vec{E} - \nabla(\nabla \cdot \vec{E}) + k^2 \frac{\overleftrightarrow{\epsilon}}{\epsilon_0} \vec{E} = 0 \tag{2.15}$$

where

$$\overleftrightarrow{\epsilon} = \epsilon_0 (1 + \overleftrightarrow{\chi}) \tag{2.16}$$

First, diffraction effects in the atom cloud are neglected, which amounts to dropping all transverse derivatives and keeping only those with respect to the propagation ($\hat{z}$-)direction. To estimate the magnitude of diffraction effects we can use ray-optics and treat the cloud as a sphere of radius R and uniform refractive index. Then the transverse deviation of rays within the cloud is roughly $\Delta x \sim \xi \lambda$ where ξ is the peak phase shift of the probe through the cloud. Typically $\xi \lesssim 1$, so diffraction effects within the cloud do not exceed the imaging resolution ($\gtrsim \lambda$) and are unimportant.

Further, the density of the atom cloud is also assumed to change slowly compared to λ. The laser field can then be approximated as $\vec{E} = \vec{A}(\vec{r}) e^{-ik_0 z}$ where $\vec{A}(\vec{r})$ is slowly varying. Called the paraxial or WKB approximation, this amounts to neglecting reflection by the medium [143].

Incorporating these approximations into the wave equation Eqn. 2.15 and working in the atom co-ordinates where $\overleftrightarrow{\chi}$ (or $\overleftrightarrow{\epsilon}$) is diagonal, we can readily solve for two eigenmodes of propagation $\{\vec{E}_a, \vec{E}_b\}$ in the medium, namely

$$\vec{E}_i(\vec{r}) = \vec{E}_i'(\vec{r}) e^{-i \int^z k_i(\vec{r}') dz'},\ i \in \{a, b\} \tag{2.17}$$

which satisfy the eigenvalue problem,

$$\left(k_0^2 \frac{\overleftrightarrow{\epsilon}(\vec{r})}{\epsilon_0} - k^2 (1 - \hat{z}\hat{z}^\dagger) \right) \vec{E} = 0 \tag{2.18}$$

The spatially dependent eigenvalues $k_{a,b}(\vec{r})$ are determined from a generalized Fresnel equation [143] for a spatially dependent anisotropic medium,

$$\sum_q \frac{|z_q|^2(1+\chi_q(\vec{r}))}{(1+\chi_q(\vec{r}))-\frac{k^2}{k_0^2}}=0 \tag{2.19}$$

where the components χ_q of the susceptibility in the atom frame have already been determined [Eqn. 2.12]. The only difficulty to solving these equations is to calculate the vector components z_q of the propagation direction in terms of the atom-frame spherical co-ordinates. If the magnetic bias field has polar co-ordinates $\{\theta, \phi\}$ with respect to the propagation direction [Figure 2.5], then the transformation from lab to atom co-ordinates is achieved with the rotation operator $\mathcal{D}(\theta,\phi)=\mathcal{D}_y(-\theta)\mathcal{D}_z(-\phi)$ in $l=1$ representation

$$\mathcal{D}(\theta,\phi)=\begin{pmatrix} \frac{1}{2}e^{i\phi}(1+\cos\theta) & \frac{1}{\sqrt{2}}\sin\theta & \frac{1}{2}e^{-i\phi}(1-\cos\theta) \\ -\frac{1}{\sqrt{2}}e^{i\phi}\sin\theta & \cos\theta & \frac{1}{\sqrt{2}}e^{-i\phi}\sin\theta \\ \frac{1}{2}e^{i\phi}(1-\cos\theta) & -\frac{1}{\sqrt{2}}\sin\theta & \frac{1}{2}e^{-i\phi}(1+\cos\theta) \end{pmatrix} \tag{2.20}$$

so that the z-direction in the atom co-ordinates used in equations (2.18) and (2.19) is

$$\hat{z}=\begin{pmatrix} \frac{1}{\sqrt{2}}\sin\theta \\ \cos\theta \\ -\frac{1}{\sqrt{2}}\sin\theta \end{pmatrix} \tag{2.21}$$

Since the $\hat{z}$ components depend only on θ, the same is true of the wavevector and eigenmodes in the atom co-ordinates. The ϕ dependence arises when the eigenvectors are transformed back to the lab co-ordinates with $\mathcal{D}^\dagger(\theta,\phi)$.

Equations (2.17)-(2.21) provide the total solution to propagation in the medium. A probe laser, $\vec{E}_{in}$, is incident on the atom cloud where $\vec{E}_{in}$ is some superposition of the free-space circular polarization basis,

$$\vec{E}_{in}=\begin{pmatrix} E_+ \\ 0 \\ E_- \end{pmatrix} \tag{2.22}$$

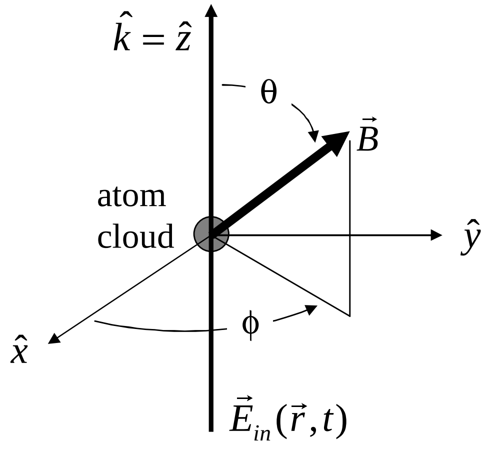

Figure 2.5: Magnetic bias field orientation relative to probe propagation direction $\hat{k} = \hat{z}$.

The output laser field $\vec{E}_{out}$ is obtained as follows:

1)Project $\vec{E}_{in}$ onto the free-space limit of the medium's eigenvectors, which are in lab co-ordinates:

$$\lim_{n\to 0}(\mathcal{D}^\dagger(\theta,\phi)\vec{E}_i) = \begin{pmatrix} E_{i+} \\ 0 \\ E_{i-} \end{pmatrix}, i \in \{a,b\} \tag{2.23}$$

where $|\vec{E}_i|^2 = 1$ and $\mathcal{D}$ is given in Eqn. 2.20.

2)Apply phase shift and absorption to each of the eigenmodes.

3)Reproject (if necessary) onto the free-space circular basis.

In summary, long after the medium we have:

$$\overleftrightarrow{E}_{out} = \left(P^\dagger M P\right) \vec{E}_{in} \tag{2.24}$$

where P is the projection onto the free-space limit of the eigenvectors [Eqn. 2.23] and can be written generally in terms of angles $\{\alpha,\beta\}$

$$P = \begin{pmatrix} E_{a+} & 0 & E_{a-} \\ 0 & 0 & 0 \\ E_{b+} & 0 & E_{b-} \end{pmatrix} \equiv \begin{pmatrix} e^{-i\alpha/2}\cos\beta & 0 & -e^{i\alpha/2}\sin\beta \\ 0 & 0 & 0 \\ e^{-i\alpha/2}\sin\beta & 0 & e^{i\alpha/2}\cos\beta \end{pmatrix} \tag{2.25}$$

M gives the effect of propagation through the medium:

$$M = \begin{pmatrix} e^{-i\xi_a} & 0 & 0 \\ 0 & 0 & 0 \\ 0 & 0 & e^{-i\xi_b} \end{pmatrix} \tag{2.26}$$

with $\xi_{a,b} = \int_{-\infty}^{\infty} (k_{a,b}(\vec{r}) - k_0)\, dz$. The real (imaginary) part of ξ describes the phase shift(absorption) acquired by a probe passing through the cloud.

Although the equations 2.17 & 2.18 for $\vec{E}_i$ and k_i are straightforward to solve, the final expressions in general involve all of the susceptibility matrix elements as well as the angles θ and ϕ. The solutions are too complicated to be written out here; however, a relatively useful expression for the eigenvalues themselves is shown here for the case where the susceptibility is small:

$$k_{a,b} = k_{av} \pm \frac{\delta k}{2} \tag{2.27}$$

$$\frac{k_{av}}{k_0} \approx 1 + \frac{1}{16}\left\{3\chi_+ + 3\chi_- + 2\chi_0 + \cos(2\theta)(\chi_+ + \chi_- - 2\chi_0)\right\}$$

$$\begin{aligned} \frac{\delta k}{k_0} \approx \frac{1}{8}\ \{ & \ 9\chi_+^2 + 4\chi_0^2 - 4\chi_0\chi_- + 9\chi_-^2 - 2\chi_+(2\chi_0 + 7\chi_-) \\ & + 2\cos(2\theta)(3\chi_+ - 2\chi_0 - \chi_-)(\chi_+ + 2\chi_0 - 3\chi_-) \\ & + \cos^2(2\theta)(\chi_+ - 2\chi_0 + \chi_-)^2\ \}^{\frac{1}{2}} \end{aligned}$$

To get a feeling for the size of the susceptibility under typical experimental conditions, we can consider the simple situation of the bias field aligned with the propagation axis of the probe laser. In this case the eigenmodes in the medium are the two circular polarizations with wavevectors $k_{a,b} = k_0\sqrt{1+\chi_\pm} \sim k_0(1 + \chi_\pm/2)$ for small χ_q. If we focus on a single transition for one of the polarizations, say $\hat{\epsilon}_+$, then the susceptibility χ_+ can be written as

$$\chi_+ \sim -\frac{D_{pk}}{k_0 R}\frac{\gamma}{2\delta}\left(1 + i\frac{\gamma}{2\delta}\right),\ \delta \gg \gamma \tag{2.28}$$

where $D_{pk} \sim n_0\sigma R$ is the peak on-resonant optical depth (absorption coefficient), n_0 the peak atom density, and R the radius of the cloud. Typical experimental parameters for a condensate in-trap are 10^6 atoms, $R \sim 28\mu$m and $D_{pk} \sim 300$; therefore χ_+ will be small($\lesssim 0.1$) for $\delta \gtrsim 5\gamma \sim 30$MHz. For comparison, typical probe detunings in the experiment are 100MHz or more from the nearest resonance.

Since the peak phase shift of the probe is $\phi_{pk} = \frac{D_{pk}}{2}\frac{\gamma}{2\delta}$ for a single transition, the susceptibility can perhaps more usefully be written as

$$\chi_+ \sim -\frac{2\phi_{pk}}{k_0 R}\left(1 + i\frac{\gamma}{2\delta}\right), \quad \delta \gg \gamma \tag{2.29}$$

Sufficient signal-to-noise is achieved in images of atom clouds for peak phase shifts of ~ 0.5, a typical value for the experiment. Under these circumstances, for a condensate with radius $R \geq 20\mu$m, the magnitude of χ is less than 0.01, certainly small.

2.4.4 Phase-contrast image formation

After propagation through the atom cloud, the probe laser is the sum of scattered and unscattered field components, approximately identified as follows:

$$\vec{E}_{out} = \underbrace{\vec{E}_{in}}_{unscattered} + \underbrace{(\vec{E}_{out} - \vec{E}_{in})}_{scattered} \tag{2.30}$$

The unscattered part is quite reasonably approximated by the incident field $\vec{E}_{in}$ since the laser beam profile (with waist w ~1mm) is typically much larger than the cloud (with radius $R \sim 28\mu$m), making the fraction of scattered power ($\propto R^2/w^2 \ll 1$) small.

As mentioned above, the spatial Fourier transformation performed by the imaging lens [Fig. 2.1] spatially separates the light field into its unscattered and scattered components with, crudely speaking, zero and non-zero spatial frequencies respectively. This allows a small phase dot in the back Fourier plane of the imaging lens to selectively shift the phase of the unscattered component by ϕ_0. Thus, after the remainder of propagation to the image plane, the total probe laser field is:

$$\begin{aligned}\vec{E}_{image}(x,y) &= e^{i\phi_0}\vec{E}_{in} + \left(\vec{E}_{out} - \vec{E}_{in}\right) \\ &= \left[(e^{i\phi_0} - 1) + P^\dagger M P\right]\vec{E}_{in} \end{aligned} \tag{2.31}$$

using the expression for $\vec{E}_{out}$ from Eqn. 2.24. Any magnification m in the imaging system has been omitted here but can easily be included in this and subsequent formulae by adjusting the coordinates according to $\{x, y\} \rightarrow \{mx, my\}$.

In the experiment, a CCD camera collects the image proportional to the incident intensity ($I \propto |\vec{E}_{image}|^2$). For a given atom cloud, the standard protocol [78, 120] actually involves a sequence of three images, a probe shot to obtain the intensity profile $I(\vec{r})$ of the probe laser modulated by the presence of the atom cloud, a normalization shot to obtain the intensity profile $I_0(\vec{r})$ of the probe alone, and finally a background shot without probe light, giving $I_{backgr}(\vec{r})$. The normalization shot can be realized either by first destroying the condensate or, more nondestructively, by detuning the probe sufficiently far from resonance. On a pixel-by-pixel basis, background subtraction and normalization are performed to yield the raw phase-contrast signal:

$$S(\vec{r}) = \frac{I(\vec{r}) - I_{backgr}(\vec{r})}{I_0(\vec{r}) - I_{bacgr}(\vec{r})} - 1 \tag{2.32}$$

2.4.5 Phase-contrast signal inversion

The final step of imaging is to invert the raw signal S [Eqn. 2.32] for the column density of the atom cloud on a pixel-by-pixel basis. This step requires knowledge of the exact form of S, which in general depends on the details of the imaging setup such as the probe polarization, magnetic bias field orientation and so on. It is most to the point to consider the specific situations arising in the apparatus.

A variety of constraints on the optical table have resulted in the following arrangements for the three different orthogonal probe directions [see Figs. 2.2 & 2.3]. The “front” horizontal axis uses a probe laser incident with horizontal, linear polarization. Additionally, a horizontally polarizing beamsplitter cube is situated in front of the camera. The “side” horizontal axis uses a vertically polarized probe incident on the atoms. Lastly, the vertical axis uses circular polarization. In all cases, the rotating magnetic bias field of the TOP trap may have an arbitrary orientation in the horizontal plane at the time of imaging.

To calculate the phase-contrast signal, the detuning of the probe laser from all resonances is assumed to be large enough that the imaginary part of the susceptibility can be disregarded [see Eqn. 2.14]. Under this approximation, the probe eigenmodes in the atom frame are real as are their wavevectors. A useful way to obtain the phase-contrast signal starts with Eqn. 2.31 for $\vec{E}_{image}$ and uses the general expression Eqn. 2.25 for the projection matrix P in terms of angles α and β . Both angles depend on the magnetic bias field orientation through $\alpha = 2\phi$ and $\beta = \beta(\theta)$. The net signal for the front axis, for example, is

$$\begin{aligned} S_{front}(\xi_{av}, \delta\xi) &= 4\sin\frac{\phi_0}{2}\left[\sin\frac{\phi_0}{2} + \cos\frac{\delta\xi}{2}\sin\left(\xi_{av} - \frac{\phi_0}{2}\right)\right] \\ &+ 4\sin\frac{\phi_0}{2}\left[\cos\alpha\sin 2\beta\cos\left(\xi_{av} - \frac{\phi_0}{2}\right)\sin\frac{\delta\xi}{2}\right] \\ &- \frac{1}{4}\left[3 - \cos 2\alpha + 2\cos^2\alpha\cos 4\beta\right]\sin^2\frac{\delta\xi}{2} \end{aligned} \tag{2.33}$$

in which ϕ_0 is the phase shift due to the phase dot, and ξ_{av} and $\delta\xi$ are the phase shifts due to the atom cloud in terms of wavevectors k_{av} and δk [Eqn. 2.27]:

$$\begin{aligned} \xi_{av}(x,y) &= \int_{-\infty}^{\infty} (k_{av}(\vec{r}) - k_0)\,dz \\ \delta\xi(x,y) &= \int_{-\infty}^{\infty} (\delta k(\vec{r}) - k_0)\,dz \end{aligned} \tag{2.34}$$

Physically, ξ_{av} is the average phase shift of the probe passing through the cloud while $\delta\xi$ is indicative of Faraday rotation of the probe's polarization. Both quantities are directly proportional to the column density of the atom cloud integrated along the probe line of sight and have implicit dependencies on the bias field orientation through the polar angle θ (see Eqn. 2.27).

Phase-contrast signals such as S_{front} of Eqn. 2.33 cannot in general be algebraically inverted for the column density. However, a main point of this section is to demonstrate that, when phase shifts are not too large ($\xi_{av} \sim \delta\xi \lesssim 1$), all the probe signals can be reasonably approximated by the simple result

$$\begin{aligned} S_0(\xi) &= 4\sin\frac{\phi_0}{2}\left[\sin\frac{\phi_0}{2}+\sin\left(\xi-\frac{\phi_0}{2}\right)\right] \\ \xi &= \begin{cases} \xi_{av} & front,\, side\, probe \\ \\ \xi_{av}+\eta\delta\xi & vertical\, probe \end{cases} \end{aligned} \tag{2.35}$$

where $\eta = 0(\pm 1)$ applies to a strong(weak) trapping potential (see below). The approximate signal is the same expression one would obtain for a *scalar* probe field. For the case of a linearly polarized probe laser such as the front axis, this amounts to neglecting Faraday rotation effects, which can be seen directly by setting $\delta\xi = 0$ in the expression for the front probe signal [Eqn. 2.33]. A nice feature of $S_0(\xi)$ is that it can be readily inverted for ξ

$$\xi = \arcsin\left[\frac{S_0}{4\sin\frac{\phi_0}{2}} - \sin\frac{\phi_0}{2}\right] + \frac{\phi_0}{2} \tag{2.36}$$

Eqn. 2.36 is the signal inversion used in the experiment with S_0 replaced by the actual acquired signal. In order to assess the validity of this approximation, as well as other effects such as bias field orientation, a representative example is now studied in numerical detail. The full phase-contrast signal S_{front} [Eqn. 2.33] for the front probe axis is calculated for a condensate under typical experimental conditions and compared to the approximate expression S_0 [Eqn. 2.35]. The magnetically trapped ground hyperfine state, $|F = 1, m_F = -1\rangle$, is considered. In addition, the two typical configurations of the TOP trap are assessed, (i) a strong trap and (ii) a weak trap where the atom cloud sags downward by about 1mm under the pull of gravity. In the former case the atoms feel a bias field B_b rotating in the horizontal plane. In the later sagged case, the atoms feel both a rotating field of $B_b \sim 1.7$G and an additional static downward field of $B_q \sim 3.2$G. Relevant condensate parameters for the weak trap include number $N \sim 10^6$ and Thomas-Fermi radius $R \sim 28\mu$m, giving a peak on-resonant optical depth of $D_{pk} \sim 300$, assuming a cycling transition. The same optical depth is used for the strong trap for comparison purposes.

First, a feeling for the size of the optical phase shifts induced by the condensate (in the weak trap) is given in Fig. 2.6 where ξ_{av} and $\delta\xi$ are plotted over the standard range of probe detunings used. The probe is detuned below all resonances for the $|1,-1\rangle$ state such that the signal is positive or bright on the CCD screen relative to the background. The typical peak phase shift of $|\xi_{av}| \sim 0.3 - 0.5$, which sets the standard range of detunings, represents an operational compromise between nondestructiveness and a good signal-to-noise ratio [see Section 2.5].

Figure 2.7(a) shows the dependence of ξ_{av} and $\delta\xi$ on the orientation of the rotating bias field B_b for the $|F=1, m_F=-1\rangle$ state and a fixed detuning. The fractional peak-to-peak variation of ξ_{av} is fairly small whereas the value of $\delta\xi$ varies considerably over bias orientation. The variation of the phase-contrast signal itself is shown in Figs. 2.7(b)&(c) for a variety of peak average phase shifts. The *fractional* variation becomes worse when the phase shift is larger or, most importantly, when the probe frequency approaches a resonance, the nearest one corresponding to the $F=1 \rightarrow F'=0$ transition at the right edge of the plots in Fig. 2.7. Additionally, the strong trap shows more of an effect than the weak one. By way of conclusion, in the weak trap where most of the vortex work is pursued, reasonable phase shifts $\xi_{av} \leq 0.6$ and probe frequencies greater than 100MHz from resonance will ensure that variations in the peak signal will not exceed 5% if the bias field orientation is left uncontrolled. A more serious problem will arise for samples of smaller number, which force the probe detuning near to resonance to achieve a good signal.

Another important imaging effect to consider is nonlinearity in the phase contrast signal, which if left unaccounted for, will effectively distort the image of an atom cloud, making it more “peaky” or flat-topped depending on the trend of the nonlinearity. Since we use only an approximate form of the true signal to invert for an image, there is the potential for distortions due to nonlinearity. The maximum fractional difference between

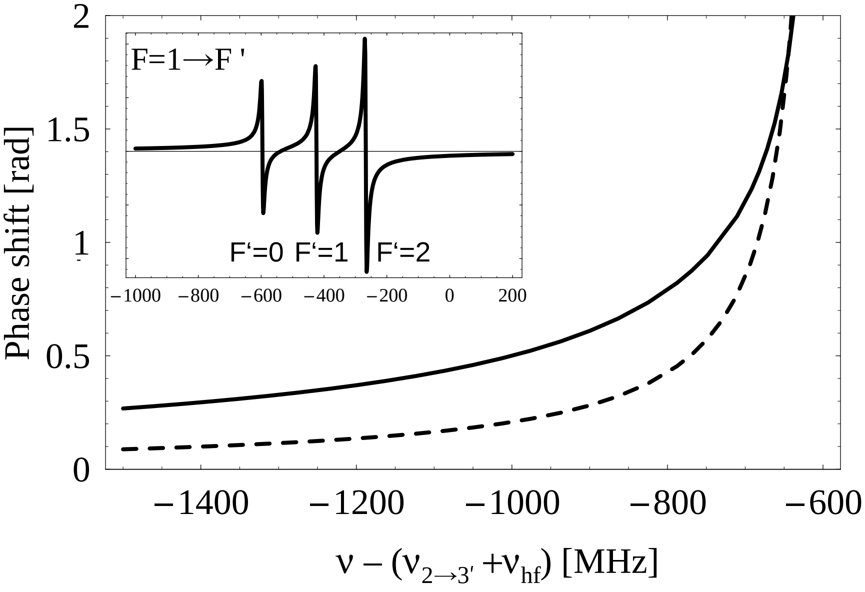

Figure 2.6: Average phase shift ξ_{av} (solid line) and differential phase shift $\delta\xi$ (dashed line) induced by a typical $|F=1, m_F=-1\rangle$ condensate versus probe laser frequency ν. The frequency range plotted is the usual operating range in the experiment. The inset shows the average phase shift over a larger frequency range including all resonances.

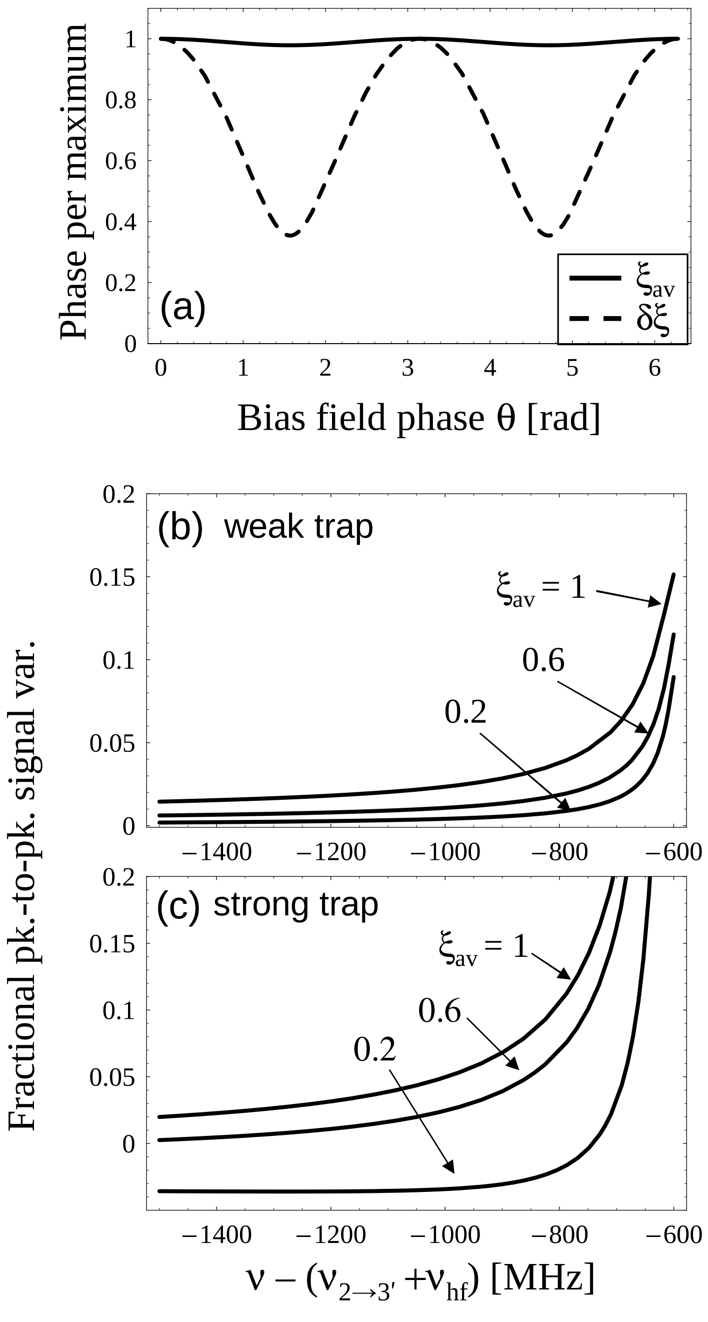

Figure 2.7: (a)Phase variation due to rotating TOP bias field $\vec{B}_b(\theta)$. Total fractional variation of phase-contrast signal is shown in (b) and (c) as a function of probe frequency ν for three different magnitudes of the average optical phase shift ξ_{av}.

the approximate signal $S_0(\xi_{av})$ [Eqn. 2.35] and the front probe signal $S_{front}(\xi_{av}, \delta\xi)$ [Eqn. 2.33] is shown in Fig. 2.8, again for the $|1, -1\rangle$ state over typical detunings. The strong trap shows more of an effect than the weak one. As a rule of thumb, an effect exceeding 10% should only arise for samples of small number where the probe needs to be less than 100MHz detuned of the $F = 1 \rightarrow F' = 0$ resonance to achieve a good signal ($\xi_{av} \sim 0.5$).

There is one additional nonlinear effect called "phase wrap," which is intrinsic to phase contrast. Since the signal is an interference effect with 2π periodicity, the signal must saturate for large enough phase shifts and begin to decrease [see Fig. 2.9]. The saturation point depends on the choice of phase dot retardance. For the choice of $\phi_0 = \pi/2$ used in the experiment, the effect is not much of an issue for *positive* phase shifts as the saturation point occurs at a fairly high phase shift. However, it is an issue for negative phase shifts since the phase-contrast signal is not symmetric. This is the main reason why the probe detuning is chosen to give a positive phase shift when looking at a cloud composed of a single spin state.

2.5 Nondestructive imaging

The utility of phase-contrast imaging lies in its nondestructive character, allowing time sequences of images or "movies" to be taken of a single atom cloud in-trap. This is particularly valuable for measuring time-dependent excitations of a condensate with a minimum amount of data-taking [e.g. Section 3.6]. As well, nondestructive imaging can provide the only way to analyze condensate dynamics in situations when the initial conditions fluctuate from each realization of a condensate sample to the next [e.g. Section 3.5]. A potentially interesting application of phase-contrast imaging would be to use the information garnered from an image to feed back onto the condensate, perhaps for some type of coherent control. Admittedly, a servo-loop based on the current implementation of the imaging would have a fairly low bandwidth since

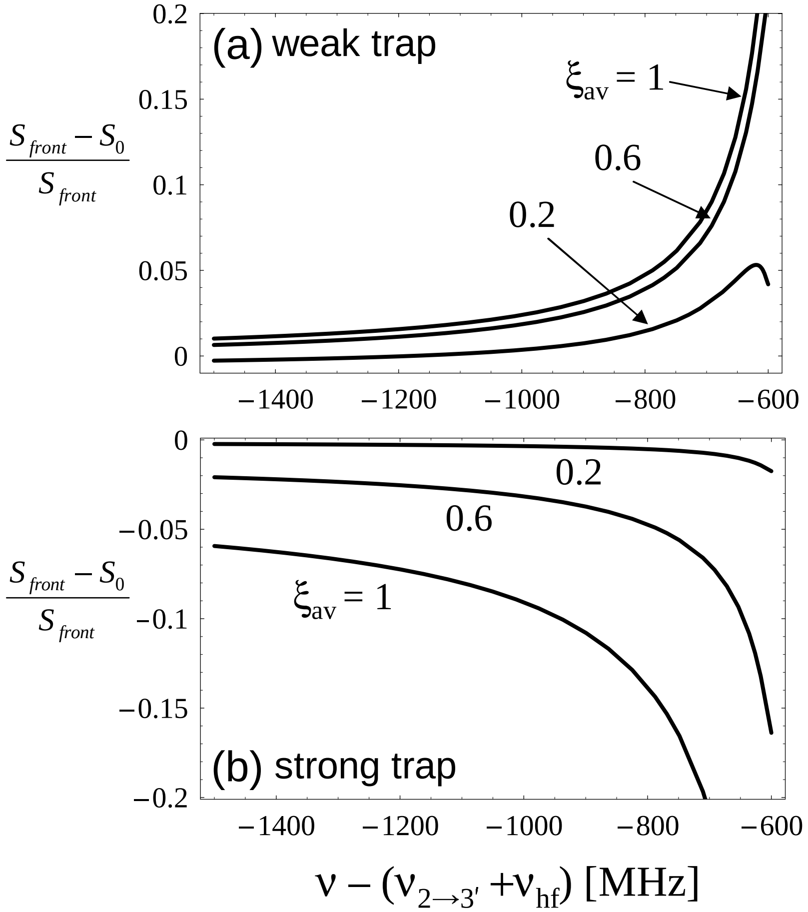

Figure 2.8: Fractional error between approximate and true phase-contrast signals, S_0 and S_{front} respectively, for the front probe direction as a function of probe laser frequency ν. Contours of fixed optical phase shift ξ_{av} are labeled accordingly. Overlapping contours would indicate a linear error independent of phase shift. The degree of image nonlinearity accrued by using the approximate signal for image processing can be inferred from the vertical spread of the contours at a fixed probe frequency ν.

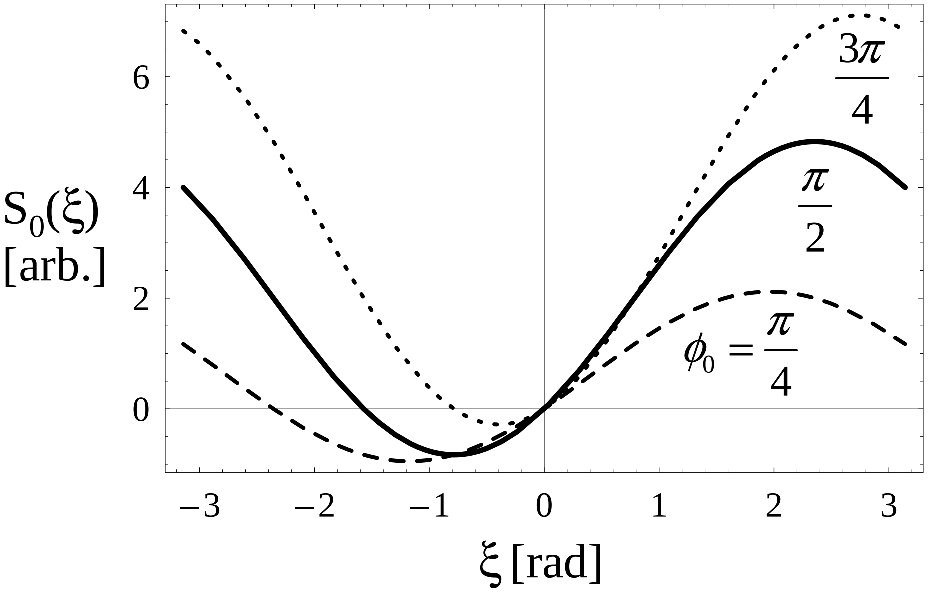

Figure 2.9: Phase-contrast signal S_0 as a function of induced optical phase shift ξ for three different phase dot retardances ϕ_0. The experiment uses $\phi_0 = \pi/2$

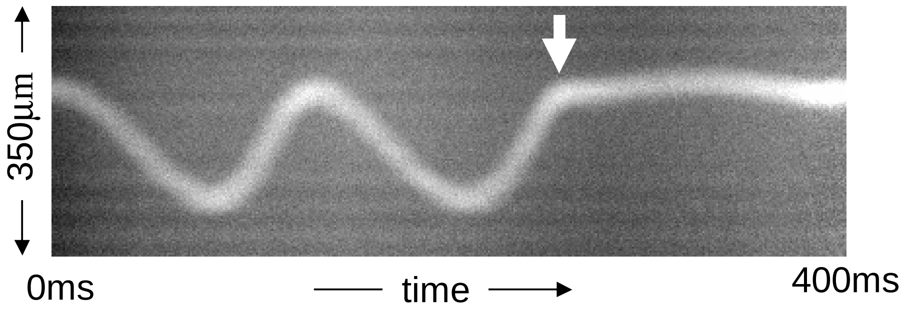

Figure 2.10: Nondestructive streak-camera image of a trapped condensate showing removal of its center-of-mass motion (up-down oscillation) by shifting the trap. The arrow indicates the time where the trap center is suddenly shifted.

the readout and processing of a sequence of images from the CCD camera requires a reasonable fraction of a second. As a simple example, phase contrast can be useful to assess and remove undesirable center-of-mass oscillations ("slosh") of the condensate in the confining potential. Sloshing represents a hindrance in many experiments such as wavefunction engineering [Chapter 3], where the condensate needs to be selectively manipulated across its spatial extent. For the simple case of reproducible slosh from shot to shot, a phase-contrast image can be made at the start of the day to measure the oscillations. In subsequent shots, an "antislosh" step can be applied, where the trap center is suddenly kicked or shifted with the correct phase and amplitude to bring the condensate to a stop [Fig. 2.10].

The statement that phase-contrast imaging is "nondestructive" is not an exact statement and requires some quantitative clarification. The two issues focused on here are (i) condensate depletion and heating due to residual spontaneous scattering from the off-resonant probe laser and (ii) the effect on condensate phase due to the laser-induced ac Stark shift.

2.5.1 Spontaneous scattering and number loss

The nondestructive character of phase-contrast imaging is intimately related to the signal-to-noise desired for the images. A discussion of signal-to-noise for phase contrast can be found in a previous thesis [120]. A few points are added here as they relate to *non-destructive* imaging in practice. For the sake of discussion, the atom cloud is assumed to induce a small phase shift $\xi \ll 1$; then the phase contrast signal is $S \sim 2\xi$. The number of spontaneously scattered photons during the imaging is $N_{sc} \propto I\xi^2$ where I is the probe intensity incident on the atoms. Thus, the destructiveness, characterized by N_{sc}, can be reduced by decreasing the intensity or increasing the probe detuning δ since $\xi \propto 1/\delta$. However, signal-to-noise represents a different issue. If the signal is assumed to be shot-noise limited then $S/N \sim \sqrt{I}\xi$. We can improve the signal-to-noise ratio by either increasing the intensity or detuning closer to boost the phase shift. Which is preferable to reduce destructiveness? The answer is that it does not matter because the signal-to-noise depends only on the spontaneous scattering rate: $S/N \propto N_{sc}^{1/2}$. Therefore, in the shot-noise limit the signal-to-noise is fixed by the scattering rate allowed for a stipulated destructiveness.

On the other hand, most of the time the image noise is dominated by background interference fringes proportional to the incident intensity. In this case, the signal-to-noise is $S/N \sim 2\xi/\eta$ where η characterizes the strength of the fringes. Under these circumstances, if the peak density of clouds being imaged is low, for example in the case of thermal clouds, the only way to obtain better signal-to-noise is to tune the probe closer to resonance. The intensity then is dropped to preserve nondestructiveness as much as possible. At some point the intensity is low enough that the shot noise becomes of the same order as the fringe noise.

The destructive nature of the probe laser has been studied by shining it continuously on the condensate. A typical result is shown in Figure 2.11(a). The decay of total condensate number matches fairly well with the calculated spontaneous decay rate (1.5 times smaller), assuming a single frequency for the probe. The destructiveness can be considerably worse if, for example, the probe laser is running poorly single-mode.

When actually taking images, the probe does not shine continuously but is pulsed on only for brief periods of exposure (100μs). To assess any delayed heating effect following a probe pulse, a sequence of eight images has been taken using three different time intervals and a deliberately destructive probe intensity [Fig. 2.11(b)]. Only a relatively small difference in condensate loss is seen between the image sequence lasting 0.14s and the one lasting 4s, indicating that most of the atom loss due to the probe pulse occurs during the pulse time and not as a result of delayed heating.

2.5.2 Stark effects and measurement induced squeezing

Nondestructive phase-contrast imaging of condensates offers the intriguing possibility to produce measurement-induced squeezed states of atom number [57, 71], analogous to squeezed states for photons. A familiar concept from quantum optics is the existence of an uncertainty relation between photon number and phase, $\delta N \delta \xi \geq 1$. At the quantum limit where the equality sign is satisfied, a reduction of number fluctuations results in an increased variance in the phase. For a maximally squeezed state ($\delta N \sim 1$), the phase is undefined. One can argue formally that the number-phase uncertainty relation is a feature of all systems of indistinguishable bosons and so applies to a condensate as well. This would imply that a nondestructive measurement of condensate number below the atom shot noise could create a squeezed condensate. The concomitant loss of a well-defined condensate phase can be thought of as the back-action effect of the number measurement. This formal discussion has not identified the physical mechanism for the back-action. The object of this section is to show how shot noise on the probe laser intensity together with the ac Stark effect [3] produce the destructive effect on the atoms' phase. In the spirit of the "Heisenberg microscope," a direct consideration of an

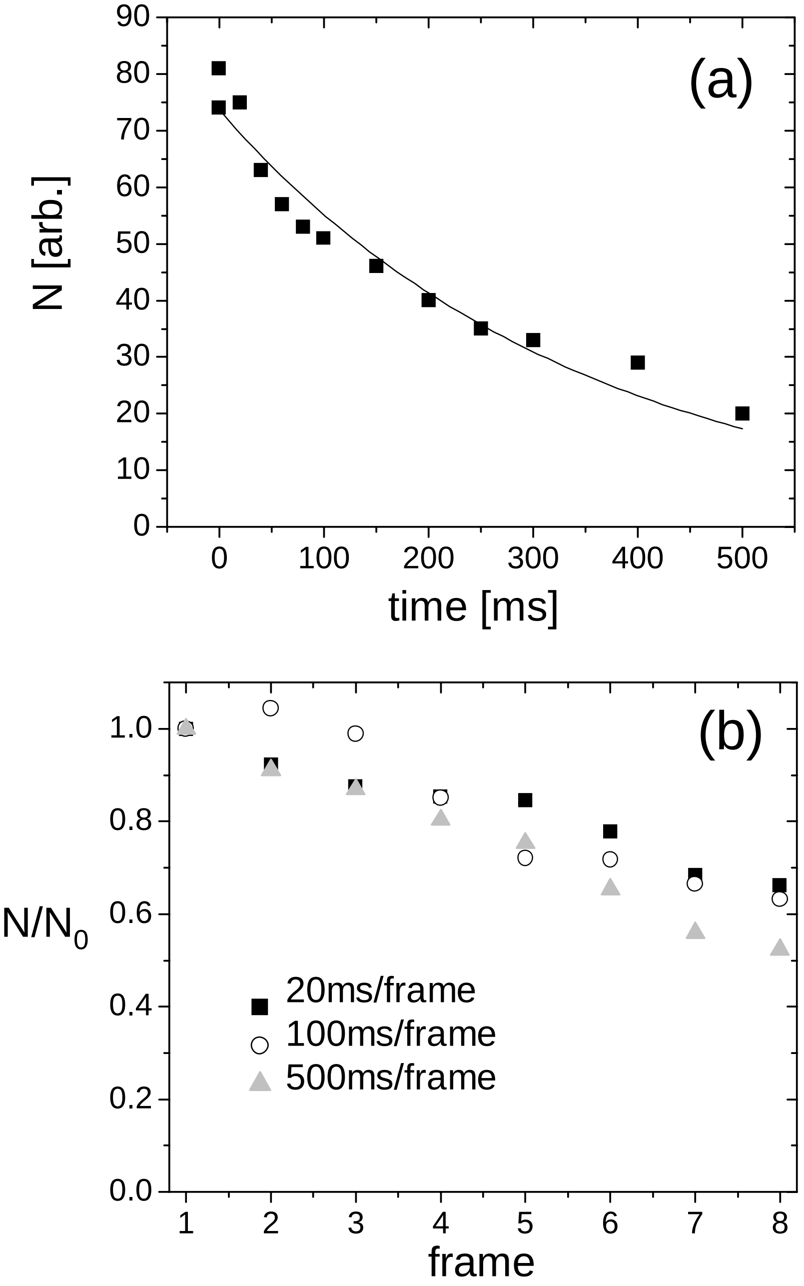

Figure 2.11: Destructive number reduction of a condensate in the presence of an off-resonant probe laser. (a)Condensate number decay due to a continuously shining probe laser with an intensity of $150\mu W/cm^2$ and a detuning of 2.1GHz from the $F = 1 \rightarrow F' = 0$ resonance. The fit exponential decay rate is $2.9(2)s^{-1}$ compared to a calculated spontaneous scattering rate of $1.9s^{-1}$. (b)Time sequence of eight probe frames with three different time intervals between frames. The light pulses for each frame are 100μs long with a large probe intensity of $2500\mu W/cm^2$ (a factor of 10 larger than typical) and a detuning of 1.1GHz from the $F = 1 \rightarrow F' = 0$ resonance.

experiment is used to arrive at the number-phase uncertainty relation for a condensate. A side benefit is a brief assessment of the feasibility to obtain number squeezing with phase-contrast imaging.

Number-squeezing due to interatomic interactions has already been observed in multi-condensate systems [132, 93]. The loss of interference contrast between the individual condensates provides a signature for the large variance in relative phase. An experiment to observe measurement-induced squeezing would use a similar technique. For example, optical tweezers can be used to split a condensate spatially into two, one of which is reserved as a phase reference. The other condensate is then subjected to a nondestructive probe, after which the condensates are re-interfered to assess the probe's affect on their relative phase. An interesting alternative that does not require any spatial separation makes use of a condensate composed of two internal spin states together with a coherent coupling drive to create a beamsplitter in the time domain. A coupled two-component condensate composed of the simultaneously magnetically trapped hyperfine states $|1,-1\rangle$ and $|2,1\rangle$ [Fig. 2.4] has already been realized with this experimental apparatus [120] and is covered in more detail in Chapter 3. A key feature of this system is that phase contrast imaging can distinguish between the two states without needing to spatially separate them. The probe laser frequency is detuned between the two states such that the $|1,-1\rangle$ state imparts a positive phase shift to the probe beam while the $|2,1\rangle$ state imparts a negative phase shift. As a result, in the presence of both states the net phase-contrast signal provides a direct readout of the number difference.

To simplify the discussion, the phase-contrast imaging of a single-component condensate is considered. The generalization to two components is straight forward and leads to similar results. The phase-contrast signal collected on the CCD camera provides a measure of the optical phase shift ξ imparted by the condensate, which in turn is proportional to its column density $\bar{n}(x, y)$,

$$\xi = \beta_{pc}\bar{n}(x, y) \tag{2.37}$$

where β_{pc} is a constant which can be determined from the previous sections of this chapter. To obtain the total number of atoms in the condensate, the image needs to be integrated over all N_{pix} CCD pixels spanned by the condensate profile. The uncertainty in the total number of atoms for small phase shifts is thus

$$\delta N_{at} = \frac{1}{\beta_{pc}} \frac{A_{pix}}{m} \left(\sum_{i=1}^{N_{pix}} \delta\xi_i^2 \right)^{1/2} . \tag{2.38}$$

In the above equation, A_{pix} is the area of a pixel, m accounts for the imaging magnification, and $\delta\xi_i$ is the phase uncertainty at the i^{th} pixel. Neglecting technical noise, the output of the probe is very nearly a coherent state satisfying the uncertainty relation $\delta N_{ph}\delta\xi_{ph} \sim 1$ and having shot-noise fluctuations about the average photon number, $\delta N_{ph} \sim N_{ph}^{1/2}$. The uncertainty relation applies at each CCD pixel where N_{ph} is the number of photons arriving at that pixel. For small phase shifts, the number of photons will be approximately pixel-independent, allowing the uncertainty in atom number to be reduced to the simple result

$$\delta N_{at} = \frac{1}{\beta_{pc}} \frac{A_{pix}}{m} \left(\frac{N_{pix}}{\eta_{QE}} \right)^{1/2} \delta\xi_{ph} \tag{2.39}$$

where $\delta\xi_{ph} \approx 1/N_{ph}^{1/2}$. The coefficient η_{QE} has been added to account for the quantum efficiency of the CCD detector. To connect with experimental parameters, the number of photons at a CCD pixel can further be written in terms of the probe intensity I incident on the atoms

$$N_{ph} = \frac{\tau}{\hbar\omega} \frac{A_{pix}}{m} I \tag{2.40}$$

The various constants include the probe duration τ, the laser frequency ω, the pixel area A_{pix} and the magnification of the imaging system m.

Now that the nondestructive number measurement has been dealt with, it only remains to consider the backaction effect on the condensate phase. The off-resonant probe induces an ac Stark shift in the internal energy state of the condensate atoms, resulting in an intensity-dependent phase shift

$$\xi_{at} = \frac{\tau \beta_{st}}{\hbar \omega} I \tag{2.41}$$

The constant β_{st} can be determined from perturbation theory for weak intensities. The *average* phase shift accumulated by the condensate can always be taken into account from a measure of the average probe intensity; what remains, however, is the uncertainty introduced by fluctuations in the intensity. Equation 2.40 can be used to relate the intensity at the atoms to the photon number counted by the CCD. This allows the uncertainty in condensate phase to be expressed in terms of the photon counting statistics at the detector,

$$\delta\xi_{at} = \beta_{st} \frac{m}{A_{pix}} \delta N_{ph} \tag{2.42}$$

The uncertainties for atom number [Eqn. 2.39] and phase [Eqn. 2.42] can be combined to yield the uncertainty relation

$$\delta N_{at} \delta\xi_{at} \sim \left\{ \frac{\beta_{st}}{\beta_{pc}} \right\} \left(\frac{N_{pix}}{\eta_{QE}} \right)^{1/2} \underbrace{(\delta N_{ph} \delta\xi_{ph})}_{\sim 1} \tag{2.43}$$

Thus the nondestructive measurement transfers the uncertainty relation for the probe photons to one for the atoms. For simple probe arrangements, for example using a single circular polarization and a magnetic bias field aligned along the imaging axis, the expression β_{st}/β_{pc} in Eqn. 2.43 is equal to one (and is expected to be larger than one for more complicated situations). In the limit of a single CCD pixel and unity quantum efficiency η_{QE}, the uncertainty relation for the atoms reaches the quantum limit expected for a system of indistinguishable bosons.

The final point addressed in this section is the feasibility of squeezing the fluctuations in condensate number with a nondestructive probe. Measurement-induced squeezing is achieved by a determination of the number to better than the atom shot-noise. The degree of squeezing can be assessed from the measurement uncertainty Eqn. 2.39

assuming an ideal detector with 100% efficiency. A practical limitation to this process is the fraction of condensate atoms lost as a result of spontaneous scattering from the probe. Clearly, the squeezing is not useful if the probe also destroys the condensate. The number of scattered photons during the probe pulse is $N_{sc} = N_{at}\Gamma\tau$ with Γ being the spontaneous scattering rate [124]. For a simple probe configuration with large detuning, the number uncertainty [Eqn. 2.39] for an ideal detector is easily written in terms of N_{sc}

$$\delta N_{at} = \left(\frac{A_c}{\sigma c_*}\right)^{1/2}\left(\frac{N_{at}}{N_{sc}}\right)^{1/2} \tag{2.44}$$

The value of the coefficient c_* is of order unity or less and, in general, depends on several Clebsch-Gordon coefficients [Eqn. 2.13] as well as the probe detuning. If a cycling transition is being used for probing, then $c_* = 1$, independent of detuning. The quantity $\sigma \sim \lambda^2/2$ is the on-resonant light scattering crosssection [Eqn. 2.8] whereas $A_c = \frac{N_{pix}A_{pix}}{m}$ is the crossectional area of the condensate in terms of detector variables with the folowing qualification: The crossectional area is $\sim \pi R_c^2$ for a condensate with radius R_C that is larger than the diffraction limit; otherwise, $A_C \sim \pi\lambda^2$ and the first term in Eqn. 2.44 attains a minimum value $(A_c/\sigma)^{1/2} \sim 1$. For typical experimental parameters, a more appropriate value for this ratio is $10 - 100$. Therefore, to achieve a maximally squeezed state ($\delta N \sim 1$), the number of scattered photons needs to be at least as large as the atom number if not larger, assuredly killing the condensate [see Section 2.5.1].

Even if the squeezing is not maximal, a reasonable effect such that $\delta N_{at} = N_{at}^{1/2}/\alpha$ with $\alpha > 1$ could nevertheless be useful for atom-interferometric applications. What considerations limit the maximum value of α? There are a number of possibilities in connection with spontaneous scattering. First, the condensate number may be so heavily depleted following the probe measurement that δN_{at}, albeit absolutely small, is not *fractionally* small anymore. This does not represent a significant limitation and only plays a role if an overwhelming fraction of the condensate is destroyed. The second limit is reached when the uncertainty δN_{sc} in the number removed from the condensate becomes comparable to the uncertainty δN_{at} of the number measurement. This limit has some flexibility with regard to probe detuning and a discussion is left to a more detailed treatment. Instead, a third issue is briefly considered here, whereby the squeezing can be strongly limited by the maximum particle density achievable in the condensate. The maximum value of the density is determined by the rate of density-dependent inelastic loss, which depends on the atomic species being used. The resulting limitation to number squeezing can be seen to arise as follows: With $\delta N_{at} = N_{at}^{1/2}/\alpha$, Eqn. 2.44 can be solved for α:

$$\alpha = \left(N_{sc} \frac{\sigma c_*}{A_c} \right)^{1/2} \tag{2.45}$$

It is evident that the level of squeezing is connected to the number N_{sc} of photons that are spontaneously scattered. The ultimate limit to N_{sc} is on the order of the number of atoms N_{at}. This leads to a maximum value of $\alpha = \alpha_{max}$, which can be expressed explicitly in terms of the number density $n \sim N_{at}/(A_c L)$. Here, L is the size of the third dimension of the condensate. The net expression for α_{max} is given by

$$\alpha_{max} \sim \left(n\lambda^3 \frac{L c_*}{2\lambda} \right)^{1/2} \tag{2.46}$$

For ^{87}Rb, the maximum density is about $n \approx 10^{14}\ \mathrm{cm}^{-3}$, yielding $n\lambda^3 \sim 100$. The size L depends on the number of atoms and the trapping arrangement. As a specific example, in a lithographic microtrap where atom interferometry may be realized, approximate parameters include $N_{at} \sim 10^4$ and $L/\lambda \sim 1 - 10$ [4]. As a result, the limit to squeezing imposed by a finite density is roughly $\alpha_{max} \sim 10$, which is a factor of 10 less than maximal squeezing. Of course, such a value is an upper limit based on a considerable loss of atoms. The practical value of α_{max} will be lower depending on such issues as how many atoms must be preserved to achieve good detection signal-to-noise.

A significant improvement to this situation can be achieved by wrapping an optical cavity with finesse $\mathcal{F}$ around the atoms. This has two effects, (i) to increase the effective path length through the atom cloud (and optical phase shift) by $\mathcal{F}/\pi$ and (ii) to boost the intensity in the cavity by $\mathcal{F}/\pi$ relative to the input [143]. If the intensity into the cavity is reduced to maintain a given amount of spontaneous scattering, the shot-noise of the phase-contrast image will certainly increase by $\sqrt{\mathcal{F}/\pi}$; however, the image signal itself increases much more - by $\mathcal{F}/\pi$ - due to the cavity-enhancement of the phase shift. The net result is a significant reduction in the number fluctuations,

$$(\delta N)_{cavity} = (\delta N)_{free} \left(\frac{\pi}{\mathcal{F}}\right)^{1/2} \tag{2.47}$$

with the cavity-free expression $(\delta N)_{free}$ given by Eqn. 2.44. At least a factor of $\sim$10 improvement in the squeezing could be achieved with a reasonable finesse of $\mathcal{F} \sim 10^3$.

Chapter 3

Single Vortex Lines and Rings

3.1 Introduction

Quantized vortex lines, forming visible topological defects in a quantum fluid, are one of the most appealing demonstrations of superfluidity and superconductivity (For a review, see [155, 74]). What sets quantum fluids, including dilute-gas BEC, apart from their classical counterparts is that rotation can be manifested *only* in the form of quantized vortices. This is a direct consequence of the fluid being associated with a macroscopic order parameter(wavefunction) $\Psi = \sqrt{\rho(\vec{r})} e^{i\mathcal{S}(\vec{r})}$. Because the fluid's velocity field $\vec{v}(r)$ is associated with the gradient of the order parameter's phase [155], any flow is fundamentally restricted to be irrotational (curl-free)

$$\nabla \times \vec{v}(\vec{r}) \sim \nabla \times (\nabla \mathcal{S}(\vec{r})) = 0. \tag{3.1}$$

This immediately precludes the occurrence of solid-body rotation, so familiar from classical fluids, as it is ostensibly non-irrotational. What is possible are vortices, characterized by an azimuthal phase gradient around a line defect that defines the vortex core. The single valuedness of the order parameter requires that the phase accumulated in a closed path around the core be an integer multiple of 2π or, in other words, that the circulation be quantized in units of $\hbar/m$ [Figure 3.1].

This chapter focuses on the creation and dynamical behaviour of singly quantized vortices in a dilute-gas Bose-Einstein condensate. While the study of vortices in a

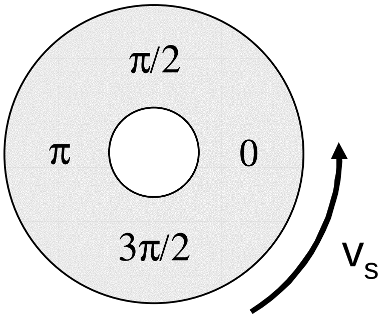

Figure 3.1: Singly quantized vortex in a quantum fluid, characterized by a 2π phase wrap around a fluidless core. The azimuthal phase gradient is associated with a superflow around the core, as indicate by the arrow.

condensate may be considered very much “condensed matter“ in flavor, a truly atomic physics oriented method - wavefunction engineering - is used to make the vortices. This technique, based on a theoretical proposal by Williams and Holland [159], led to the first experiment to demonstrate vorticity in an atomic condensate [122]. A slightly different interpretation of the original proposal [159] is presented here to emphasize the experimental route to generating condensates with arbitrary wavefunctions.

The idea for wavefunction engineering arose out of earlier experiments with two-component condensates, in which a microwave-frequency field is used to transfer population between two internal spin states of ^{87}Rb [120]. The essence of creating an arbitrary wavefunction is to control the amplitude and phase of the transferred population in a spatially dependent way. A novel benefit of this particular vortex creation technique is the ability to create two-component vortices, where fluid composed of one spin state contains vorticity while the fluid in the other spin state is non-rotating and fills out the vortex core. Because of the interatomic interactions, a condensate in a superposition of the different spin states amounts to two interpenetrating, *interacting* superfluids [64, 120]. The relative density evolution of the two superfluids provides a fascinating additional degree of freedom to the dynamics described in this chapter.

The deterministic introduction of a single vortex into a condensate via wavefunction engineering provides an excellent starting point to assess vortex dynamics. Studies of two fundamental "bending modes" of a vortex have been made, namely precession of the vortex core position about the condensate center and tilting of the vortex line's orientation. In Section 3.5, the core precession will be shown to be the dynamical response of the vortex to the radial forces pulling on it. The same forces more generally apply a bending force to a vortex line offset from the symmetrical position of the condensate center [151, 89]. Under these circumstances, a curved shape can minimize the vortex length. This is equivalent to energy minimization since for a condensate with repulsive interactions there is an associated energy cost per unit length to suppress the density along the vortex core. Vortex curvature is expected to be prominent in the case of vortices aligned with the long direction of a strongly prolate condensate, where significant vortex shortening can be achieved with a bent shape. Indeed, increasing vortex curvature in the presence of thermal dissipation has recently been observed by the ENS group in their cigar-shaped condensate [142]. On the other hand, for the roughly spherically shaped condensates of this experiment, the vortices are relatively short and stiff and are expected to be essentially straight except for very near to the cloud edge.

Nevertheless, we *have* been able to generate "maximally bent" vortices in the form of vortex rings fully situated within the bulk of the condensate. The formation process of the vortex ring - through the catastrophic decay of a dark soliton - represents interesting physics in and of itself, being a confluence of ideas from nonlinear optics, condensed matter and atomic BEC. Furthermore, the method demonstrates the use of wavefunction engineering to create a precursor state, the soliton, that has the correct symmetry to evolve through dynamical instabilities into a desired target state, the vortex ring. Perhaps this idea may prove useful to create objects in the condensate with yet more complicated topologies.

As a final comment, each of the experiments in this chapter has involved the implementation of new techniques to manipulate and probe condensates with vorticity. These include the general technique of wavefunction engineering with two-component condensates, tailored TOP confining potentials for vortex manipulation [Section 3.6], multiple axes of imaging [Section 3.8], and two complementary methods of vortex detection - direct imaging of vortex cores in ballistically expanded condensates [Section 3.5] and angular momentum sensing using surface-wave spectroscopy [Section 3.6]. (Core detection in expansion was in fact first demonstrated by the ENS group [118].) In general, the study of single-vortex dynamics has provided a solid intuition and a proving ground for techniques in the study of vortex behaviour in a condensate. The techniques have been broadly useful in the later experiments of Chapter 4 involving multiple vortices and have spawned new ideas which might otherwise have been missed, for example, the interaction of surface modes with highly rotating condensates [Section 4.8].

3.2 Coupled two-component condensates

Since two-component condensates form the basis for the wavefunction engineering technique, a short overview of their main properties is presented here. A more detailed account may be found in [120]. Rubidium has three magnetically trappable hyperfine ground states, two of which have nearly the same magnetic moment and so can be held simultaneously in overlapping TOP potentials [120]. These two states, $|F = 1, m_F = -1\rangle$ and $|F = 2, m_F = 1\rangle$ hereafter known as $|1\rangle$ and $|2\rangle$, can be coherently coupled with a ~6.8GHz two-photon transition via the virtual intermediate state $|F = 2, m_F = 0\rangle$ [Figure 3.2]. As long as the radio frequency (rf) and microwave fields comprising the two-photon transition are sufficiently far detuned from the intermediate state, it can be adiabatically eliminated leaving an effective two-level system $\{|1\rangle, |2\rangle\}$. The usual coherent population transfer of Rabi oscillations may be observed between the states

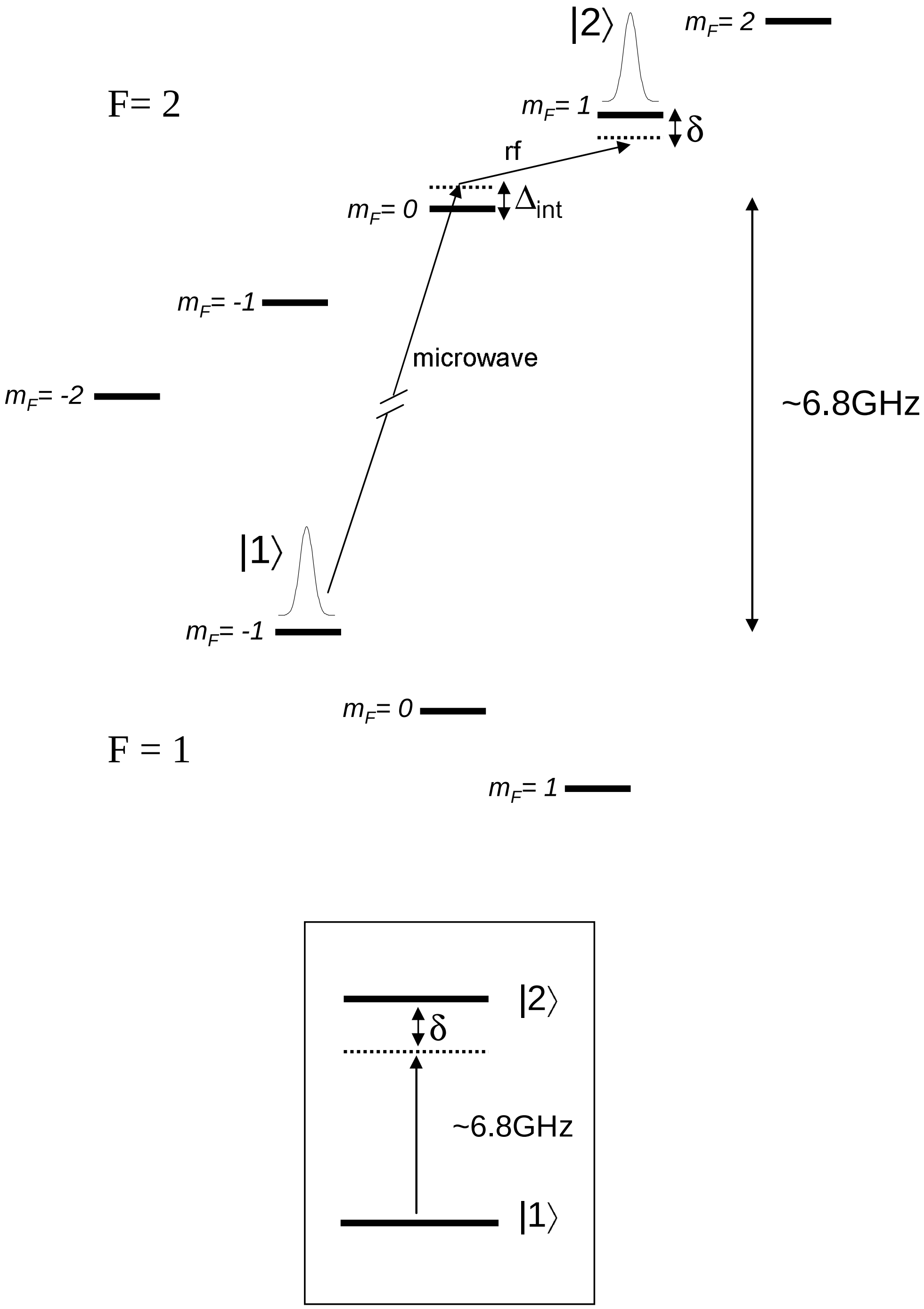

Figure 3.2: Two-photon coupling between two hyperfine spin states of the ^{87}Rb ground-state $5S_{1/2}$. The spin states, labeled $|1\rangle$ and $|2\rangle$ for short, may be simultaneously confined in overlapping magnetic potentials. The two-photon coupling is comprised of a microwave photon (~6.8GHz) and an rf photon (~1MHz) as indicated. The intermediate state that mediates the coupling may be adiabatically eliminated, leaving a two-level system with an effective coupling drive (boxed inset).

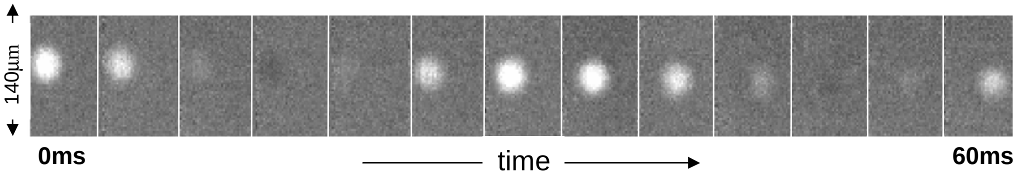

Figure 3.3: Nondestructive imaging of a magnetically trapped condensate undergoing spatially uniform two-photon Rabi oscillations between internal states $|1\rangle$ and $|2\rangle$. The frequency of the probe laser is tuned such that it is primarily sensitive to the presence of the $|1\rangle$ state, which appears as bright on a gray background.

$|1\rangle$ and $|2\rangle$ [Figure 3.3] with an effective on-resonant ("bare") Rabi frequency given by

$$\Omega_0 = \frac{\Omega_{\mu W}\Omega_{rf}}{4\Delta_{int}} \tag{3.2}$$

Approximate values for the intermediate state detuning Δ_{int}, microwave and rf Rabi frequencies $\Omega_{\mu W}$ and Ω_{rf} are ~1MHz, ~100KHz and ~0-10KHz respectively, giving an effective Rabi frequency Ω_0 in the range 0-1KHz. As an aside, the nondestructive imaging of Rabi oscillations in Figure 3.3 shows nicely how phase contrast imaging is an ideal probe for the two-component dynamics as it is state sensitive through the choice of probe laser detuning.

The dynamics of the two-component system involve more than simply coupling of internal levels since the components interact through collisions. In the dilute-gas regime characterizing the condensate samples, the weak interparticle interactions are well described by an elastic s-wave scattering length and an associated density-dependent mean field [69]. Three scattering lengths, a_{11}, a_{22} and a_{12}, refer to each of the intra- and inter-species two-body interactions possible for the $|1\rangle$ and $|2\rangle$ states. The values of the scattering lengths are all positive, indicating repulsive interactions, and are of very nearly the same strength [5]. However, slight differences in the interactions make it such that it is energetically favorable for a mixture of the two fluids to phase-separate into a distribution dependent on particulars such as the confining geometry [102, 99]. Figure 3.4 shows the phase separation behaviour typical of the spherical trap used in this

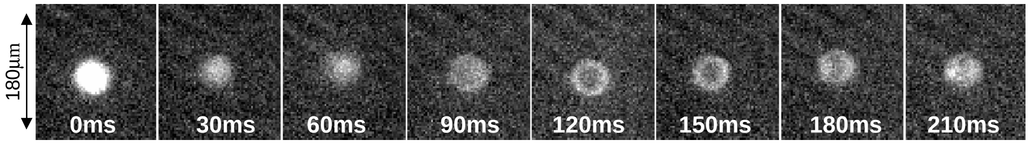

Figure 3.4: Nondestructive imaging of mean-field-induced spin segregation in a two-component condensate, comprised of the internal spin states $|1\rangle$ and $|2\rangle$. The frequency of the probe laser is tuned such that it is primarily sensitive to the presence of the $|1\rangle$ state, which appears bright. At $t = 0$, the condensate is in $|1\rangle$, after which a short coupling pulse transfers $\sim$1/2 the population to $|2\rangle$. The internal spin states are simultaneously trapped in a spherical, harmonic magnetic trap ($\omega \sim 2\pi 8$Hz). The spherical symmetry causes a radial spin segregation into a $|1\rangle$ shell around a $|2\rangle$ ball by 120ms. The mutual density oscillations continue to later times.

chapter. After a short $\pi/2$ pulse of the two-photon drive creates an initially uniform superposition of the two states, they separate radially into a ball-and-shell structure with the $|1\rangle$ fluid exterior to the $|2\rangle$'s. The $|1\rangle$ state in other words has a slightly greater buoyancy than the $|2\rangle$ state. The mutual density oscillations continue about the equilibrium ball-and-shell configuration with a characteristic time scale for the initial phase separation of roughly the harmonic trap period or 120ms.

In the hierarchy of time scales, the last effect noted here, which ultimately limits the kinds of behaviour that may be observed, is the magnetic trap loss of the two components due to inelastic collisons. In the first place, the situation is not as bad as perhaps might initially be expected. The fortuitous suppression of spin-exchange collisions in ^{87}Rb allows for the simultaneous coexistence of the $|1\rangle$ and $|2\rangle$ states without rapid loss [128]. The individual lifetime of a $|1\rangle$-state condensate in the typical spherical trap ($\omega_{trap} = 2\pi$ 8Hz) is $\sim$50s, most likely limited by collisions with hot background gas.[1] A condensate in the $|2\rangle$ state has a considerably shorter density-dependent lifetime of about 1s. This is due to the availability of collisional channels to magnetically untrapped states via spin exchange. The lifetime of the $|2\rangle$ state is a not-so-generous experimental

---

[1] Loss in condensate fraction from sample heating can be suppressed by the continuous application of forced evaporative cooling. Empirically, this is found to somewhat improve the lifetime of a $|1\rangle$-state condensate.

limit since only a few trap periods worth of dynamics may occur before the $|2\rangle$ atoms are depleted. On the other hand, for single-component vortex experiments involving the $|1\rangle$ state only, the time available is essentially “forever”.

3.3 Wavefunction engineering with two-component condensates

3.3.1 The idea

It has already been mentioned that the wavefunction engineering technique is associated with two-component condensates. However, some limited manipulation of the condensate wavefunction is possible with single-component condensates alone. Dark solitons in particular have been experimentally realized in this way [58, 73]. As a macroscopically occupied wavefunction, a single-component condensate has an associated scalar order parameter with a well-defined amplitude and phase at each point in space. One can spatially modify the phase using the intensity-dependent ac Stark shift induced by an off-resonant laser [Figure 3.5]. The size of a typical trapped condensate (10-100μm) is large enough that it can be imprinted with intricate Stark-induced phase patterns, limited in detail only by the wavelength of the illuminating laser ($\lambda \sim 1\mu$m). This technique provides access only to the phase, leaving the condensate density to rearrange itself via dissipative dynamics after the imprinting is complete. One hopes that the density evolution is sufficiently well-bounded that the desired target state survives the dynamics. This is by no means guaranteed since the target state has a higher energy in general than the ground state.

Coupled two-component condensates provide a means to control both the amplitude and the phase of the wavefunction engineered. As was shown in Figure 3.3, a coupling drive coherently transfers population between spin states uniformly across a condensate. The aim of wavefunction engineering is to control the amplitude and phase of the coherent transfer in a spatially dependent way. To develop a simple model, the

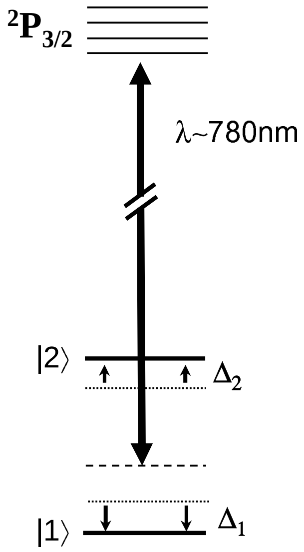

Figure 3.5: The ac Stark shift of ground hyperfine states in ^{87}Rb due to a laser detuned from resonance with the excited electronic state $5P_{3/2}$.

two-photon Rabi frequency [Eqn. 3.2] is assumed to be sufficiently large that population transfer between the spin states occurs quickly compared to the mean-field driven component separation in the trap. Under these circumstances, a simple “nailed down” picture can be considered in which the two-component dynamics are described by a local two-level system fixed at each point in space.

The means to control the population transfer in the two-level system is again the laser-induced ac Stark shift, which serves to alter the energy splitting between the two levels [Figure 3.5] thereby affecting the detuning with respect to the coupling (two-photon) drive. At least two control parameters are required to influence both the amplitude and phase of the transfer. This results in a more sophisticated scheme than phase imprinting whereby the incident intensity is *modulated* with characteristic parameters of the dynamic control being the amplitude and phase of modulation. To obtain spatially selective control over the population transfer, one can imagine using a spatial light modulator array to put an arbitrary two-dimensional light pattern onto the condensate. This amounts to focusing a laser beam at each point in the condensate

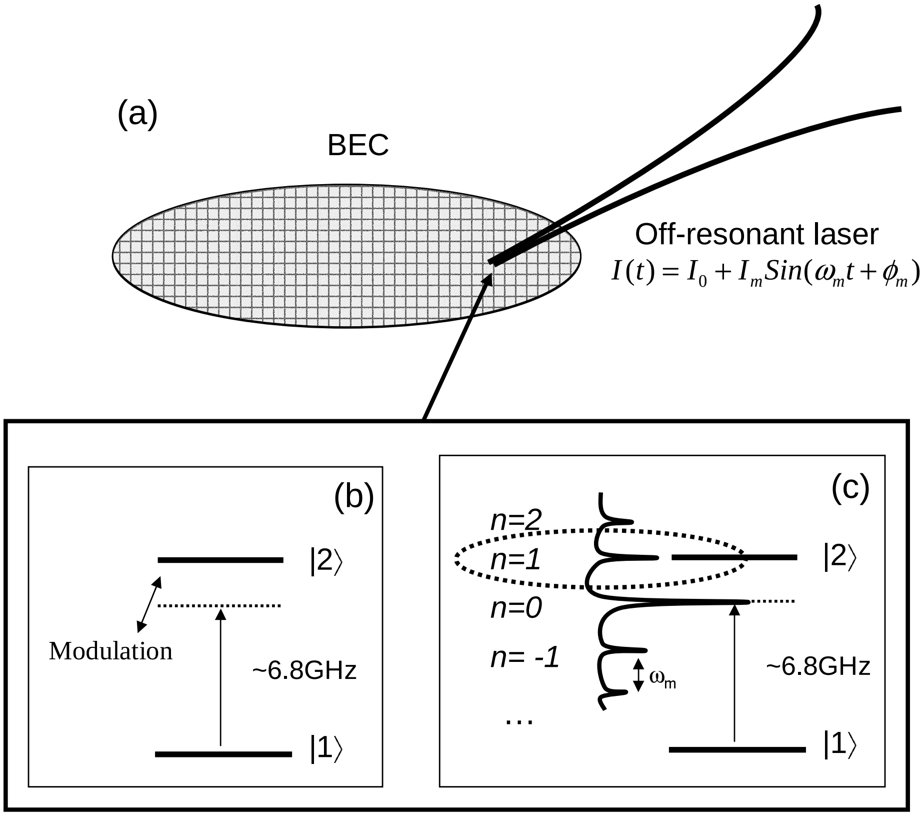

Figure 3.6: Local wavefunction engineering in a two-component condensate. (a) An off-resonant laser with modulated intensity is focused at a particular point in the condensate. The oscillating intensity modulates the local resonance between internal hyperfine states $\{|1\rangle, |2\rangle\}$ via the ac Stark effect. In the presence of a coupling drive, this is equivalent to the modulation of the drive (b), which acquires sidebands at multiples of the carrier frequency. A resonant sideband (c) allows coherent population transfer between the spin states. Control of the sideband amplitude and phase allows control of the amplitude and phase of the locally transferred population (see text).

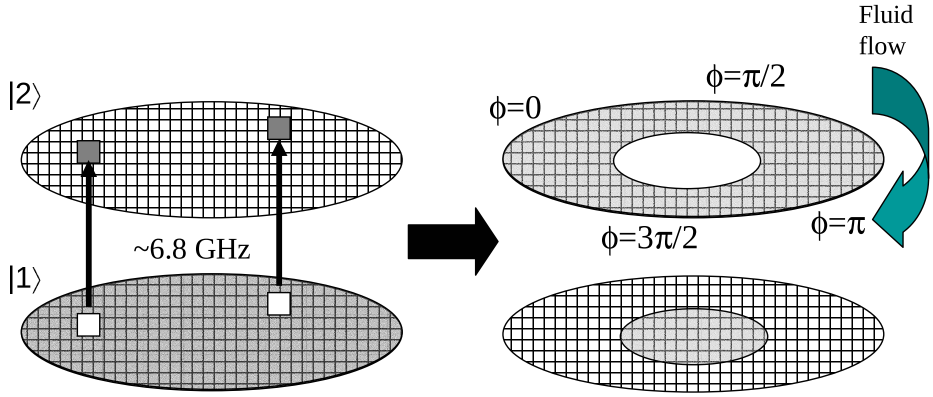

Figure 3.7: Point-by-point wavefunction engineering in a two-component condensate to construct a singly quantized vortex.

[Figure 3.6]. Modulating the laser intensity at each point in the condensate dithers the two-level resonance of the atoms. Equivalently the coupling drive itself can be considered to be locally modulated, putting FM sidebands onto the carrier frequency at integer multiples of the modulation frequency. Thus it now becomes possible to couple resonantly to the atoms using not only the carrier frequency but also one of the sidebands [Figure 3.6]. If a sideband is tuned to the two-level resonance, the rate of the resulting population transfer may be controlled by the strength of the sideband, which is directly related to the modulation depth of the laser intensity at that point. While the control of transfer amplitude is straight forward, what is truly remarkable is that the phase of the transferred population can also be controlled in a completely deterministic way - by the choice of modulation phase. This means that the modulation parameters of amplitude and phase may be dialed into the spatial light modulator pixel-by-pixel to produce the desired (two-dimensional) condensate wavefunction in the final internal spin state [Figure 3.7]. Once the transfer to the target wavefunction is complete, the "scaffold state" formed by the remaining population in the initial spin state can (if desired) be selectively blown away with the light pressure from an on-resonant laser.

3.3.2 A closer look

Since the direct control of population amplitude and phase through associated modulation parameters is so fundamental a point, it is shown explicitly for the two-level system at a particular point in the condensate. The model imagines a two-level system $\{|1\rangle,|2\rangle\}$ with resonant frequency ω_0 at about 6.8GHz and a coupling drive characterized by frequency ω and bare Rabi frequency Ω_0. The resonance is Stark modulated as

$$\omega_0(t) = \omega_0 + \alpha_m \sin(\omega_m t + \phi_m) \tag{3.3}$$

with modulation frequency ω_m, amplitude α_m and phase ϕ_m. The value of ω_0 includes the time-averaged Stark shift of the states. There are four system parameters to account for, namely the amplitude and phase of both states $|1\rangle$ and $|2\rangle$. The total population in the two-level system is conserved; thus only the population difference, $p_2 - p_1$, matters. Initially the state begins in a single spin state. The phases may be separated into the phase of the initial state and the phase of the target state referenced to the initial. As long as the time-averaged Stark shift is the same across the condensate, there is only an isotropic phase shift to the initial state, which can be considered a spatially flat phase reference. As an additional caveat, the notion of a spatially flat phase reference holds only initially when population is being transferred *from* the initial state everywhere in the condensate. Once the population begins to be transferred back to the initial state at some points in the condensate, the phase evolution gets complicated (see below). Except for Section 3.9, the wavefunction engineering focuses on the regime where population is still being transferred from the initial state; thus, we need care only about the population difference and relative phase ϕ to understand the structure of the final state's wavefunction. A particularly powerful pictorial way to understand the dynamics of these two variables is the Bloch picture [49] where the system is characterized by a pseudospin vector $\vec{s}$ in a three-dimensional space [Figure 3.8]. The vertical $\hat{3}$-axis represents the population difference and the azimuthal angle in the horizontal plane indicates

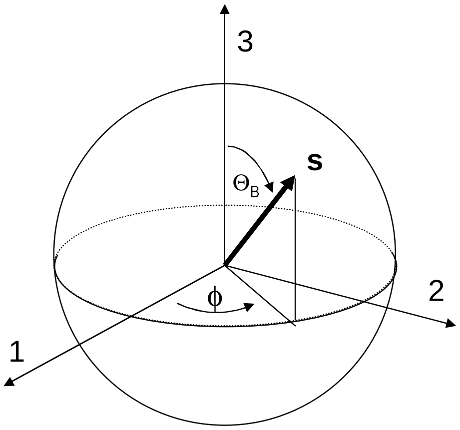

Figure 3.8: Bloch sphere

the relative phase. In terms of the well-known one-to-one correspondence of a two-level system with a spin-1/2 system, the Bloch vector axes represent the expectation values of the Pauli spin components, $s_i = \langle\sigma_i\rangle$.

It is important to note that the Bloch-sphere representation suffers from a limitation in that the relative phase is undefined for a pseudospin pointing along either of the poles. Only away from the poles where population exists for both states of the two-level system is the relative phase a meaningful quantity. In fact, the loss of a well-defined relative phase at the poles is necessary since there is a π phase change in ϕ as the pseudospin traverses a pole. The phase change is associated with the state whose population vanishes at the given pole. (See Section 3.9 for a physical implication of this effect).

The situation of a coupled two-level system in the absence of modulation ($\alpha_m = 0$) is reviewed first because it provides a paradigm for the solution with modulation. The approach follows closely that of ref. [49]. The equations of motion for the pseudospin in the presence of a coupling drive may be written as a torque problem

$$\frac{d}{dt}\vec{s}(t) = \vec{\Omega}_L(t) \times \vec{s}(t) \tag{3.4}$$

where the torque vector is oscillating in time

$$\vec{\Omega}_L(t) = \begin{pmatrix} -\Omega_0 e^{-i\omega t} + c.c. \\ 0 \\ \omega_0 \end{pmatrix} \tag{3.5}$$

The bare Rabi frequency Ω_0 is given by Eqn. 3.2. If the drive is not too far detuned from resonance ($|\omega - \omega_0| \ll \omega_0$), the problem can be solved to a very good approximation by transforming into a frame rotating about the $\hat{3}$-axis at the drive frequency ω and then performing a time-average to eliminate all rapidly oscillating torque components. This so-called "rotating-wave approximation" is justified since the fast oscillating components will have no cumulative effect on the pseudospin over time. What remains after the time-averaging is again a torque equation for the pseudospin $\vec{\rho}(t)$ in the rotating frame

$$\frac{d}{dt}\vec{\rho}(t) = \vec{\Omega} \times \vec{\rho}(t) \tag{3.6}$$

but now with a constant torque

$$\vec{\Omega} = \begin{pmatrix} -\Omega_0 \\ 0 \\ -\delta \end{pmatrix} \tag{3.7}$$

where $\delta = \omega - \omega_0$ is the detuning[2] [Figure 3.2]. Since the rotating frame, called here the "standard" Bloch frame, differs from the lab frame by a trivial (time-dependent) rotation about the $\hat{3}$-axis, the phase difference between the states can without loss of generality be associated with the azimuthal angle in the standard frame. The solution to Equation 3.6 is just a rotation of the pseudospin about the torque direction

$$\vec{\rho}(t) = \overset{\leftrightarrow}{R}(t)\, \vec{\rho}_R \tag{3.8}$$

with $\vec{\rho}_R$ being a constant vector characteristic of the initial conditions. The expression

---

[2] The detuning differs by a minus sign from the definition in [49].

for the rotation matrix $\overleftrightarrow{R}(t)$ is:

$$\overleftrightarrow{R}(t) = \begin{pmatrix} \frac{\Omega_0^2+\delta^2\cos\theta(t)}{\Omega^2} & \frac{\delta}{\Omega}\sin\theta(t) & \frac{\delta\Omega_0}{\Omega^2}(1-\cos\theta(t)) \\ \frac{-\delta}{\Omega}\sin\theta(t) & \cos\theta(t) & \frac{\Omega_0}{\Omega}\sin\theta(t) \\ \frac{\delta\Omega_0}{\Omega^2}(1-\cos\theta(t)) & \frac{-\Omega_0}{\Omega}\sin\theta(t) & \frac{\delta^2+\Omega_0^2\cos\theta(t)}{\Omega^2} \end{pmatrix} \tag{3.9}$$

The effective off-resonant Rabi frequency Ω and the argument $\theta(t)$ are identified as

$$\Omega = |\vec{\Omega}| = \sqrt{\Omega_0^2+\delta^2}, \qquad \theta(t) = \Omega t \tag{3.10}$$

The general dynamical behaviour, corresponding to Rabi oscillations, involves precession of the pseudospin $\vec{\rho}$, which traces out a cone centered on the torque vector $\vec{\Omega}$. For example, at the start of the coherent control process, the population of the two-level system is all in one state. For the case of the $|2\rangle$ state, this corresponds to a pseudospin vector pointing along the north pole of the Bloch sphere. The coupling drive is far detuned ($|\delta| \gg \Omega_0$) such that the torque vector [Eqn. 3.7] is also nearly aligned with the north pole. In the absence of any modulation, the pseudospin will precess in a tight circle about the torque direction [Figure 3.9]. The deviation of the pseudospin from its initial vertical orientation is small, as one would expect, since the large detuning of the drive permits little population transfer to the final state.

A time-dependent detuning is now added in accordance with Eqn. 3.3

$$\delta(t) = \delta_0 + \alpha_m \sin(\omega_m t + \phi_m) \tag{3.11}$$

As a result, it is now necessary to solve for the pseudospin dynamics in the presence of an oscillating torque. In similar fashion to the original Rabi problem, the torque oscillations are expected to drive a slow tipping of the pseudospin at a new effective Rabi frequency Ω_C, which characterizes the rate of population transfer for the coherent control. Continuing with the analogy to the Rabi problem, a separation of time scales is evident between the instantaneous spin precession rate at Ω and the slow accumulated spin tipping at Ω_C. Using the standard technique to reduce the number of fast-oscillating

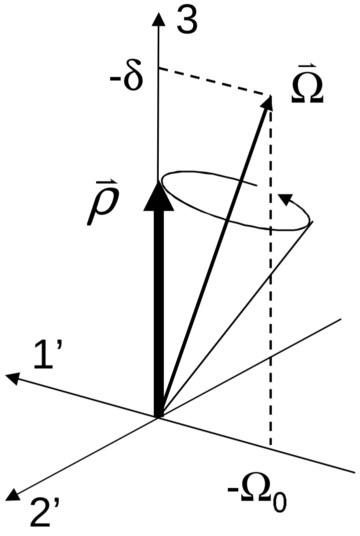

Figure 3.9: Rabi oscillations on the Bloch sphere in the standard rotating frame (see text). The pseudospin $\vec{\rho}$ precesses in time, tracing out a cone about the torque vector $\vec{\Omega}$.

variables, a transformation is made into the instantaneous moving frame of the torque vector, sometimes called the "quasi-static basis." The moving frame is both rotating and dithering in space. As a result the transformation matrix $\overleftrightarrow{R}(t)$ [Eqn. 3.9] acquires extra time dependence through

$$\begin{aligned} \Omega \rightarrow \Omega(t) &= \sqrt{\Omega_0^2 + \delta(t)^2} \\ \theta(t) &= \int^t \Omega(t')dt' \end{aligned} \tag{3.12}$$

and $\vec{\rho}_R$ of Eqn. 3.8, originally constant, becomes compensatorily time dependent. To obtain the equation of motion in the co-moving frame, the torque equation 3.6, including a time-dependent detuning, is first written in matrix form and then expanded using $\vec{\rho}(t) = \overleftrightarrow{R}(t)\vec{\rho}_R(t)$. The resulting equations of motion for the pseudospin $\vec{\rho}_R$ in the co-moving frame are

$$\frac{d\vec{\rho}_R}{dt} = -\left(\overleftrightarrow{R}^{\dagger} \frac{\partial \overleftrightarrow{R}}{\partial \Omega} \frac{\partial \Omega}{\partial t} \right) \vec{\rho}_R \tag{3.13}$$

To obtain an analytical understanding of these equations we consider the limit where the time-averaged detuning δ_0 is large compared to both the bare Rabi frequency Ω_0

and the modulation amplitude α_m. After an expansion to first order in α_m and Ω_0, the time-average of the equations of motion [Eqn. 3.13] can (once again!) be written as an effective torque equation:

$$\frac{d}{dt}\vec{\rho}_R(t) = \vec{\Omega}_C \times \vec{\rho}_R(t) \tag{3.14}$$

The time-averaged torque $\vec{\Omega}_C$ in the co-moving frame has components:

$$\begin{aligned}
\Omega_{C1} &= -sign(\delta_0)\alpha_m \frac{\omega_m \Omega_0}{\Omega^2}\left\langle \sin(\omega_m t + \phi_m)\sin\left(\Omega t + \frac{\alpha_m}{\omega_m}\sin(\omega_m t + \phi_m)\right)\right\rangle_t \\
\Omega_{C2} &= \alpha_m \frac{\omega_m \Omega_0}{\Omega^2}\left\langle \sin(\omega_m t + \phi_m)\cos\left(\Omega t + \frac{\alpha_m}{\omega_m}\sin(\omega_m t + \phi_m)\right)\right\rangle_t \\
\Omega_{C3} &= 0 + \mathcal{O}\left(\frac{\Omega_0^2}{\Omega^2}\right)
\end{aligned} \tag{3.15}$$

The righthand side of the above expressions can be expanded in Bessel functions, which are the familiar feature one obtains for all problems involving frequency modulation. "Resonances," defined by a non-zero average torque, will occur when the modulation frequency is an integer fraction of the effective Rabi frequency

$$\omega_m = \frac{\Omega}{n}, \quad n \in \pm 1, \pm 2 \ldots \tag{3.16}$$

The integer n refers to the index of the FM sideband being used for coupling [Figure 3.6]. The first two resonances are evaluated as follows, corresponding to coupling via the first two sidebands:

$$\begin{aligned}
\omega_m = \Omega \quad &\rightarrow \quad \vec{\Omega}_C = -\frac{\alpha_m \Omega_0}{2\Omega} J_0\left(\frac{\alpha_m}{\omega_m}\right)^2 \begin{pmatrix} sign(\delta_0)\cos\phi_m \\ -\sin\phi_m \\ 0 \end{pmatrix} \\
\omega_m = \frac{\Omega}{2} \quad &\rightarrow \quad \vec{\Omega}_C = \frac{\alpha_m \Omega_0}{2\Omega} J_1\left(\frac{\alpha_m}{\omega_m}\right) J_0\left(\frac{2\alpha_m}{\omega_m}\right) \begin{pmatrix} sign(\delta_0)\cos 2\phi_m \\ -\sin 2\phi_m \\ 0 \end{pmatrix}
\end{aligned} \tag{3.17}$$

Only the lowest order Bessel term has been retained for these expressions. The direction of the torque $\vec{\Omega}_C$ is referenced to the moving frame; however, under the approximation already made that the average detuning is large and the modulation depth relatively small, the moving frame is nearly equivalent to the standard Bloch frame within a trivial rotation about the $\vec{3}$-axis. (This can be seen by setting α_m and Ω_0 to zero in the transformation matrix $\overleftrightarrow{R}$ [Eqn. 3.9].) As a result, the time-averaged torque can be interpreted in the same way as for the familiar Rabi problem. This provides the remarkable conclusion that, when a sideband is resonant, $\vec{\Omega}_C$ lies in the horizontal Bloch plane and has an azimuthal orientation controlled by the modulation phase. For the first sideband resonance the azimuthal angle is (within a sign) given by the modulation phase; for the second sideband it is twice the modulation phase and so on. Clearly, by controlling the orientation of the torque vector the pseudospin can be pointed in an arbitrary direction in the horizontal plane, or, in more physical terms, population can be transferred in the two-level system with a deterministic arbitrary phase [Figure 3.10].

The amplitude of the time averaged torque, which corresponds to a new effective Rabi frequency Ω_C, is directly proportional to the bare Rabi frequency Ω_0 and, most importantly, the modulation amplitude α_m. Thus, the amount of population transferred over a given time can be directly controlled by the modulation depth. As a side note, from the Bessel dependence it is clear that the second FM sideband resonance is considerably suppressed relative to the first in the low modulation regime ($\alpha_m/\omega_m \lesssim 1$).

Concentrating on the first sideband, the prescription for wavefunction engineering of a two-component condensate is straightforward: apply off-resonant laser light at each point in space to modulate the local two-component resonance. For each point, dial in the amplitude and phase of modulation to obtain the desired amplitude and phase for the wavefunction transfer. Direct point-by-point control is a novel feature of coherent control with condensates and is due to the large size of the macroscopic wavefunction (10-100μm) relative to the wavelength ($\sim$1μm) of the laser addressing it. It is interesting to compare this situation to coherent control techniques in other atomic and molecular systems, including the engineering of electronic wave-packets in Rydberg atoms [157]

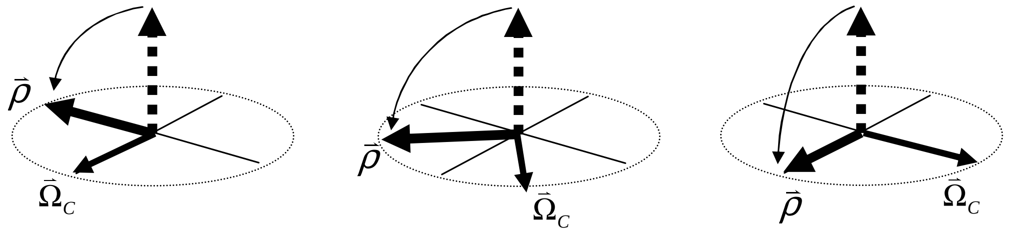

Figure 3.10: Coherent control of the pseudospin $\vec{\rho}$ on the Bloch sphere. The azimuthal angle of the pseudospin can be controlled with the orientation of effective torque vector $\vec{\Omega_C}$ (see text). Three different orientations are illustrated. A particular *polar* angle of the pseudospin can also be achieved by applying the torque for the required amount of time.

and vibrational wave-packets in molecules [92]. In both cases the $\sim 1\mu$m wavelength of the short-pulsed laser incident on the system is much larger than the typical size of the system, measured in Bohr radii. Therefore, coherent control is achieved in a different way. The large bandwidth of the laser pulses is used to couple to the superposition of energy states required to construct the target wavefunction [Figure 3.11]. One can consider wavefunction engineering in this fashion to be analogous to Fourier wave optics whereas the point-by-point manipulation of the condensate describes the complementary case analogous to ray optics.

3.3.3 Experimental realization: single vortex formation

The implementation of wavefunction engineering within the system $\{|1\rangle,|2\rangle\}$ begins with a two-photon drive characterized by a bare Rabi frequency[3] of $\Omega_0 \sim 33$Hz and a detuning of $\sim$100Hz from resonance, giving an effective off-resonant Rabi frequency of $\Omega \sim 100$Hz. The coherent control makes use of the first sideband resonance ($\omega_m = \Omega \sim 100$Hz) as it provides the strongest coupling. There exist a number of technological possibilities to generate the spatially and temporally modulated pattern of laser intensity necessary to create arbitrary condensate wavefunctions. As mentioned

---

[3] Ω_0 is kept at a low value to suppress the magnitude of inhomogeneities in its value across the condensate. The inhomegeneities arise from the magnetic trapping potential [Section 3.9].

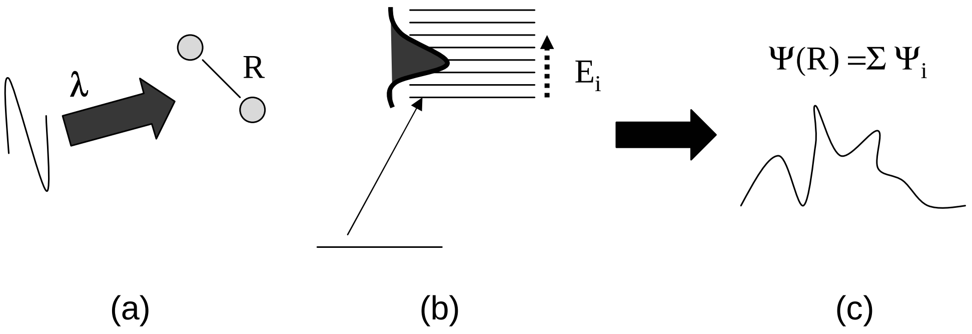

Figure 3.11: Wavefunction engineering in"Fourier space." The cartoon illustrates the creation of a vibrational wavepacket in a diatomic molecular system with a short pulsed laser. (a) A laser pulse is incident on the molecule. (b) The frequency bandwidth of the pulse allows coupling to many vibrational states. (c) Shaping the frequency spectrum of the pulse allows the creation of the desired target state $\Psi(R)$ as superposition of vibrational modes Ψ_i.

earlier, a two-dimensional liquid crystal modulator provides the "ultimate" general solution. Simpler techniques, however, exist to create the topological features of immediate interest, namely solitons and vortices. To make a singly quantized vortex, which is a donought shape with a 2π azimuthal phase winding, a spatially dependent intensity modulation is required that increases from zero away from the cloud center and has a 2π phase dependence azimuthally. These specifications exactly describe a linear slope of light intensity rotating about the center of the condensate. This is accomplished in practice by rotating a laser beam that is offset from the condensate center [Figure 3.12]. Since the rotation(i.e. modulation) frequency is a modest ∼100Hz, a pair of piezo-actuated mirrors provides a convenient and simple means to move the "sculpting" beam in two-dimensions [Figure 3.12]. To minimize any spatially dependent phase-imprinting effect from the *time-averaged* beam profile, the radius of beam rotation is chosen to be ∼3/4 of its waist. This results in a uniform time-averaged intensity profile across the condensate extent. Typical beam parameters include a waist size of 95μm, total power of ∼10nW, and a laser frequency ∼1100MHz below the $F = 1 \rightarrow F' = 0$ transition [Figure 2.4]. These parameters yield an average ac Stark shift across the condensate of typically 60Hz (taken into account in the two-photon drive frequency) and a peak modulation amplitude at the condensate edge (R$\sim$25μm) of 45Hz or $\sim$0.45Ω.

The condensate begins in a single initial spin state, chosen as either $|1\rangle$ or $|2\rangle$. The coupling drive is sufficiently far detuned ($\sim 3\Omega_0$) that negligible population transfer occurs in the presence of the drive alone. However, when the sculpting beam is applied and the two-photon drive is tuned to within a few Hz of the first sideband, coupling to the final spin state occurs. As expected, population is transferred into the donought shape of a vortex surrounding a core of the initial spin state [Figure 3.13]. The process is continued for 50-70ms yielding a typical transfer efficiency of 50%. A vortex can be successfully created starting with either internal state [Figure 3.13] although one would expect that driving to the $|1\rangle$ state is preferable because it has a longer lifetime and its situation outside a $|2\rangle$ core is the natural one in terms of the components' buoyancies (Compare Figures 3.13(b)&3.4). In any case, vortices are habitually formed by driving to the $|1\rangle$ state. If a $|2\rangle$ vortex is desired, a short (4ms) π pulse from a strong two-photon drive can be subsequently applied to flip the spin composition of vortex and core.

To obtain a reasonable transfer rate at the first sideband, the bare Rabi frequency Ω_0 and peak modulation depth α_m are a reasonable fraction of the two-photon detuning. This results in local residual Rabi oscillations during the engineering process [Figure 3.14]. Within one Rabi cycle ($\sim$10ms), a partial transformation of the final population occurs to a crescent shape that appears to rotate around the cloud. However, the non-symmetric crescent shapes are avoided by stopping the engineering process after an integer multiple of the average effective Rabi period ($2\pi/\Omega$). At such points in time, neglecting technical imperfections, all azimuthal points must have experienced the same evolution and the state must be symmetric, which it is in practice [Figure 3.14].

"By construction," the wavefunction engineering should make a vortex with a 2π winding as indicated by the simulation [Figure 3.13(d)]. The phase winding can be experimentally verified with an interferometric technique that couples the two components

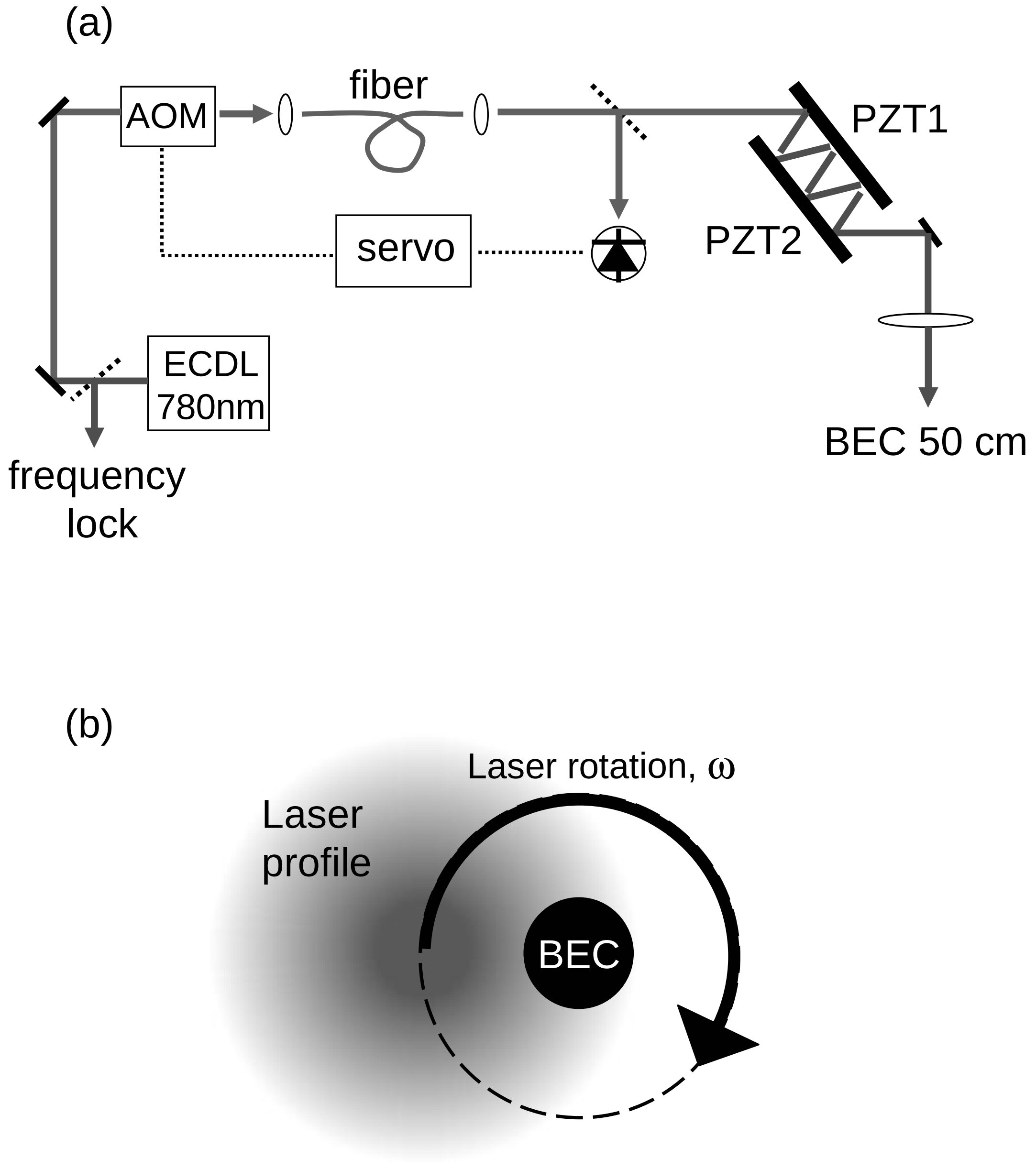

Figure 3.12: Sculpting beam setup for wavefunction engineering. (a) The output of an external cavity diode laser (ECDL) is passed through an acousto-optic modulator (AOM) to provide control of the laser power. The light is transported to near the condensate via optical fiber, providing some spatial mode cleaning as well. A small amount of light is split off after the fiber to servo the laser power. A pair of piezo-mounted mirrors, PZT1 and PZT2, allow the beam to be moved in two dimensions with an arbitrary pattern. Three bounces between the mirrors provide amplification of the beam's motion. The beam is then weakly focused onto the condensate to create, for example, a rotating beam (b) for vortex engineering.

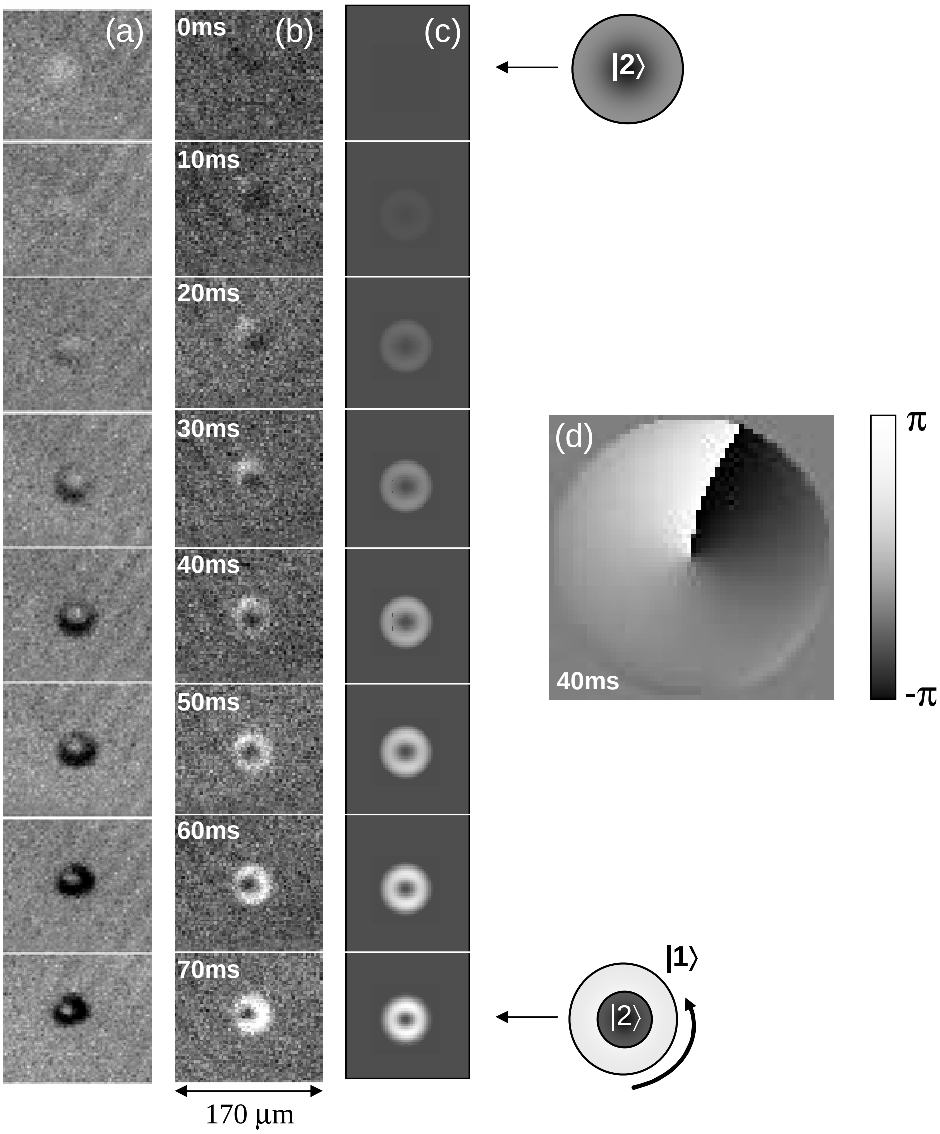

Figure 3.13: (a)&(b) Nondestructive imaging of vortex growth during the process of wavefunction engineering in a trapped two-component condensate. Images are taken at taken at 10 ms intervals corresponding to one period of the effective off-resonant Rabi oscillations present in the condensate. A vortex may be created in the internal $|2\rangle$ state (a) or $|1\rangle$ (b). In each case, the frequency of the probe laser is tuned to be primarily sensitive to the state containing vorticity. (c) A numerical simulation of the local Bloch equations [Eqn. 3.6] with detuning modulation across the condensate is shown for comparison. Parameters of the simulation, typical of those in the experiment, are as given in the text. (d) The phase difference between the internal states is shown for the simulation at t=40ms and may be interpreted as the phase of the final spin state. Although not perfectly uniform radially, the phase pattern clearly predicts the 2π azimuthal phase wrap of a singly quantized vortex.

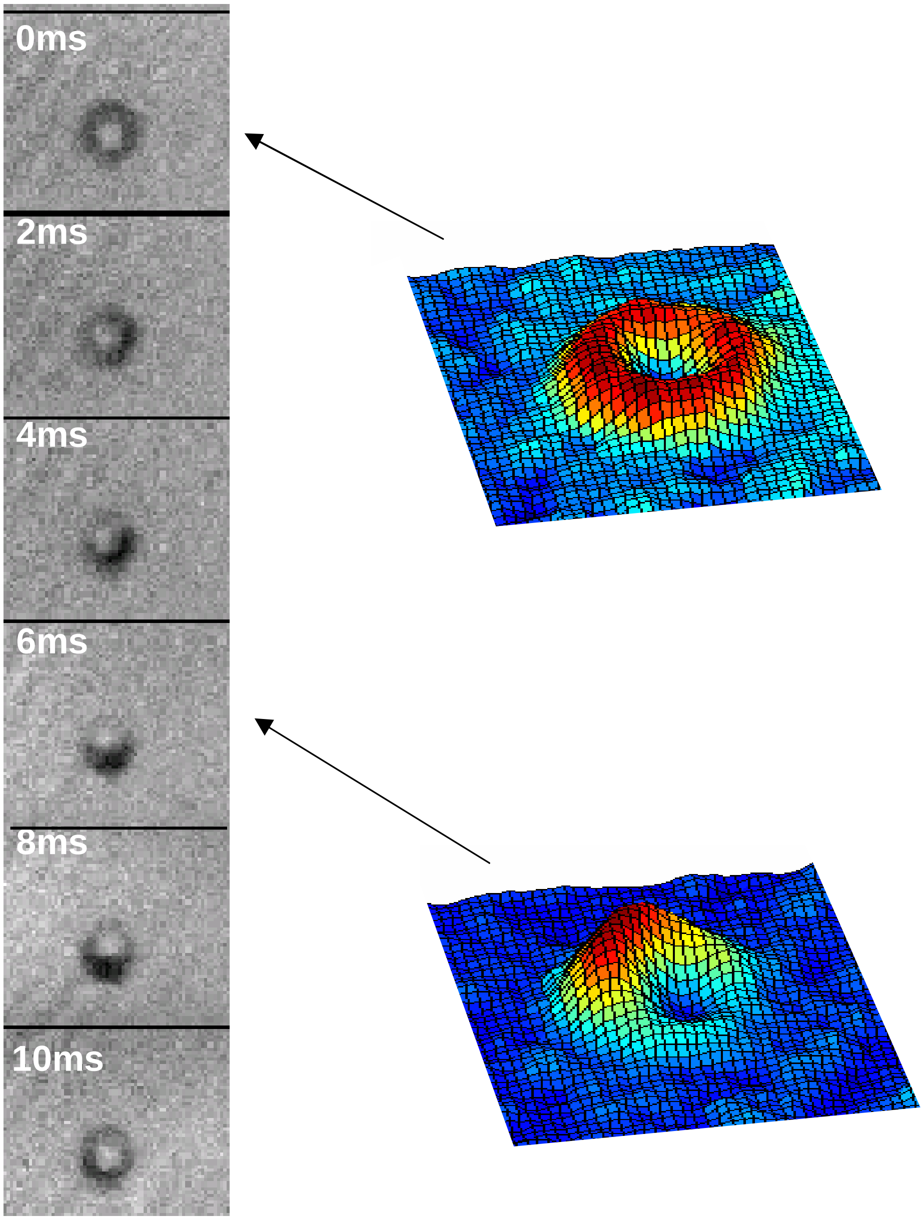

Figure 3.14: Nondestructive imaging showing the residual local Rabi oscillations during the growth of a vortex, in this case in the $|2\rangle$ state. The image series spans one cycle of the average off-resonant Rabi frequency (Ω=100Hz). At times (e.g. t=0ms) corresponding to an integer multiple of the Rabi period, the $|2\rangle$ fluid forms a symmetric ring corresponding to a centered vortex.

where the densities of the core and vortex overlap. This was done for the first demonstration of vortex creation [122]. It is not discussed again here as two more heavily used vortex diagnostics are already presented in later sections.

The handedness of the vortex created can be changed by reversing the rotation of the sculpting beam, but this is not done in practice. For a fixed beam rotation direction, the vortex handedness can also be chosen with the sign of the average two-photon detuning [Eqn. 3.17], which is demonstrated experimentally in Section 3.6.

The long term stability of the engineering process has been improved by a slow intensity servo applied to the sculpting beam [Figure 3.12]. Residual difficulties include the slow thermal drift of the piezoelectric elements, which could ultimately be stabilized with a beam-pointing servo. By far, however, reproducibility of the vortex formation is most adversely affected by undesirable center-of-mass motion ("slosh") of the condensate. This causes both shot-to-shot variations in the relative position between the condensate and sculpting beam as well as relative motion during the engineering process. Typically, the result is the creation of an off-center vortex. Careful attention is required on a day-to-day basis to minimize slosh as much as possible. Many shots (with a $\lesssim$1min cycle time) are still needed to obtain a collection of reasonably well-centered vortices. For this reason, a good deal of effort is made to assure that all aspects of the experiment are stable over long periods of time, including condensate formation, beam intensity, and so on.

3.4 Dynamical stability of two-component vortices

While it is essentially irrelevant which spin state is used initially to create a two-component vortex [Figure 3.13], differences in the interparticle interactions of the two components [Section 3.2] produce a stark dichotomy of dynamical behaviour depending on the spin composition of the vortex and core. For convenience, the notation (1,0) denotes the case of a $|1\rangle$ vortex and $|2\rangle$ core while (0,1) denotes the opposite configuration. On a simple level, a vortex in the $|2\rangle$ state will certainly be destroyed more quickly due to the faster collisional loss of $|2\rangle$ atoms from the magnetic trap; however, a more interesting issue is the *dynamical* stability of a two-component vortex given that the two fluids can exchange angular momentum through their mutual interactions. A simplified analytical model by Pérez-García and García-Ripoll [90, 135] evokes the qualitative behaviour, which is shown to depend on two factors: the spin component hosting the vortex, and, interestingly, the relative population N_1/N_2 of the components. A stability condition is derived for the (1,0) configuration as

$$\left(\sqrt{\frac{N_1}{N_2}} - 1\right)^2 > 1 - \frac{a_{11}}{a_{22}} \tag{3.18}$$

For ^{87}Rb, the values of the intra-species scattering lengths, a_{ii} [Section 3.2] are such that the stability condition is satisfied for any population distribution amongst the spin components. The opposite configuration (0,1) is stable if

$$\left(\sqrt{\frac{N_2}{N_1}} - 1\right)^2 > 1 - \frac{a_{22}}{a_{21}} \tag{3.19}$$

For ^{87}Rb this inequality fails over the range of populations $N_1/N_2 \in [0.73, 1.49]$.

The stability of the two different vortex configurations has first been compared under the experimental condition of a roughly equal population distribution between vortex and core [Figure 3.15]. The (1,0) configuration remains stable over time whereas, in the (0,1) case, the $|2\rangle$ vortex crushes inward under the influence of its negative bouyancy. The $|2\rangle$ vortex fragments into two pieces, never healing into an intact ring shape in subsequent dynamics.

For a sufficiently small $|1\rangle$ core, the stability condition for the (0,1) configuration will be satisfied. In order to approach this regime experimentally, a vortex has first been created in the (1,0) state. The $|2\rangle$ core can then be reduced slowly over $\sim$1s through its inherent decay or quickly ($\lesssim$10ms) through the application of a short blast of selectively resonant laser light. In either case, a 4ms two-photon π pulse is then administered to

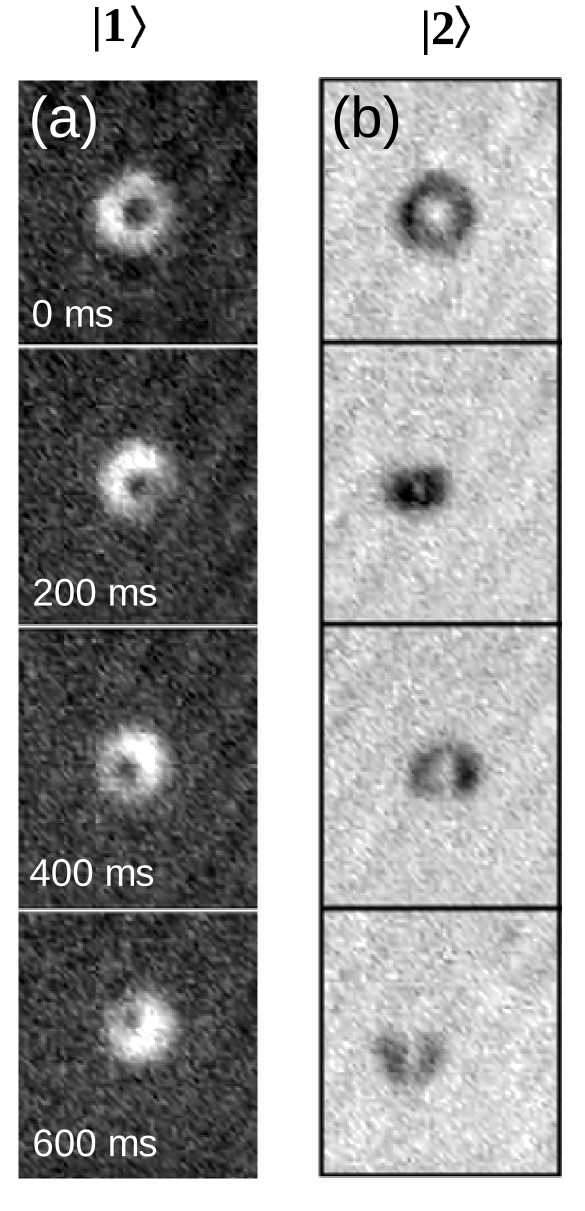

Figure 3.15: Dynamical stability of two-component vortices.(a) The free evolution of a $|1\rangle$ vortex (i.e. (1,0) state) in the magnetic trap. It is stable over a time long compared to the trap oscillation period (128 ms). (b) The free evolution of a $|2\rangle$ vortex (i.e. (0,1) state) is much more dynamic. It is seen shrinking quickly into the invisible $|1\rangle$ core and rebounding into fragments. Each column is from a single run, where the times indicated are referenced to the end of vortex creation. In these pictures the states appear differently with respect to the background due to the different signs of the imaging light detuning.

switch the spin-composition of the vortex from (1,0) to (0,1). This essentially instantaneous spin flip provides a sharp initial time for the subsequent evolution of the (0,1) configuration.

Figure 3.16 presents typical results where one image sequence involves a moderately sized $|1\rangle$ core while the two remaining sequences are for a small $|1\rangle$ core. In the case of the larger core, the two components separate into two pieces with the $|1\rangle$ fluid moving outward to edge of the condensate. The two components continue to rotate around one another to preserve the total angular momentum of the system. The theory of [90, 135] predicts that the instability of the initial (0,1) configuration should induce an oscillation between (0,1) and (1,0) in which the components fully exchange angular momentum. The predicted intermediate state of two rotating halves sharing angular momentum appears similar to that observed in Figure 3.16(a); however, the continued evolution to the (1,0) configuration has not been seen experimentally. Indeed, the fact that the $|2\rangle$ vortex fragments into a single rather than two pieces as in Figure 3.15(b) may be attributed to a radial bias in the initial core position introduced by the engineering process.

For the case of a small $|1\rangle$ core [Figure 3.16(b)and (c)], the mutual mean field energy clearly is sufficiently reduced that the (0,1) configuration is stable. The $|1\rangle$ atoms remain confined within the $|2\rangle$ fluid and track the core as it precesses around the condensate center in the direction of the vortex flow [see Section 3.5]. In the image sequence of Figure 3.16(c) it may even be possible to distinguish a “Matryoshka nested doll” configuration in which the $|1\rangle$ core itself is filled with a small amount of $|2\rangle$ fluid trapped inside due to its negative buoyancy.

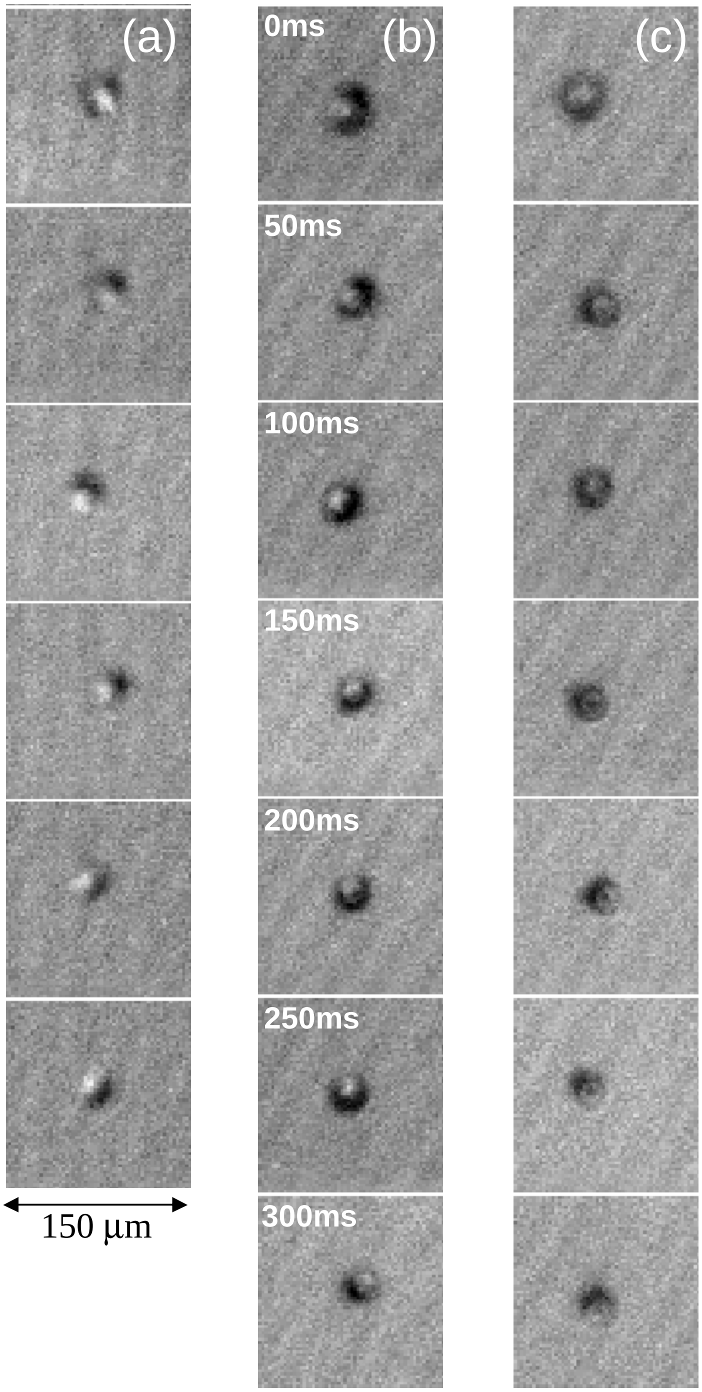

Figure 3.16: Three nondestructive image sequences showing the time evolution of two-component vortices in the (0,1) state. The image frames are spaced by the times indicated. (a) A $|2\rangle$ vortex (dark) with a moderately sized $|1\rangle$ core (bright) is unstable and breaks up. The $|1\rangle$ and $|2\rangle$ components separate into two segments that rotate around one another. (b)&(c) A $|2\rangle$ vortex with a small-sized $|1\rangle$ core is stable. The $|1\rangle$ fluid remains confined in the $|2\rangle$ fluid and tracks the precessional motion of the vortex core.

3.5 Vortex Core precession [51]

3.5.1 Abstract

We have observed and characterized the dynamics of singly quantized vortices in dilute-gas Bose-Einstein condensates. Our condensates are produced in a superposition of two internal states of ^{87}Rb, with one state supporting a vortex and the other filling the vortex core. Subsequently, the state filling the core can be partially or completely removed, reducing the radius of the core by as much as a factor of 13, all the way down to its bare value of the healing length. The corresponding superfluid rotation rates, evaluated at the core radius, vary by a factor of 150, but the precession frequency of the vortex core about the condensate axis changes by only a factor of two.

3.5.2 Introduction

The dynamics of quantized vortices in superfluid helium and superconductors have been fascinating and important research areas in low-temperature physics [155, 74, 154]. Even at zero temperature, vortex motion within a superfluid is intricately related to the quantization of current around the vortex core. Besides these superfluid systems, studies of the dynamics of optical vortices has also become an active area of research [87, 112]. More recently, demonstrations of the creation of quantized vortices in dilute-gas Bose-Einstein condensates (BEC) [122, 118] have emphasized the similarities between the condensed matter, optical, and dilute-gas quantum systems. Because of the observational capabilities and the techniques available to manipulate the quantum wavefunction of the condensates, dilute-gas BEC experiments provide a unique approach to studies of quantized vortices and their dynamics. This section reports direct observations and measurements of singly quantized vortex core precession in a BEC.

Numerous theoretical papers have explored the expected stability and behavior of vortices in BEC [105, 141, 6, 55, 106, 82, 152, 153, 116, 147, 123, 90, 135]. One interesting expected effect is vortex core precession about the condensate axis [141, 55, 106, 82, 152, 153, 116, 147, 123]. Radial motion of the core within the condensate can also occur, and may be understood as being due to energy dissipation and damping processes. Core precession may be described in terms of a Magnus effect – a familiar concept in fluid dynamics and superfluidity [155, 74]. An applied force on a rotating cylinder in a fluid leads to cylinder drift (due to pressure imbalances at the cylinder surface) that is orthogonal to the force. Analogously, a net force on a vortex core in a superfluid results in core motion perpendicular to both the vortex quantization axis and the force. In the condensate vortex case, these forces can be due to density gradients within the condensate, for example, or the drag due to thermal atoms. The density-gradient force may be thought of as one component of an effective buoyancy: just as a bubble in a fluid feels a force anti-parallel to the local pressure gradient, a vortex core in a condensate will feel a force towards lower condensate densities. The total effective buoyancy, however, is due less to displaced mass (the "bubble") than it is to dynamical effects of the velocity-field asymmetry, a consequence of a radially offset core. Typically, the total buoyancy force is away from the condensate center, and the net effect is an azimuthal precession of the core via the Magnus effect. Drag due to the motionless (on average) thermal atoms opposes core precession, causing the core to spiral outwards towards the condensate surface. In the absence of this drag (for temperature ~ 0), radial drift of the core may be negligible.

3.5.3 Experimental technique

Our techniques for creating and imaging a vortex in a coupled two-component condensate are described in refs. [122, 159]. The two components are the $|F=1, m_F=-1\rangle$ and $|F=2, m_F=1\rangle$ internal ground states of ^{87}Rb, henceforth labeled as states $|1\rangle$ and $|2\rangle$ respectively. We start with a condensate of 10^6 $|2\rangle$ atoms, confined in a spherical potential with oscillator frequency 7.8 Hz. A near-resonant microwave field causes some of the $|2\rangle$ atoms to convert to $|1\rangle$ atoms. The presence of a rotating, off-resonant laser beam spatially modulates the amplitude and phase of the conversion. The net result is a conversion of about half of the sample into an annular ring of $|1\rangle$ atoms with a continuous quantum phase winding from 0 to 2π about the circumference – a singly quantized vortex. The balance of the sample remains in the non-rotating $|2\rangle$ state and fills the vortex core. With resonant light pressure we can selectively remove as much of the core material as we desire. In the limit of complete removal, we are left with a single-component, bare vortex state.

In this bare-core limit, the core radius is on the order of the condensate healing length $\xi = (8\pi n_0 a)^{-1/2}$, where n_0 is the peak condensate density and a is the scattering length. For our conditions, $\xi = 0.65\ \mu$m, well under our imaging resolution limit. The bare core can be observed after ballistic expansion [118] of the condensate, but this is a destructive measurement. On the other hand, if we leave some of the $|2\rangle$-state atoms filling the core, the pressure of the filling material opens up the radius of the $|1\rangle$ vortex core to the point where we can resolve the core in a time series of nondestructive phase-contrast images.

3.5.4 Filled-core dynamics

We first discuss vortex dynamics in two-component condensates, where $10\%-50\%$ of the atoms were in the $|2\rangle$ fluid filling the $|1\rangle$ vortex core. We took successive images of the $|1\rangle$ atoms in the magnetic trap, with up to 10 images of each vortex. The vortex core is visible as a dark spot in a bright $|1\rangle$ distribution, as shown in Fig. 3.17(a). Instabilities in our vortex creation process usually resulted in the creation of off-center vortex cores, allowing us to observe precession of the cores. We observed precession out to ~ 2 s, after which the $|2\rangle$ fluid had decayed to the point that the vortex core was too small to be observed in the trapped condensate.

The recorded profile of each trapped condensate was fit with a smooth Thomas-

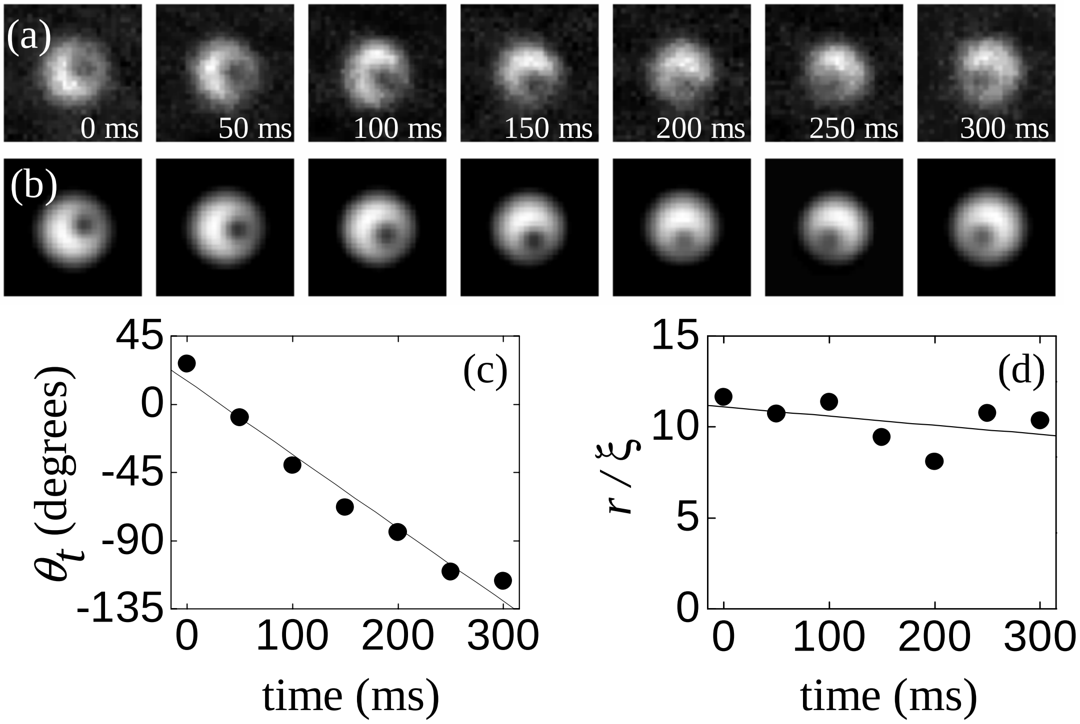

Figure 3.17: (a) Seven successive images of a condensate with a vortex and (b) their corresponding fits. The 75-μm-square nondestructive images were taken at the times listed, referenced to the first image. The vortex core is visible as the dark region within the bright condensate image. (c) The azimuthal angle of the core is determined for each image, and is plotted vs. time held in the trap. A linear fit to the data indicates a precession frequency of 1.3(1) Hz for this data set. (d) Core radius r in units of healing length ξ. The line shown is a linear fit to the data.

Fermi distribution. Each vortex core profile was fit with a Gaussian distribution to determine its radius and position within the condensate. From the fits, we determined the overall radius R_t of the trapped condensate (typically 22 μm), the HWHM radius r of the filled vortex core, and the displacement d_t and angle θ_t of the core center with respect to the condensate center. Core angles and radii for the images in Fig. 3.17(a) are shown in Figs. 3.17(c) and (d). The vortex core is seen precessing in a clockwise direction, which is the same direction as the vortex fluid flow around the core. The angular precession frequency was determined from the time dependence of θ_t (Fig. 3.17(c)). This and other similar data sets showed no reproducible radial motion of the core over the times and parameters examined. However, consistent decrease in the size of the core was observed, which we interpret as being due to known decay of the $|2\rangle$ fluid through inelastic atomic collisional processes.

For each data set, we determined a mean core radius and displacement. The data cover a range of core radii ($r = 7\xi$ to 13ξ), displacements ($d_t = 0.17R_t$ to $0.48R_t$), and percentage of atoms in the core (10% to 50%). Except for a few “rogue vortices” (discussed below), the measured precession frequencies are clustered around 1.4 Hz, as shown in Fig. 3.18, precessing in the same direction as the fluid rotation. The data (Fig. 3.18(a)) suggest a slight increase in frequency for cores further from the condensate center. We also see (Fig. 3.18(b)) a slight decrease in precession frequency for larger cores. These measurements are in qualitative agreement with two-dimensional numerical simulations for two-component condensates [123].

As indicated in Fig. 3.18, a few vortex cores exhibited precession opposite to that of the fluid flow (negative frequencies). The quality of the corresponding vortex images was routinely lower than for the positive-frequency precession points, with vortices looking more like crescents and “D” shaped objects rather than like the images of Fig. 3.17. We only found such occurances with our two-component (in-trap) measurements. We speculate that this “inverse precession” may be due to rare events in

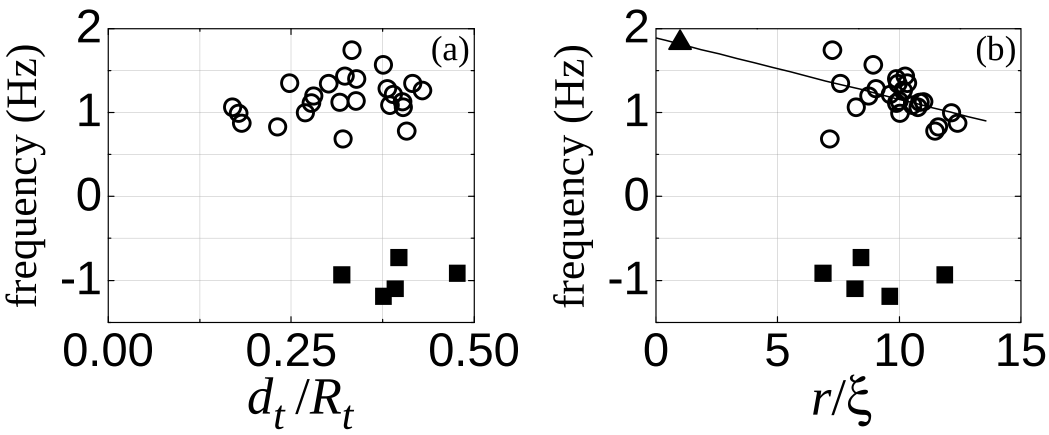

Figure 3.18: Compiled data for filled vortex core precession, with each data point extracted from a series (as in Fig. 3.17) of nondestructive images of a single vortex. Precession frequency is plotted vs. (a) core displacement d_t in units of condensate radius R_t, and (b) core radius r in units of healing length ξ. Circles correspond to positive frequencies and filled squares to negative frequencies. (Positive frequency is defined as core precession having the same handedness as the vortex angular momentum.) The triangle at $r = \xi$ shows for reference the average measured precession frequency of many bare vortices (see text and Fig. 3.19(b)). A line is drawn as a guide to the trend in frequency vs. core size.

which total angular momentum may be distributed in a complicated way among both internal states. Such cases might arise due to position instabilities of the rotating laser beam during the vortex creation process. Recent theoretical attention has addressed the possibly related situation of non-symmetric configurations of vortices in two-component condensates [90, 135].

3.5.5 Bare core dynamics

To examine the dynamics of bare vortices, our procedure consisted of taking a nondestructive phase-contrast picture of the partially filled $|1\rangle$ vortex distribution (Fig. 3.19(a) inset), as previously discussed, followed by complete removal of the core filling [7]. We then held the bare vortex in the trap for a variable hold time t_h, after which the condensate was released from the trap. We took a final near-resonance phase-contrast image [8] of the atomic distribution (Fig. 3.19(a)) after the condensate had ballistically expanded by a factor of ~ 3.5 [9] and the empty core had expanded [70] to a fit radius of $\sim 9\mu$m.

Displacements d_t and angular positions θ_t of the cores for the in-trap images were extracted as described before. The images of the expanded clouds were fit with identical distributions, and the Thomas-Fermi radius R_e of the expanded cloud and the vortex core displacement d_e and angle θ_e were obtained for each image. For each pair of images, we determined the angular difference $\Delta\theta_{et} \equiv \theta_e - \theta_t$ between the cores in the expanded and in-trap images. We also determined the core displacement ratio d_e/d_t, an indicator of the radial motion of the core during the hold time t_h.

From the measurements of $\Delta\theta_{et}$ at different hold times t_h (Fig. 3.19(b)), we find a bare core precession frequency of 1.8(1) Hz, slightly faster than the precession of filled cores and consistent with the trend shown in Fig. 3.18(b) for filled cores. To emphasize that our measurements of filled and empty cores are different limits in a continuum of filling material, we indicate the measured bare core precession frequency in Fig. 3.18(b)

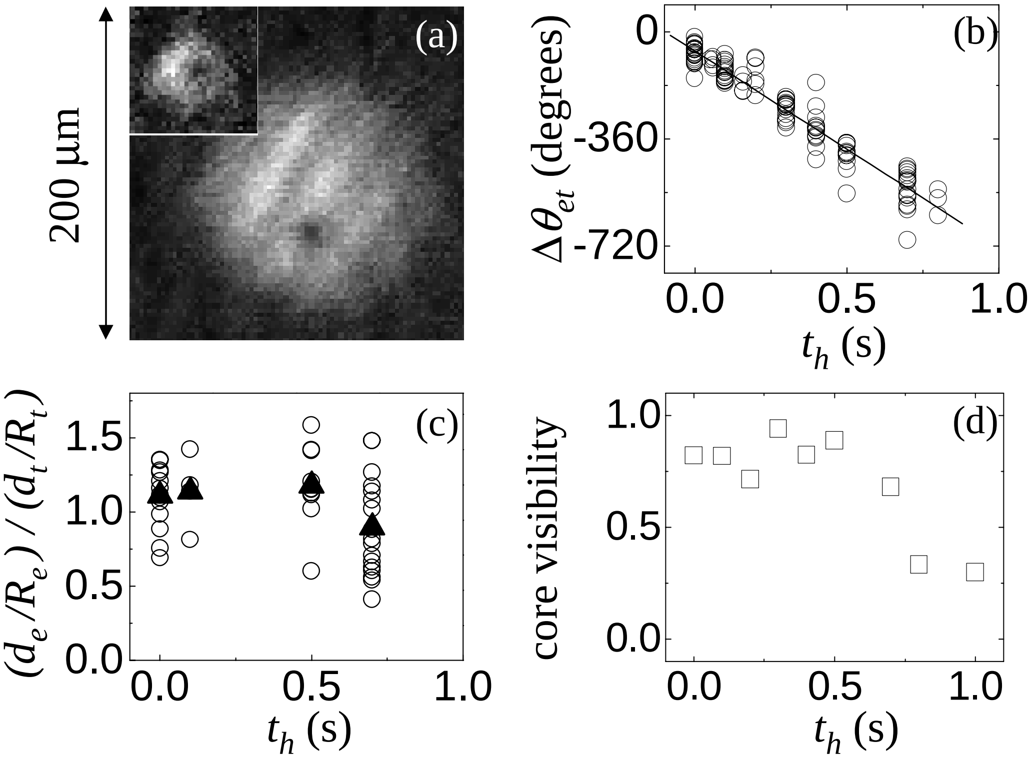

Figure 3.19: (a) Ballistic expansion image of a vortex after all $|2\rangle$ atoms have been removed. The dark spot is the bare vortex core. Inset – the corresponding, preceding in-trap nondestructive image of the partially-filled core. (b) Angular differences $\Delta\theta_{et}$ between vortex cores from the in-trap and expansion images, plotted against hold time t_h in the magnetic trap. The line is a fit through the data, indicating a bare core precession frequency of 1.8(1) Hz. (c) Radial core motion is determined by $(d_e/R_e)/(d_t/R_t)$, the ratio of the fractional core displacements from the expansion and in-trap images of each data set. The data are shown as open circles, with the average of all data at each given hold time plotted as a filled triangle. (d) Core visibility of an expanded vortex, defined as the conditional probability for observing a vortex in an expanded image given the observation of a vortex in the corresponding, pre-expansion in-trap image. Visibility drops dramatically for hold times $t_h > 1$ s.

with a point at $r = \xi$.

From Fig. 3.18(b) it is apparent that the structure and content of the vortex core have a relatively modest effect on precession frequency. One can calculate, for instance, the fluid rotation rate ν_r at the inner core radius. The value of ν_r is given by the quantized azimuthal superfluid velocity evaluated at the radius of the core, divided by the circumferential length at that radius. For bare vortices, ν_r is about 260 Hz, while for the largest filled cores of Fig. 3.18(b) (for which nearly half of the sample mass is composed of core filling), ν_r is only about 1.7 Hz. Thus between vortices whose inner-radius fluid rotation rates vary by a factor of 150, we see only a factor of 2 difference in precession frequency.

The slower precession of filled cores can be understood in terms of our buoyancy picture. Due to its slightly smaller scattering length, $|2\rangle$ fluid has negative buoyancy with respect to $|1\rangle$ fluid, and consequently tends to sink inward towards the center of the condensate [10]. With increasing amounts of $|2\rangle$ material in the core, the inward force on the core begins to counteract the outward buoyancy of the vortex velocity field, resulting in a reduced precession velocity. It is predicted that with a filling material of sufficiently negative buoyancy in the core, the core precession may stop or even precess in a direction opposite to the direction of the fluid flow [123], but our data do not reach this regime.

Various theoretical techniques involving two- and three-dimensional numerical and analytical analyses have been explored to calculate the precession frequency of a vortex core within a condensate. We briefly compare those most readily applied to our physical parameters, assuming a spherical, single-component condensate with 3×10^5 atoms in a non-rotating trap. Where relevant, we assume a core displacement of $d_t = 0.35 R_t$. A two-dimensional hydrodynamic image vortex analysis [11] has been analytically explored in the homogeneous gas [82] and two-dimensional harmonic confinement [116] limits. The latter of these predicts a bare core precession frequency of ~ 0.8 Hz. Svidzinsky and Fetter's three-dimensional [152] solution to the Gross-Pitaevskii equation predicts a precession frequency of ~ 1.3 Hz. Jackson *et. al.* [106] have obtained results in close agreement with this analytical solution using a numerical solution to the Gross-Pitaevskii equation. Finally, a path-integrals technique by Tempere and Devreese [153] predicts a 1.24-Hz precession, and a two-dimensional simulation by McGee and Holland [123] using a steepest-descents technique predicts a precession frequency of 1.2 Hz.

Measurements of d_e/d_t for different hold times t_h show the radial motion of the bare cores and is a probe of energy dissipation of the vortex states. The plot of Fig. 3.19(c) displays no trend of the core towards the condensate surface during t_h, indicating that thermal damping is negligible on the 1 s timescale [12]. However, we notice a sharply decreasing visibility of expanded bare vortices for hold times greater than $t_h \geq 1$ s, as indicated in Fig. 3.19(d). The absence of radial core motion suggests that decreased visibility is due to imaging limitations rather than true decay. One hypothesis is that the vortex core may be tilting away from the imaging axis [151], suppressing contrast in optical depth below our signal-to-noise threshold. Such a situation may arise if the trap is not perfectly spherical, and if the vortex is not aligned along a principle axis of the trap. Evidence in support of this hypothesis [13] will be presented in Section 3.6.

Through a combination of destructive and nondestructive imaging techniques we have obtained measurements of vortex dynamics in bare- and filled-core vortices in dilute-gas BEC. Vortex precession frequencies show only modest dependence on the radius and content of the vortex core. Further measurements of vortex dynamics in condensates may reveal the rate of loss of angular momentum at finite temperatures, an indication of energy dissipation. Such measurements may suggest interpretations for "persistence of current" in condensates, further strengthening ties between BEC and superfluidity. In order to pursue these goals, we plan to extend the studies reported here to investigate higher-order dynamical behavior and to characterize the dissipative effects of finite temperatures.

3.6 Vortex tilting [98]

3.6.1 Abstract

A vortex in a condensate in a nonspherical trapping potential will in general experience a torque. The torque will induce tilting of the direction of the vortex axis. We observe this behavior experimentally and show that by applying small distortions to the trapping potential, we can control the tilting behaviour. By suppressing vortex tilt, we have been able to hold the vortex axis along the line of sight for up to 15 seconds. Alternatively, we can induce a 180° tilt, effectively reversing the charge on the vortex as observed in the lab frame. We characterize the vortex non-destructively with a surface-wave spectroscopic technique.

3.6.2 Introduction

The decay of “persistent” supercurrents, be they in superfluids or superconductors, is intimately connected to the dynamical behavior of vortices. A magnetically trapped, gas-phase Bose-Einstein condensate (BEC) provides a useful laboratory for characterizing the microscopic behavior of individual vortices subject to various controlled perturbations [122, 118, 51, 61]. In one recent experiment, a vortex core in a near-spherical condensate “vanished” [51] from view apparently without moving out to the edge of the sample and annihilating there. Another group [118] found that the empirical critical rotation velocity for the formation of a vortex in an elongated condensate is much higher than can be accounted for by a simple model of the vortex as a rigid line-defect without any dynamics along its length. Feder *et al.* [80] explain the latter observation by showing that the higher rotation rate is necessary to suppress the growth of anomalous normal modes ("bending" modes) of the vortex. In this section we study the lowest odd-order normal mode, which in our near-spherical geometry corresponds not to a bend but to a tilting of the vortex orientation. We show that the "vanishing" vortex of ref. [51] was in fact due to tilting of the vortex away from the line of sight. Such uncontrolled tilting was caused by residual asphericity in the condensate's confining potential. By tailoring the asphericity, we have learned to control the tilting dynamics.

The tilting behaviour of a vortex in a condensate, confined in a slightly aspheric, parabolic potential, is discussed in detail by Svidzinsky and Fetter [151], starting from the Gross-Pitaevskii equation. Only a brief summary of their theoretical results is given here. The vortex direction satisfies a set of equations similar in form to the Euler equations for rigid body rotation, familiar from classical mechanics. As a result, the tilting dynamics of a quantized vortex in a confined BEC are reminiscent of the behaviour of a freely spinning rigid body as seen in the body-fixed frame [84]. In the case of the spinning rigid body, there are two stable axes about which precession of the spin direction will occur, namely the axes with the largest and smallest moments of inertia. The intermediate axis is unstable and no precession occurs about that direction. If the spin direction lies initially near the intermediate axis, it will evolve away from its initial orientation. Similarly, for a quantized vortex in a BEC, tilt precession of the vortex is predicted to occur about two stable axes, given in this case by the tight and weak directions of confinement. The unstable axis corresponds to the direction of intermediate trapping strength.

The tilting dynamics of a vortex are constrained by two integrals of motion, one in particular corresponding to conservation of energy. Physically, this implies that, as the vortex tilts, its direction follows an angular trajectory which is a contour of constant vortex length, or equivalently constant energy. As is the case for all the normal modes of a vortex, the precession frequency for a vortex tilting about a stable axis is predicted to scale with the rate of vortex fluid circulation evaluated at the condensate edge. For our typical conditions, this fluid rotation is near 0.3 Hz. The theoretical frequency for tilt precession depends additionally on the magnitude and character of the trap asymmetries and the initial orientation of the vortex.

3.6.3 Vortex formation

In our experiment, we first use a wavefunction engineering technique to make singly quantized vortices in a two-component BEC [122, 159]. The two components, which are two different hyperfine levels of ^{87}Rb, are magnetically confined together in a nominally spherical, harmonic TOP trap [78], parameterized by a trapping frequency $\omega_{trap}/2\pi = 7.8(1)$ Hz. The vortex formation process leaves one component in the circulating state while the other component, which is non-rotating, fills out the core [14]. The vortex is formed initially aligned along the line of sight. We take a non-destructive picture of the two-component vortex to record the initial displacement of the core with respect to the center of the condensate cloud. We then create a bare vortex by selectively removing the fluid filling the core [51], which shrinks down to a size below our imaging resolution.

This section deals exclusively with the dynamics of bare vortices in a single-component BEC. The bare vortex state is formed with about $2 \cdot 10^5$ atoms at a temperature of $T/T_c = 0.8(1)$ where the critical temperature T_c is 20(6) nK. The number of atoms in the condensate is determined (in the Thomas-Fermi limit) from the condensate radius R, equal to 20.8(4) μm on average. Following the creation process and core removal, the condensate is held for a variable holding time in its confining potential, and then probed for the presence of the vortex.

3.6.4 Disappearing vortices

We have previously reported that the visibility of vortex cores was lost after a holding time of about 1 s in a nominally spherical trap [51]. In those experiments, the confining potential was suddenly removed, and the condensate allowed to expand ballistically before imaging. The presence of a vortex was detected in the expansion image as a dimple in the condensate's density distribution. The topological nature of a quantized vortex means that the only way for a BEC to rid itself of a vortex is for the core to make its way to the edge of the cloud and annihilate there; the vortex cannot gradually spin down. Our vortices, however, seemed to disappear without any visible radial motion of the cores outward. We did notice that the contrast of the cores as observed in expansion decreased at longer holding times before being lost altogether. These results could be explained by a tilting of the vortex away from the line of sight. Because the vortex core is such a narrow feature, only small deviations from the line of sight ($\sim 20^\circ$) are necessary for contrast to be lost below the noise threshold in the expansion images.

In order to circumvent this imaging limitation, we have implemented an alternative method of vortex detection that is more robust against tilting of the vortex from the line of sight, and that has the additional advantage of being sensitive to the handedness of the vortex circulation. This detection technique uses the idea that the collective excitation frequencies of a trapped condensate are sensitive to the presence of a vortex [15, 150]. We make use of quadrupolar surface-wave excitations, that is, surface-wave excitations which carry angular momentum $l = 2$. (The angular momentum of these perturbative excitations should not be confused with the angular momentum per particle of the bulk of the condensate, which in the presence of a well-centered vortex approaches $l = 1$). The projection of angular momentum of an $l = 2$ surface-wave excitation onto the axis of the vortex direction can have components $m = 0, \pm 1, \pm 2$.

In the absence of a vortex, the counter-propagating $\pm m$ modes are degenerate, but in the presence of a vortex the handedness of the fluid flow breaks time-reversal symmetry and lifts the degeneracy. The use of surface-wave spectroscopy for vortex detection was first demonstrated experimentally by Chevy *et al.* [61].

To detect a vortex, we excite an $l = 2$, $m_z = 0$ excitation about the vertical $\hat{z}$ axis by modulating the trapping potential for a single cycle. Along the line of sight, the $\hat{x}$ axis, the $m_z = 0$ mode projects onto a superposition of $m_x = +2$, $m_x = -2$, and $m_x = 0$ modes. The $m_x = +2$ and $m_x = -2$ superposition may be thought of as a standing-wave of clockwise and counterclockwise surface waves. Along the line of sight we observe the cloud alternately stretch along two principal axes, first vertical, then horizontal. The excitation period is measured to be 11.0(2) Hz in agreement with the predicted value $\sqrt{2}\omega_{trap}$ [148]. The presence of a vortex along the line of sight induces a splitting of the clockwise and counterclockwise wave velocities, so that the nodes of the standing-wave are not completely fixed. As a result we observe a precession of the principal axes of the quadrupolar excitation. We record the precession in a sequence of seven non-destructive images, strobed at half the quadrupolar excitation period. A typical data set is shown in Fig. 3.20. Opposite vortex circulation clearly leads to opposite precession of the principal axes, as is evident in Figs. 3.20(b) and (c).

For a vortex whose direction is tilted with respect to the line of sight, we still expect precession of the quadrupolar principal axes to be induced about the vortex direction. The main limitation to vortex detection in this case is that there must be sufficient projection of the quadrupolar precession onto the imaging camera. In the extreme case where the vortex is oriented at 90° to the line of sight, any quadrupolar precession will also be about an axis perpendicular to the line of sight, in other words, not readily observable on the imaging camera.

Armed with our new detection method, we revisited the topic of longevity of vortices in our nominally spherical trap. The precession of surface waves clearly revealed

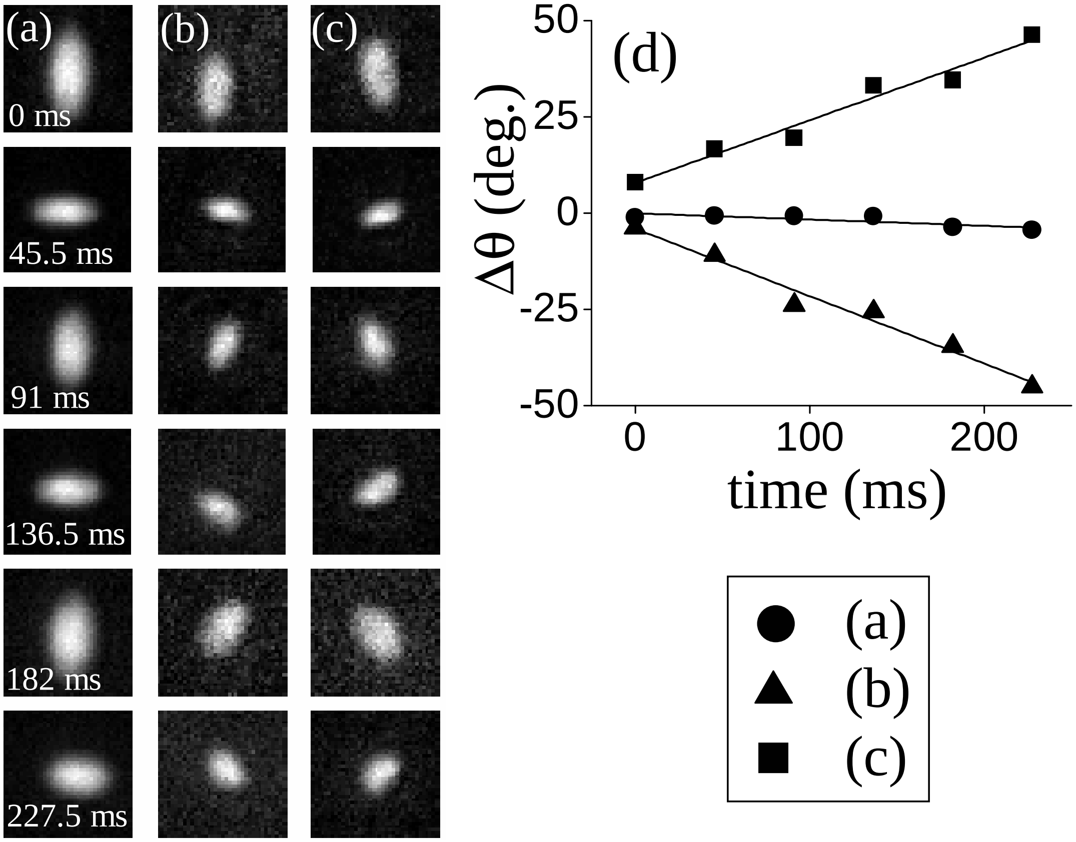

Figure 3.20: Using surface excitations for *in situ* detection of a vortex in a confined BEC. (a), (b) and (c) are each a series of non-destructive images of the quadrupolar mode, after excitation. The pictures are strobed at 45.5 ms, half the excitation period. (a) is the case of a vortex free condensate; (b) and (c) show the excitations in the presence of a vortex whose core is normal to the plane of the page. The vortices in (b) and (c) have opposite handedness. The principal axes of the ellipse-shaped quadrupolar mode precess in the direction of the fluid flow. The images are each fit to an elliptical distribution with orientation $\Delta\theta$ of the principal axes. The orientation, expressed as an angular deviation from the vertical and horizontal axes, is plotted versus time in (d) for each of the cases (a), (b) and (c). A linear fit has been applied to the data to determine a precession frequency of the principal axes, -0.49(4) Hz for (b) and 0.45(5) Hz for (c).

the presence of vortices at 1.5 s and at 2 s holding time, well after the vortices ceased to be visible in the expansion images [51]. Given that the surface-wave probe for vortices should be relatively robust to small tilts of the vortices with respect to the line of sight, we came to the tentative conclusion that our vortices were in fact tilting away from the line of sight during the first few seconds after their creation. This behavior could be accounted for by small ($\leq$3%) residual asymmetries in our trapping potential.

3.6.5 Vortex tilt: three experiments

Further study of the tilting required better characterization of the trap potential, and we achieved this by deliberately introducing tailored deformations to the confining potential, deformations that were certain to overwhelm the residual asymmetry. The results of three such experiments are presented here: first, the suppression of vortex tilt; second, the generation and observation of vortex tilt about a stable axis; and, third, the manipulation of a vortex's orientation through controlled deformations of the BEC's confining potential.

In the first experiment, the spherical confining potential is squeezed by 10% along the line of sight following the creation of a vortex in the BEC [16, 17]. This places the vortex along the tight, stable axis of the trap. As a result, tilting of the vortex away from the line of sight should be suppressed. After a variable holding time in the squeezed trap, the confining potential is returned to spherical symmetry and the condensate is then quickly probed for the presence of the vortex. Using both the surface-wave and expansion techniques, we have detected vortices lasting for holding times up to 15 s. This is a significant improvement over our previously published limit of 1 s. Although visibility has been restored at long times by holding the condensates in a squeezed trap, it is important to note that only well-centered vortices have been found to survive to the longest times. This is consistent with a model of initially offset cores spiraling out of the condensate under the influence of thermal damping [18].

The second experiment proceeds in the same way as the first except the spherical trap is now squeezed along a horizontal axis at 45° to the line of sight. The squeezing process produces a triaxial confining potential, where the tight and weak directions of confinement lie in the horizontal plane while the intermediate axis is vertical. The measured trap asymmetries together with the initial vortex direction indicate that the vortex should precess about the weak axis, although slightly different conditions could lead to rather different behavior (see Fig. 3.21). In any case, as the vortex tilts away from the line of sight to a maximum excursion of 90° from the imaging axis, the visibility of the vortex will gradually disappear. Eventually, if the vortex precesses about the stable axis and back into the line of sight, it should become visible again in a 'revival of visibility'. This effect is seen in Fig. 3.22, where vortex visibility is plotted as a function of holding time in the squeezed trap. Visibility is defined as the probability of detecting a vortex at a given time and is obtained from a set of approximately ten shots for each point plotted. Vortices whose initial offset from trap center exceeds a prescribed value of $\sim$0.15 R are omitted from the analysis. This is done to reduce blurring of the revival due to possible position-dependent tilt rates, and, moreover, to prevent loss of contrast at long times due to the drift of cores out of the condensate. The vortex detection is accomplished with both surface-wave and expansion techniques. The revival measured with expansion imaging is much more narrowly resolved in time, as is to be expected from this method's greater sensitivity to alignment of a vortex with the line of sight.

The frequency of the tilt mode, determined from the data in Fig. 3.22, is 0.25(2) Hz. The theory of Svidzinsky and Fetter [151] predicts the lowest-order odd-parity vortex mode should have a frequency below 0.3 Hz for our values of the Thomas-Fermi radius, confinement asymmetry, and initial vortex angle. Uncertainties in the confinement asymmetry preclude a more precise determination of the theoretical tilting frequency. The uncertainties are such that the vortex could lie on an initial trajectory arbitrarily close to a 'saddle' line, where the revival time should diverge (see Fig. 3.21). The high

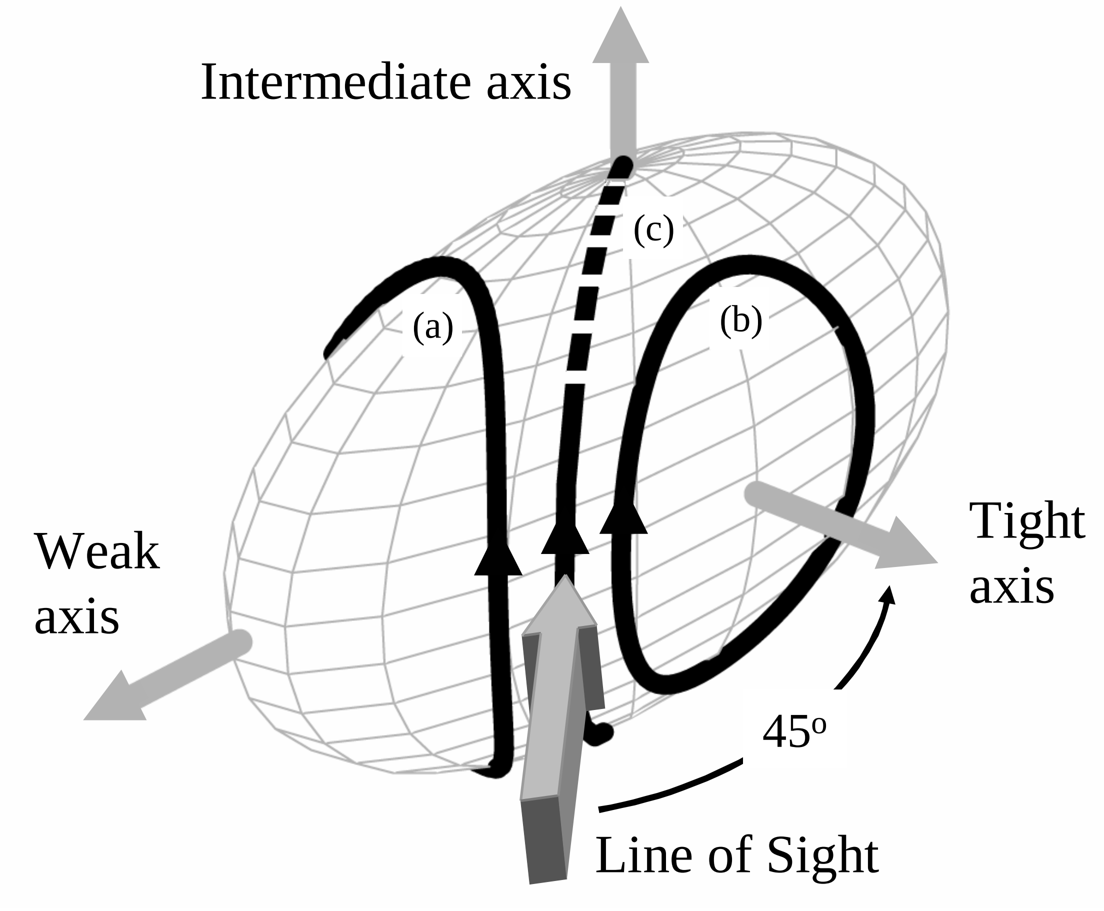

Figure 3.21: Possible tilting behaviour of a vortex in a confined BEC is illustrated for the conditions of the second tilting experiment (see text). The axes of symmetry for the triaxial confining potential are indicated. Initially, the vortex is nearly anti-aligned with the line of sight. Depending on the precise initial orientation of the vortex and the relative values of the confinement strengths, the vortex direction could (a) precess about the weak axis, (b) precess about the tight axis, or (c) drift towards the intermediate axis along a 'saddle' line, as traced out on the surface of the condensate.

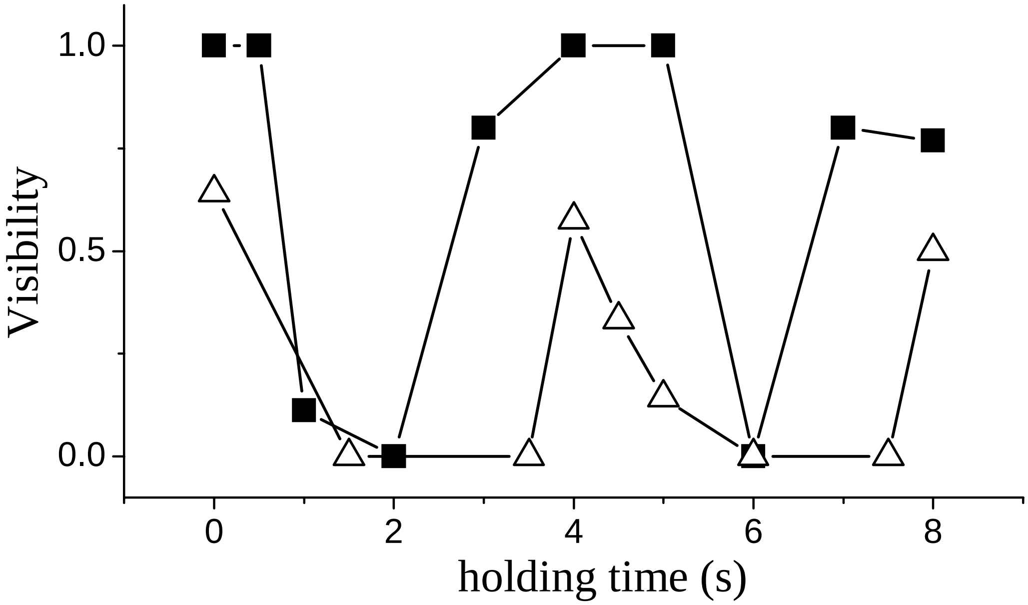

Figure 3.22: Visibility of a vortex in a BEC is plotted versus the time the BEC is held in a trap squeezed along an axis at 45° to the line of sight. Visibility is the probability of detecting a vortex over several shots. Filled squares indicate vortex detection with the surface-wave technique; open triangles indicate detection with the expansion technique.

contrast of the two revivals in Fig. 3.22 clearly indicates, however, that the shot-to-shot fluctuations of the confinement asymmetry and of the initial position of the vortex are small.

The third and final tilting experiment demonstrates the reversal of vortex handedness. The vortex, as usual, is formed along the line of sight. The direction of the vortex is then flipped 180° by deforming the trapping potential in two steps, as illustrated in Fig. 3.23. From the perspective of the line of sight, the 'lab frame,' the vortex has effectively flipped its handedness. Surface-wave detection is used to verify this, with pictures similar to Figs. 3.20(b) and (c) being obtained before and after the flipping process respectively. Manipulation of vortex direction may prove to be a useful technique in a TOP trap. For example, maneuvering a vortex to an arbitrary direction followed by a second stage of wavefunction engineering could produce a condensate wavefunction with more complicated, three-dimensional topological structure.

In conclusion, we have described a non-destructive method of vortex detection and used it to characterize the tilt modes of a bare vortex in a trapped BEC. Control over the tilt of a vortex has been demonstrated, including the suppression of tilting altogether. The suppression of tilting, which maintains the visibility of vortices out to long times, now permits the study of the lifetime of vortices at finite temperature.

3.7 A position sensitive spectroscopy

The vortex dynamics described to this point have been essentially at zero temperature and well described by the Gross-Pitaevskii equation. The finite temperature behaviour which has been alluded to in Sections 3.5 and 3.6 is the lifetime or "persistence" of a bare vortex in the condensate. As a topological feature, the vortex cannot "spin down." To leave the condensate, it must spiral radially outward under the influence of the friction imparted by the normal cloud bathing the condensate (see also Section 4.6). In order to assess this motion one would like to follow the radial position

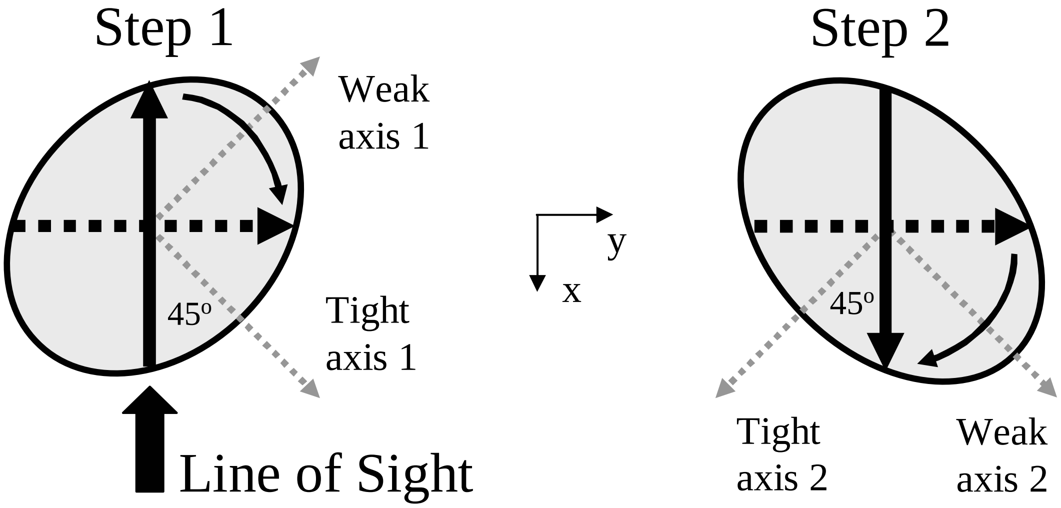

Figure 3.23: A sequence of trap deformations to reverse the direction of a vortex is shown. The figure shows a horizontal crosssection of the BEC as seen from above. The vortex is initially formed along the line of sight and aligned with the -$\hat{x}$ axis. In step 1, the trap is squeezed in the horizontal plane along tight axis 1. The vortex is then allowed to precess for 1.5 s, at which point it should be aligned with the $\hat{y}$ axis. The new direction of the vortex is indicated by a dotted arrow. In step 2, the trap is squeezed along tight axis 2 and the vortex allowed to precess another 1.5 s until it is aligned with the $\hat{x}$ axis. To an observer looking down the line of sight, the vortex has effectively reversed its handedness. Changing the time allowed for vortex precession by 0.5 s inhibited the effect. For the correct timing, the flipping process was found to be successful 80% of the time.

of the vortex as it spirals outward to the condensate edge. However, a complication arises if wavefunction engineering is used to create the vortex. As was mentioned in Section 3.3.3, condensate slosh causes shot-to-shot variations in the initial core position. This is an important consideration in comparing with theory since the lifetime of a vortex is predicted to depend logarithmically on its initial distance from the condensate center (with a centered vortex being metastable) [82]. As a result, a nondestructive measurement scheme is required to determine both the initial and final radial core positions for each experimental run. Such a task is technically challenging for bare vortices since the core size is below imaging resolution in-trap, where nondestructive phase-contrast imaging can be used. The first option available, as outlined in Section 3.5, is to measure the initial core position of a two-component vortex, remove the component that fills out the core to create a bare vortex, wait, then analyze the final core position in expansion. Besides being a relatively convoluted measurement, this technique suffers from limitations to vortex visibility in the expansion images, where the "haze" of a sizable normal cloud surrounding the condensate obscures the vortex cores. Interestingly, the surface-wave spectroscopy presented in the previous section provides an alternative nondestructive technique to assess bare-vortex position in the condensate. Although vortex-lifetime results obtained in this way ultimately proved inconclusive and are not discusssed here, the technique, which is interesting in its own right, is outlined here.

As alluded to previously, surface-wave spectroscopy is sensitive to the angular momentum of a vortex in the condensate. For the quadrupolar ($l = 2$) surface waves used in the experiment, the vortex flow breaks the symmetry between co- and counter-propagating surface modes ($m = +2$ and $m = -2$), which acquire a frequency splitting [15]. A sum-rule argument [161] shows that the splitting depends on the angular momentum per particle $\langle \ell_z \rangle$ in the condensate

$$\omega_+ - \omega_- = \frac{2}{m}\frac{\langle \ell_z \rangle}{\langle r_\perp^2 \rangle}. \tag{3.20}$$

The expectation value of $r_\perp^2$, the square of the co-ordinate perpendicular to the vortex quantization axis, depends on the shape of the potential confining the condensate. For the nominally spherical condensates in the experiment, $\langle r_\perp^2 \rangle$ scales with the square of the size of the condensate given by the Thomas-Fermi radius R. To connect with the results of Section 3.6, the standing-wave pattern formed by a superposition of $m = +2$ and $m = -2$ waves [Figure 3.20] precesses due to the splitting at a rate

$$\omega_p = (\omega_+ - \omega_-)/4. \tag{3.21}$$

While a singly-charged vortex at the *center* of a condensate contributes an angular momentum per particle of $\hbar$, an offset vortex will contribute progressively less as it moves towards the edge of the condensate. (The core of course still has a 2π winding around it.) A calculation for a harmonic confining potential [19] gives the angular momentum per particle in terms of lateral vortex displacement r as

$$\langle \ell_z \rangle = \hbar \left(1 - \frac{r^2}{R^2} \right)^{5/2}. \tag{3.22}$$

Thus, in so far as surface-wave spectroscopy is sensitive to the angular momentum per particle in the condensate, it provides an indirect assay of vortex position. Recent theory [83, 96] indicates that the sum-rule result for the frequency splitting [Eqn. 3.20] may be inaccurate for a single offset vortex; nevertheless, the qualitative behaviour is certainly correct and provides an intuitive understanding of the effect of vortex position on surface-wave spectroscopy.

To verify this experimentally, multiple runs have been performed to create a vortex in the standard way. To summarize briefly, a two-component vortex with varying radial position is engineered and the core fluid is then removed to create a bare vortex. An image of the two-component vortex is taken before the removal and later fit to obtain the vortex position. A standing wave of $m = +2$ and $m = -2$ waves is excited on the condensate containing the bare vortex. The precession rate [Eqn. 3.21] of the standing wave, determined from a series of non-destructive images [Figure 3.20], is plotted as a function of radial core displacement in Figure 3.24. Although the basic trend of the data is as expected, the precession rate decreases faster with displacement than the predicted dependence according to Eqns. 3.20 and 3.22 as well as the prediction according to ref. [83]. This discrepancy is likely due to systematic errors in the core position obtained from fits to the two-component images. Simulated images of two-component vortices indicate that the fits are untrustworthy when the distance from the cloud center to core position is more than a few tens of percent of R.

As a final note, the statement that the surface-wave technique is "nondestructive" does require justification as the presence of the surface-wave excitation has the potential to perturb the vortex. At least in terms of effects to the radial core position, the nondestructiveness can be readily assessed by monitoring any changes in the surface-wave precession frequency over time. As demonstrated qualitatively in Figure 3.25, the surface-wave excitation apparently has no effect on the radial position of the vortex for the range of excitation amplitude used (20%-40%).

3.8 Soliton engineering and decay to vortex rings [50]

3.8.1 Abstract

We have created spatial dark solitons in two-component Bose-Einstein condensates in which the soliton exists in one of the condensate components and the soliton nodal plane is filled with the second component. The filled solitons are stable for hundreds of milliseconds. The filling can be selectively removed, making the soliton more susceptible to dynamical instabilities. For a condensate in a spherically symmetric potential, these instabilities cause the dark soliton to decay into stable vortex rings. We have imaged the resulting vortex rings.

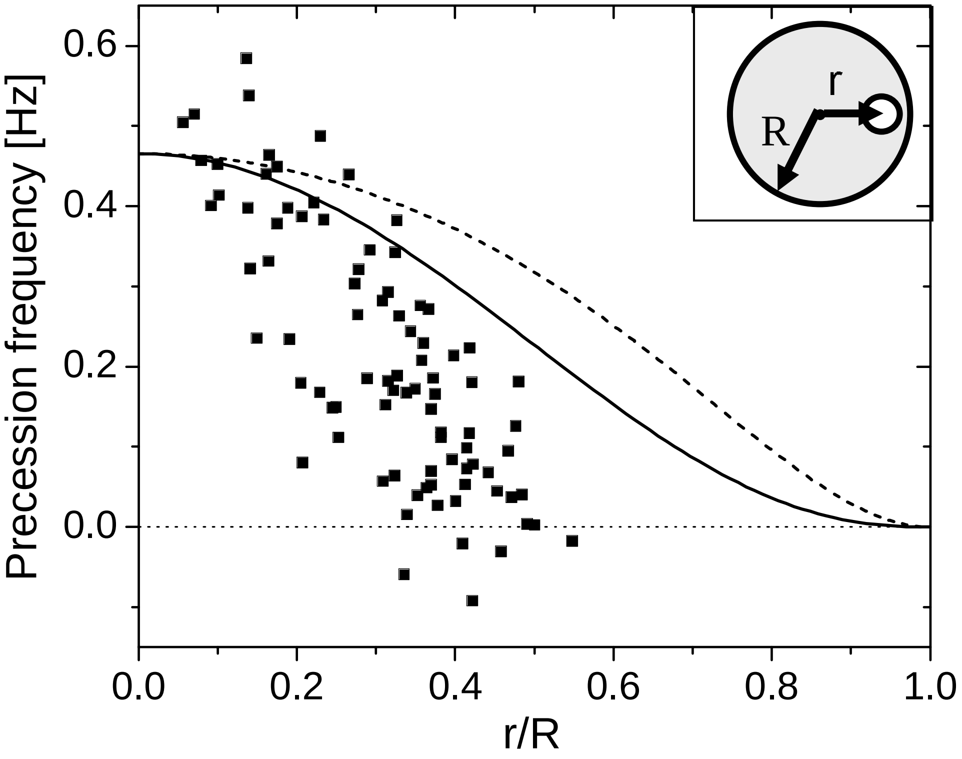

Figure 3.24: Quadrupolar precession frequency vs. displacement r of a bare vortex from the center of a condensate (see inset). The displacement is scaled by the Thomas-Fermi radius ($R \approx 22\mu$m) of the nominally spherical condensate. Each data point represents a single experimental run in which a singly-quantized vortex is created in a condensate, followed by quadrupolar surface-wave spectroscopy as per Figure 3.20. The plot combines three data sets with different amplitudes for the quadrupolar excitation, characterized by an ellipticity ϵ of $\{0.2,\ 0.26,\ 0.4\}$. The solid line is the predicted behaviour based on Eqns 3.20 & 3.22 while the dotted line is the prediction according to ref. [83].

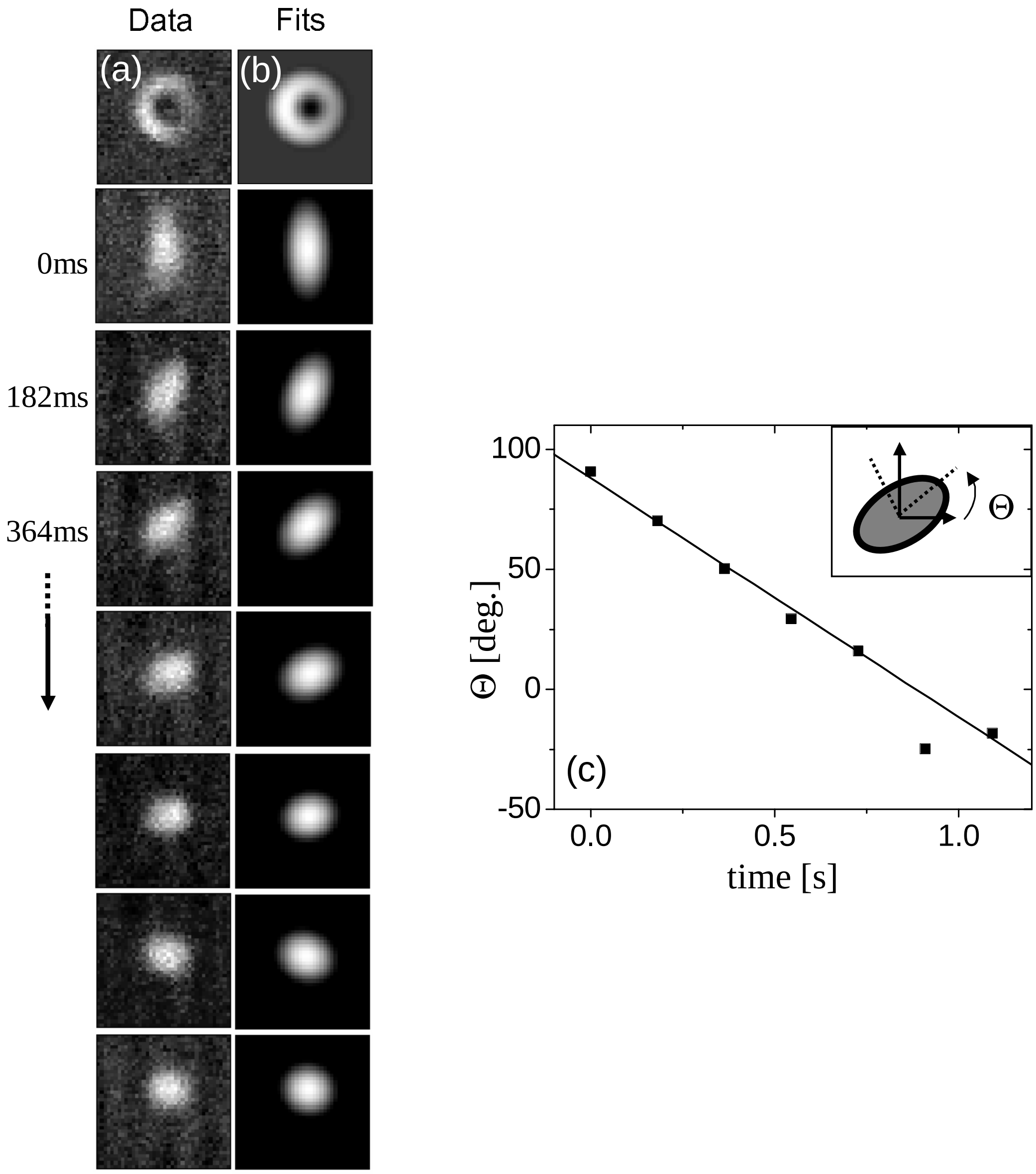

Figure 3.25: Long-time precession of a quadrupolar standing-wave on the surface of a condensate containing an $\ell = 1$ vortex. (a) Sequence of nondestructive *in-situ* images, which begins in the first frame by showing a two-component vortex engineered into the condensate. The fluid filling the core is then removed (not shown) and a quadrupolar surface wave excited. The second frame and following show the time evolution of the surface wave where the indicated times are referenced to the time of surface-wave excitation. The images are spaced by two oscillation periods of the quadrupolar surface mode ($2\tau = 182$ms) such that the major axis of the condensate deformation would remain vertical in the absence of a vortex. The decrease in ellipticity of the cloud is primarily due to thermal damping of the quadrupolar mode. (b) A two-dimensional ellipse is fit to each image. (c) The angular orientation of the ellipse's major axis is extracted and plotted as a function of time. A linear fit has been added to guide the eye.

3.8.2 Introduction

Topological structures such as vortices and vortex rings have fascinated scientists and mathematicians for centuries. In a quantum fluid, vortices have quantized flow around a one-dimensional core where the density vanishes. Vortex **lines**, which terminate at the boundaries of the quantum fluid, have been observed in superfluid helium and superconductors [74, 155], and recently in Bose-Einstein condensates (BECs) [121, 118]. Similarly, vortex **rings** are vortices whose cores are closed loops; the poloidal quantized flow pattern resembles that of a smoke ring. Quantized vortex rings have been produced in superfluid helium, and were first detected in pioneering work by Rayfield and Reif [139]. In this section we report direct experimental observations of vortex rings in BECs.

Solitons are localized disturbances in a continuous nonlinear medium that preserve their spatial profile due to a balance between the effects of dispersion and nonlinearity [20]. Dark solitons have been previously created in single-component BECs using phase-imprinting methods [21]. These structures are characterized by a local decrease in fluid density (the depth). The macroscopic quantum phase of the BEC differs on either side of the soliton; for a completely dark (black) soliton, the depth is 100% (a complete absence of fluid), the phase offset is π, and the soliton velocity is zero. We have created black solitons (having a fluid-free nodal plane) in nearly spherically symmetric ^{87}Rb BECs, and have observed the subsequent decay of the solitons into vortex rings.

Unlike vortices and vortex rings, whose stability is ensured by Kelvin's theorem [74], soliton stability depends on the nonlinearity and geometry of the medium [22]. Optical dark solitons in self-defocusing nonlinear media have been observed to decay into optical vortices via a 'snake instability' [23], confirming predictions [110]. In general, dark solitons in BECs are also expected to be inherently dynamically unstable [111, 24, 60, 81]. Because both the velocity and depth of a soliton are determined by its phase offset [140], small local perturbations of either the strength of the nonlinearity or of the depth give the soliton a corresponding nonuniform transverse velocity profile. Once the soliton begins to decay, it quickly breaks up into more stable structures. Within our spherically symmetric BECs, the expected decay products are concentric vortex rings [81]. Because the theoretical background for soliton decay in condensates has been previously described in detail in Ref. [81], we limit our paper to primarily a phenomenological presentation of data. Evidence for soliton decay is obtained through direct images of the BEC density distribution. We provide a visual comparison of data with numerical simulations of soliton decay.

3.8.3 Experimental techniques

We create dark solitons using concepts that we have previously applied to making singly quantized vortices in BECs [121, 159]. The magnetically trapped BEC can exist as a superposition of two internal components, hyperfine states $|1\rangle \equiv |F=1, m_F=-1\rangle$ and $|2\rangle \equiv |F=2, m_F=1\rangle$. Conversion between the two components is achieved with a microwave field slightly detuned from the $|1\rangle$ to $|2\rangle$ internal conversion energy. A "modulation beam," an off-resonant laser beam whose small spatial focus provides a requisite spatial selectivity, is dithered rapidly across the BEC. The laser beam induces a small AC Stark shift in the $|1\rangle$ to $|2\rangle$ transition energy. The phase and amplitude of this effective frequency modulation varies from point-to-point in the sample in a spatial pattern determined by the time-varying position of the optical modulation beam; thus the microwave-induced inter-component conversion varies in phase and amplitude across the BEC.

In our experiment, we start with a uniform-phase (i.e., ground state) condensate of component $|2\rangle$. To make a soliton, we choose a modulation beam pattern such that inter-component conversion is suppressed in the middle of the sample, whereas the upper and lower parts of the BEC undergo conversion to component $|1\rangle$ with an initial phase offset of π between the two parts [Figure 3.26]. Uncontrolled variations in the timing of the modulation cause the angular orientation of the soliton nodal plane to vary randomly from one soliton to the next. For further details, see our earlier vortex work [121] and theory by Williams and Holland [159]. The soliton state contains about 3×10^5 $|1\rangle$ atoms, and the filling consists of about 7×10^5 $|2\rangle$ atoms. The axial (vertical) trap frequency is 7.6(3) Hz, the radial (horizontal) frequencies are 7.8(3) Hz, and the condensates have a Thomas-Fermi (TF) radius of 28 μm. The solitons are created at temperatures of $T = 23(6)$ nK, or $T/T_c = 0.8(1)$, where T_c is the BEC phase transition temperature.

After removing the coupling field, we observe the trapped excited-state condensates using nondestructive phase-contrast imaging. Our probe laser is tuned such that only component $|1\rangle$ is visible, and these atoms appear bright on a dark background. As described in [121], a filled-core vortex appears as a dark hole in a bright atom cloud. Similarly, a soliton with a filled nodal plane appears as a dark band that divides the $|1\rangle$ BEC. This two-component BEC can be described as a **bright** soliton of component $|2\rangle$ trapped within the $|1\rangle$ dark soliton [25]. The filling material of $|2\rangle$ atoms stabilizes the dark soliton against dynamical instabilities; the filled solitons are observed to last for at least 800 ms.

To study the dynamical instabilities of the solitons, we first use resonant light pressure to selectively remove the $|2\rangle$ atoms that fill the nodal plane. The $|2\rangle$ atoms are adiabatically removed over 100 ms, and a bare dark soliton of component $|1\rangle$ remains. The soliton node and any soliton decay products are then too small to be observed while the BEC is held in the trap [26]. We thus remove the trapping potential and allow the BEC to ballistically expand, causing the variations, or 'defects,' in the density distribution to also expand [70]. These density defects are then resolvable. We obtain a final near-resonance phase-contrast image of the expanded atom cloud, using a probe detuning of 20 MHz. Expansion imaging has previously been used to detect bare vortex

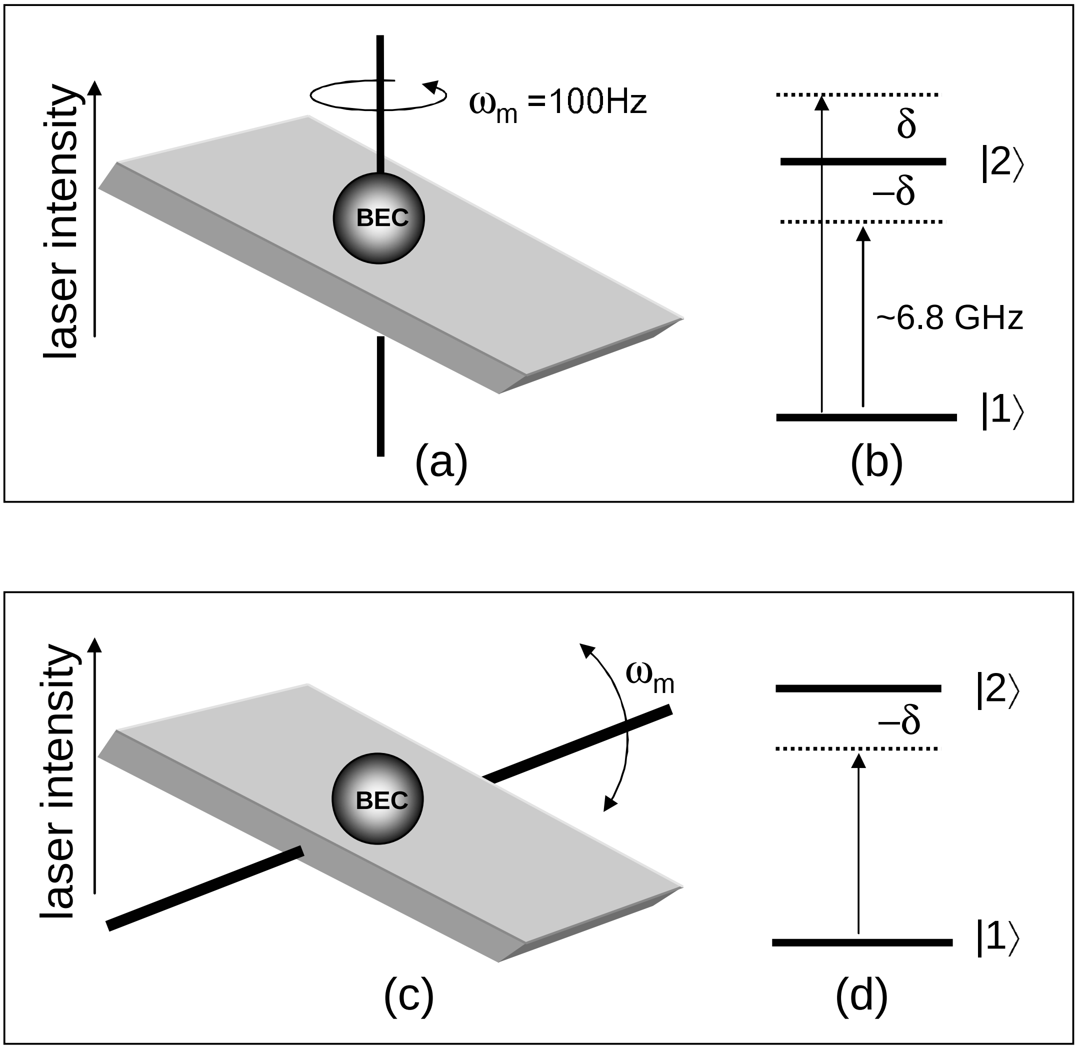

Figure 3.26: Experimental setup for soliton engineering is shown in (a,b). A linear gradient in light intensity (a) from an offset laser beam is rotated about the condensate center at a frequency ω_m. A pair of microwave coupling drives (b) is applied between internal $|1\rangle$ and $|2\rangle$ with detunings of $\delta = \pm\omega_m$. Using the results of Section 3.3, the experimental setup can be shown to be equivalent to the simpler wavefuction engineering technique as described in (c,d). The light intensity undergoes a "see-saw" modulation (c) at frequency ω_m and only one coupling drive (d) is used. The node of the soliton is formed along the pivot of the seesaw, where no intensity modulation occurs and, as a result, no population transfer occurs between states $|1\rangle$ and $|2\rangle$.

cores [118, 51].

3.8.4 Numerical calculations

Before discussing experimental data, we briefly describe results of numerical calculations. The techniques employed have been described in detail in Ref. [81]. The equilibrium configuration, dynamics, and Bogoliubov excitation spectrum for a two-component condensate at low temperatures may all be obtained from the appropriate three-dimensional time-dependent Gross-Pitaevskii (GP) equation [137], with $N_1 = 3 \times 10^5$ $|1\rangle$ atoms in a state initially constrained to have odd parity along one axis, and $0 \leq N_2 \leq 7 \times 10^5$ $|2\rangle$ atoms in an even-parity state. The spherical trap frequency is chosen to be $\nu_0 = 7.8$ Hz, and the intra- and inter-species scattering lengths are $(a_{11}\,, a_{22}\,, a_{12}) = 5.5 \times (1.03\,, 0.97\,, 1.0)$ nm, respectively [99]. The behavior of the BEC in full two-component simulations, in which we approximate a slow removal of the $|2\rangle$ atoms, is found to be qualitatively similar to simulations where we set $N_2 = 0$ at the outset. In all cases, the soliton is found to undergo a snake instability, decaying into vortex rings.

Indeed, the Bogoliubov spectrum contains modes with complex frequencies for all N_2 considered; such modes have been shown to drive the soliton instability [81]. For $N_2 \geq 4 \times 10^5$, only one such mode remains, with imaginary frequency of magnitude $\nu \sim (4 \times 10^4/N_2)\nu_0$. Assuming a soliton decay time $\propto \nu^{-1}$, a filled soliton with $N_2 = 7 \times 10^5$ is expected to be stable for longer than 2 s, consistent with experimental observations.

The results of a one-component ($N_2 = 0$) simulation are shown in Fig. 3.27. The soliton decays into three nearly concentric vortex rings approximately 130 ms after initial formation. In general, the rings tend to migrate towards the condensate surface, and may then grow, shrink, and reconnect with each other. The innermost ring is the most stable, remaining intact for at least 150 ms in the absence of a collision with another ring. Along an imaging axis parallel to the plane of a given vortex ring, the integrated column density reveals two dips in the density distribution, connected by a fainter line. The ring, however, is not constrained to lie in any given plane, and may bend and tilt, producing other types of images. In elongated traps with aspect ratios of two or higher, simulations indicate that a soliton can decay directly into nearly parallel vortex lines rather than rings; however, this behavior is not obtained for spherical traps.

3.8.5 Experimental results

In our experimental cycle, we first create a filled dark soliton and obtain a non-destructive image of the initial trapped (filled) soliton. Over the next 100 ms, we remove the $|2\rangle$ atoms from the soliton nodal plane until only the $|1\rangle$ atoms remain. The trapped single-component condensate is then held for a variable hold time before being allowed to ballistically expand for 56 ms [27]. Finally, the expanded density distribution is recorded.

Images of the decayed solitons typically reveal two dips in the condensate density distribution, as shown in Fig. 3.28(b)-(e). While our images are consistent with the expected signatures of vortex rings, they are inconclusive evidence for the decay of solitons into vortex rings; from a single image containing only a pair of density dips, we can not differentiate between a **single vortex ring** and a **pair of vortex lines**. For comparison, an expanded vortex line is shown in Fig. 3.28(a). We believe that our signal-to-noise levels may limit our ability to see a dark line connecting the two clear density defects that would indicate the sides of a ring. We also note that high-frequency excitations visible in $T = 0$ simulations would be quickly damped for $T > 0$, and thus not seen in the experiment.

Because detection of two-dimensional topological structures, such as dark solitons and vortex rings, can be enhanced by probing along two orthogonal directions, we added an additional probe beam. In our improved apparatus, the second probe beam is orthogonal to the original beam, and propagates horizontally (as does the original).

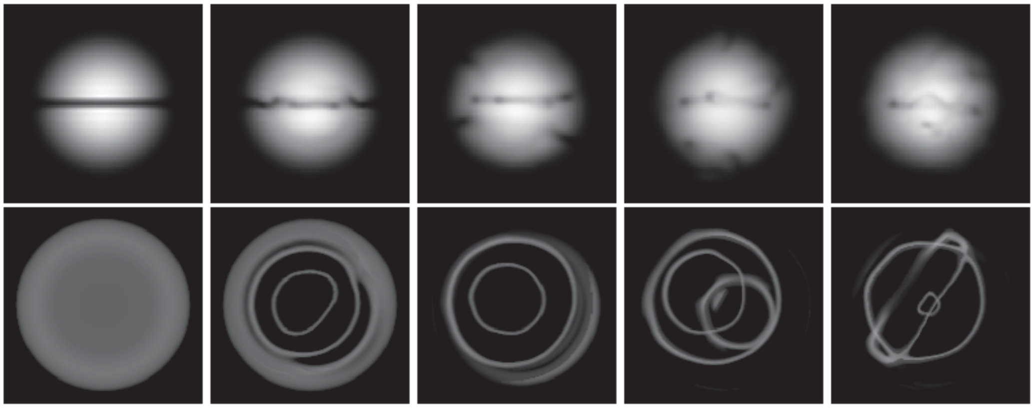

Figure 3.27: Results of numerical simulations showing the decay of a black soliton in a BEC. The simulation corresponds to 3×10^5 ^{87}Rb atoms in a spherically symmetric trap with frequency 7.8 Hz. Successive frames are shown at 50 ms intervals, with the first frame at 100 ms after the start of the simulation. The first row shows the density profile of the condensate, integrated down an axis parallel to the soliton plane. The low-density regions within the cloud are also rendered (second row), with views perpendicular to the soliton plane.

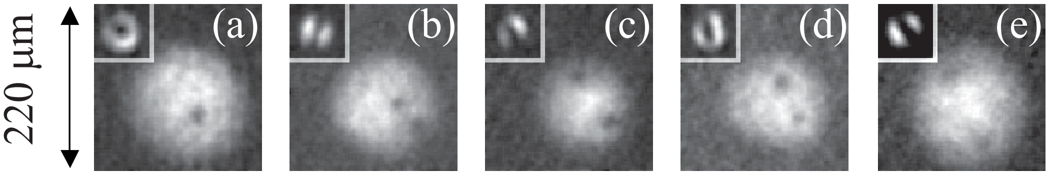

Figure 3.28: Typical images of expanded condensates, and their initial states (insets) before the $|2\rangle$ atoms were removed. (a) A vortex, (b)-(e) the decay products of solitons. Image (e) was taken with a hold time of 500 ms; all other images were taken with a hold time of 0 ms, in addition to the 100 ms $|2\rangle$ removal and the 56 ms expansion [22].

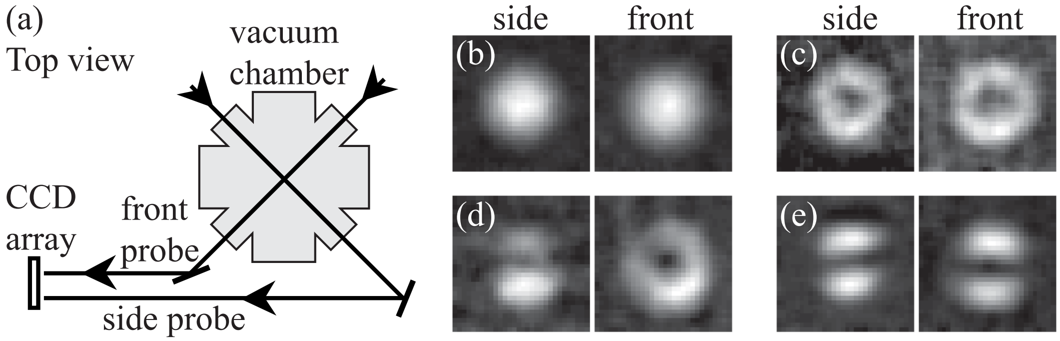

Figure 3.29: (a) An illustration of our probe beam paths. (b)-(e) Simultaneous 100-μm-square images of trapped condensates from the front and side imaging directions. Shown are (b) a ground state condensate of component $|1\rangle$, (c) a shell of $|1\rangle$ atoms around a central ball of $|2\rangle$ atoms [21,22], (d) a $|1\rangle$ vortex filled with $|2\rangle$ atoms, and (e) a horizontally oriented dark soliton of component $|1\rangle$, filled with $|2\rangle$ atoms.

The beams intersect at the condensate. Phase-contrast imaging is used independently with each beam path, and the probe beams propagate towards different sides of a single charge-coupled device (CCD) camera array. The apparatus allows us to take simultaneous pictures of condensates from the 'front' (original) and the 'side' (added) directions using a single camera, as illustrated in Fig. 3.29(a). While we can observe the full depth of the filled soliton node along the front direction, regardless of the initial orientation, the nodal plane is usually at an oblique angle to the side probe, and soliton contrast is thus reduced. Examples of simultaneous images of trapped condensates from the front and side are shown in Figs. 3.29(b)-(e). In the pair of images shown in Fig. 3.29(d), the filled core of a vortex is visible as the dark hole in the front image, and as the dark band in the side image. In Fig. 3.29(e), a filled horizontal dark soliton appears as a band across the condensate in each probing direction, demonstrating that the BEC is split into two sections.

The use of two orthogonal probe beams confirms that dark solitons indeed decay into vortex rings. With the two beam paths, we observed pairs of density dips in simultaneous side and front expanded images of decayed solitons. In each image set shown in Figs. 3.30(b)-(d), pairs of density dips lie nearly horizontally and at corresponding locations within the two BEC images. We have also obtained images in which a faint line corresponding to a decrease in integrated column density can be observed between two defects in one of the expanded images, as shown in Figs. 3.30(e) and (f), providing further striking demonstrations of soliton decay into vortex rings. Figures 3.30(e)-(g) emphasize that when the vortex ring is not close to horizontal, clear pairs of density dips are not seen in the side images. However, a weak ring-shaped halo may be discerned in the side image residuals of Figs. 3.30(e) and (g), when the ring is in a near-vertical plane orthogonal to the side probe direction. Although the halo signal is only slightly above the noise of the residuals, it can be noticed when compared to the residuals for an expanded ground state condensate, shown in Fig. 3.30(a). Images in Figs. 3.30(b) through (f) represent the best 10% of our data showing solitons decaying into rings; Fig. 3.30(g) is typical.

Numerical as well as experimental data show great variability in the types of images that can be expected after a soliton decays. For example, Fig. 3.30(h) is a rare example showing two clear density dips in the side image, but here a clear line corresponding to the defect extends through the entire condensate in the front image and residuals. It is possible that this image shows soliton decay into two vortex lines rather than a ring, or breakup of a ring into vortex lines. We defer to a future paper a discussion of the diversity of our images, which may result from interesting vortex ring dynamics, including vortex ring bending, tilting, and reconnections.

Small perturbations unavoidably induce a dark soliton to decay. In a spherically symmetric BEC, a soliton decays into a relatively stable vortex ring. In addition to demonstrating this nonlinear decay, our experiment shows that condensates can indeed support vortex rings, which may be detected via expansion imaging. Future experiments may include studies of vortex ring stability, lifetime, and dynamics [108], as well as investigations into vortex structures created by impurity motion above a superfluid

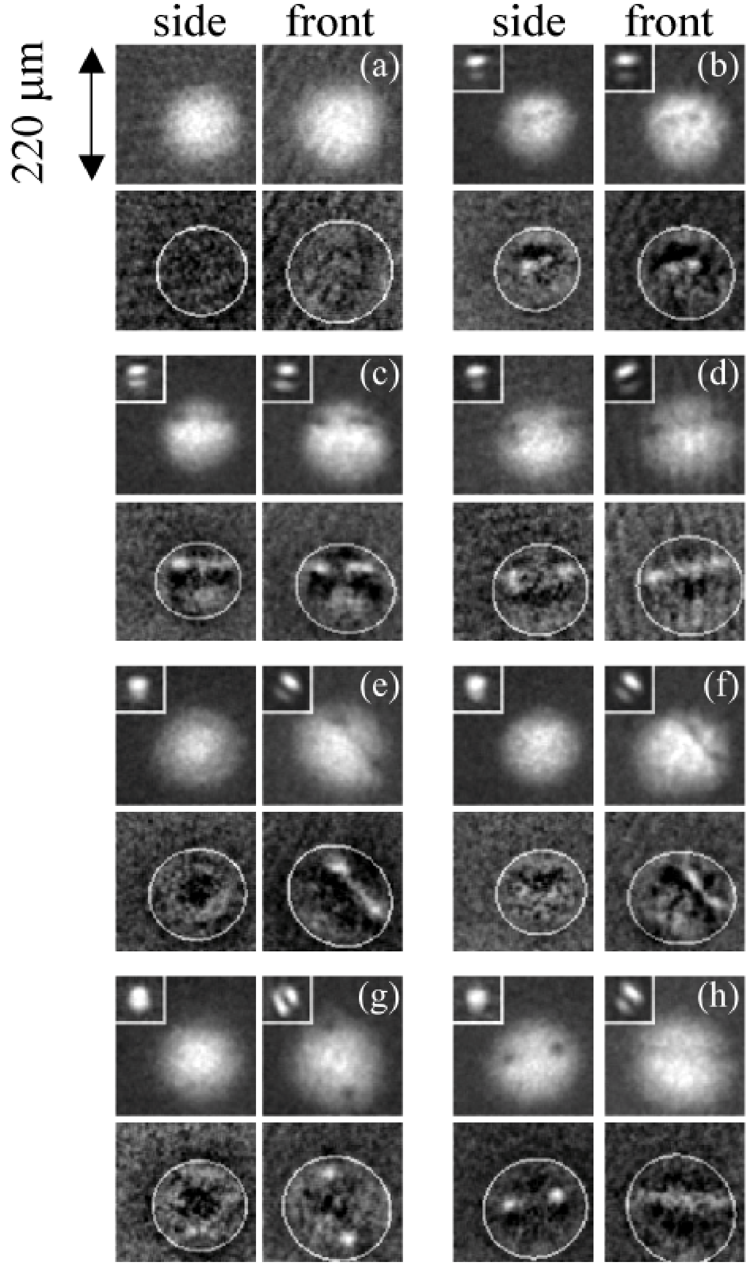

Figure 3.30: Images of expanded condensates and their initial states (insets), as viewed along both imaging axes. Each subfigure consists of two expansion images (top row of each subfigure) and two images of residuals plots (bottom row), obtained after subtracting a TF fit of each expansion image. The white regions in the residuals correspond to depletion of fluid in the BEC. The residuals are superimposed with white ellipses outlining the fit TF profiles of the condensates, for position reference. (a) An expanded ground state condensate. (b)-(h) The decay products of solitons. The hold times (between $|2\rangle$-atom removal and BEC expansion) were 0 ms for images (a)-(c),(f), and (g); 50 ms for (d) and (e); and 150 ms for (h). For all images, we reduced background noise (fringes) using a digital fourier-transform filter.

critical velocity [130]. Possibilities to create vortex rings by other means may also be explored, such as by passing objects through the BEC [107].

3.9 Wavefunction engineering at DC

The wavefunction engineering technique with two-component condensates uses a space- and time-dependent modulation of the resonance between the two internal components. In this way, arbitrary control over the population transfer between the states is realized [Section 3.3]. It is, however, possible to exert some degree of spatial control over the population transfer through the application of *static* gradients in the resonance across the condensate. This method of wavefunction engineering "at dc," which is an extension of earlier work in this group on two-component condensates [121], provides an extremely simple way to generate dark solitons in a condensate and may be extended to generate stacks of several solitons.

The method takes advantage of preexisting features of the ^{87}Rb two-photon transition used in the experiment [Figure 3.2] as well the magnetic potential confining the condensate. In particular, the two-photon transition between the simultaneously trapped states $|F=1, m_F=-1\rangle$ ("$|1\rangle$") and $|F=2, m_F=1\rangle$ ("$|2\rangle$") occurs via a magnetically untrapped state, $|F=2, m_F=0\rangle$. As a result, there arises a gradient in the transition's intermediate state detuning Δ_{int} across the vertical extent of the condensate [Figure 3.31]. Essentially this gradient is due to the force of gravity, which the magnetic trapping force counterbalances for the trapped $|1\rangle$ and $|2\rangle$ states but cannot for the intermediate state because of its vanishing magnetic moment.

The gradient in intermediate state detuning has the peculiar effect that it does not change the two-photon resonance frequency across the condensate but instead adds a vertical gradient to the on-resonant coupling strength (Rabi frequency Ω_0)[Eqn. 3.2]. In keeping with the local Bloch picture developed in Section 3.3, a "pseudospin" can be associated with the internal two-level system $\{|1\rangle,|2\rangle\}$ at each vertical point in the

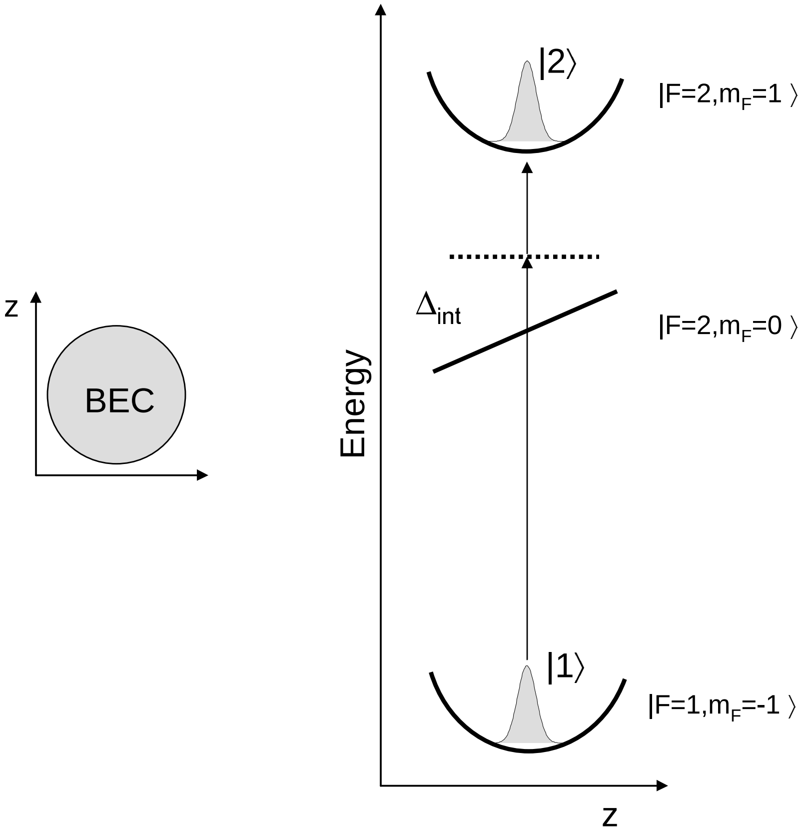

Figure 3.31: Vertical variation in two-photon intermediate state detuning Δ_{int} across a magnetically trapped condensate. The magnetically untrapped intermediate state feels a linear potential gradient (force) due to gravity.

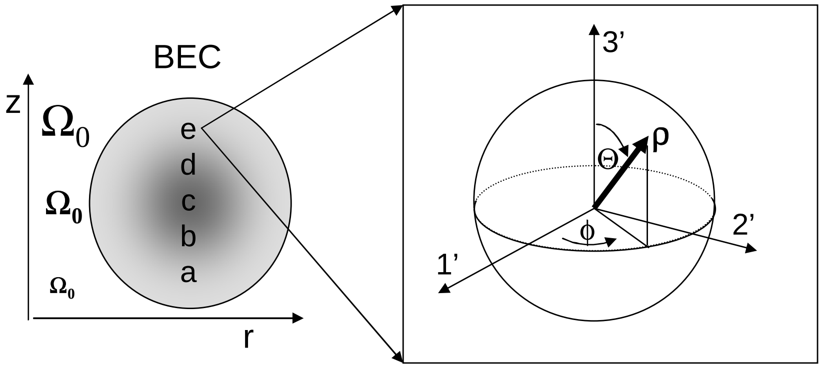

Figure 3.32: Local pseudospin $\vec{\rho}$ (inset) at each vertical point labeled "a...e" on the condensate. The on-resonant Rabi frequency Ω_0 increases vertically, as indicated schematically.

condensate [Figure 3.32]. The pseudospin's polar angle θ characterizes the population difference between $|2\rangle$ and $|1\rangle$ while the azimuthal angle ϕ defines their relative phase. At $t = 0$ before any coupling drive is applied, the condensate is in a single internal state such that the pseudospin points down (for $|1\rangle$) or up (for $|2\rangle$) everywhere on the condensate [Figure 3.33(i)]. The application of an on-resonant coupling drive to the condensate is equivalent to introducing a torque vector along the $\hat{1}$-axis of the Bloch sphere. This causes the pseudospin to precess in the 2-3 plane about the torque direction, corresponding to on-resonant Rabi oscillations. Because of the gradient in Ω_0, the size of the torque changes for different vertical positions across the condensate and the precession of the pseudospin progresses at different rates locally.

After some time, the Rabi oscillation at the top of the condensate will be 2π out of phase with the oscillation at the bottom. This corresponds to a full 2π spread in the pseudospin's orientation across the condensate - one "winding" [Figure 3.33(iii)]. At this time in the condensate, a central region of one spin component vertically separates two outer regions of the other, forming a "hamburger-and-bun" appearance [Figures 3.33(iv) and 3.34]. From the Bloch sphere, it is clear that there must also a vertical step of π in the relative phase ϕ across the middle of the condensate (Compare points b & d in

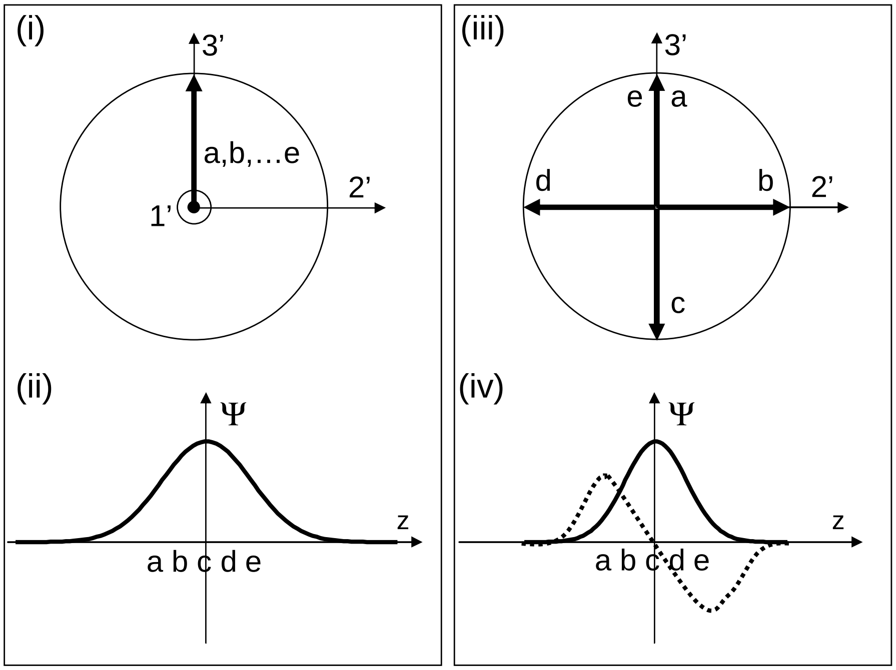

Figure 3.33: Filled dark soliton creation from a static vertical gradient in the Rabi frequency. (i) The condensate begins in one internal state ($|2\rangle$) such that the local pseudospin points up at all vertical positions on the condensate labeled a through e. (ii) The initial condensate wavefunction Ψ is sketched as a function of vertical trap co-ordinate z. (iii) Eventually the vertical gradient in Rabi frequency leads to a complete angular spread in the pseudospin across the condensate. (iv) The corresponding wavefunction is shown for each of the two-components, $|1\rangle$ (dotted line) and $|2\rangle$ (solid line).

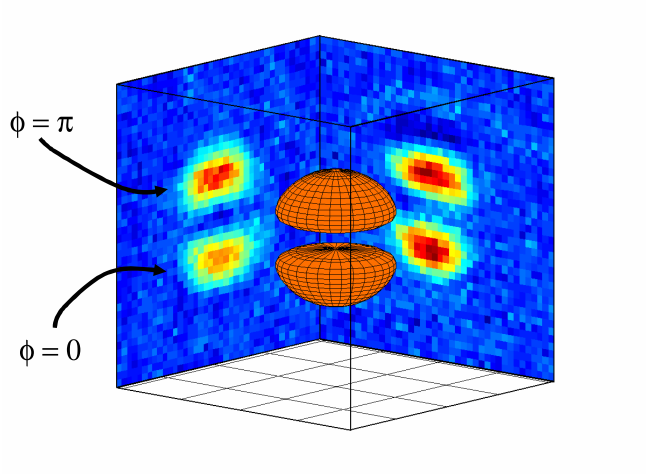

Figure 3.34: Three-dimensional density distribution of a filled dark soliton, inferred from two orthogonal images shown in side panel projections. Only the bimodal distribution of the spin component containing the soliton is displayed. The other component fills out the intervening space forming the horizontal soliton plane.

figure 3.33(iii)). This phase step is wholly associated with the spin component lying in the outer regions since its density node permits the rapid phase change at the center of the condensate. Very simply then, what has been created is a horizontally-oriented filled dark soliton as for Section 3.8! To confirm this indirectly, the central component filling out the soliton plane has been removed to induce the decay of the soliton to vortex rings. After ballistic expansion of the condensate, two axes of images have been used to identify the usual signature of a vortex ring [Figure 3.35], which shows up in *every* shot. The reproducibility is due to the fact that the soliton (and consequently the vortex ring) is always formed in a plane including the two imaging axes.

This soliton creation technique has a few additional features of potential interest. First, if the drive is applied until two or more windings are present in the condensate, a stack of solitons may be created [Figure 3.36]. Unfortunately, corresponding stacks of vortex rings were not observed in expansion. Second, if the coupling drive is not exactly resonant, the phase steps will be smoothed out somewhat and be reduced from π, in other words creating filled gray solitons. Stacks of gray (moving) solitons suggest the possibility of their collisions; however, since each member in the stack has a phase step

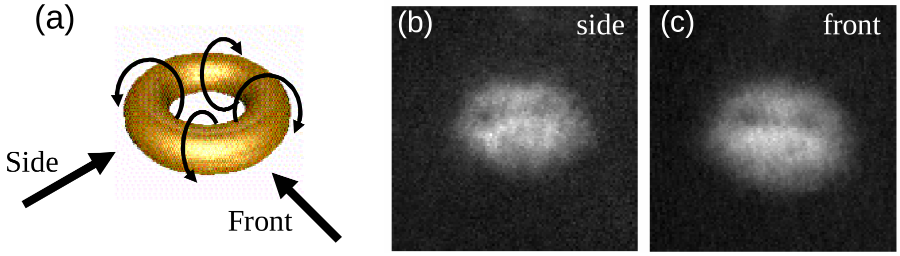

Figure 3.35: Typical vortex ring formed from a "winding soliton." (a) The vortex ring is in a plane including the two orthogonal imaging axes, labeled "front" and "side." (b & c) Expansion images showing the characteristic pairs of density dimples in both imaging axes. The dimples correspond to the points on the vortex ring tangent to the imaging direction.

with the same orientation, the gray solitons will all move in the same direction probably precluding any collisions.

As a final note of general interest, soliton creation through winding demonstrates the quantum weirdness of a spin-1/2 (SU(2)) system. At the time of a single winding in the condensate, the Rabi oscillations at the top and bottom edges of the condensate are 2π out of phase, which for a classical oscillation would indicate rephasing. Both regions *are* in the same spin state yet a π phase difference still exists between them, creating the soliton. Only after a full 4π phase evolution has occurred will the local spin-1/2 systems at the top and bottom of the condensate be rephased.

3.10 More angular momentum

The wavefunction engineering implemented so far with frequency modulation has used the first sideband for coherent control [Section 3.3]. What do the higher-order sidebands offer? For the n^{th} sideband, the phase of the engineered wavefunction is an n-fold multiple of the modulation phase, as has been shown explicitly for the cases $n = 1$ and $n = 2$ [Eqn. 3.15]. This has an interesting consequence in the creation of quantized vortices where a modulation pattern with a 2π azimuthal phase gradient is applied to the condensate. As has been demonstrated in Section 3.3.3, the first sideband can be

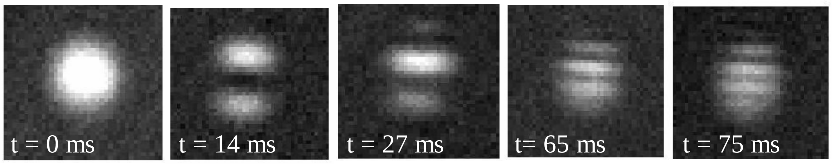

Figure 3.36: Vertical stacks of solitons arising from a static vertical gradient in the Rabi frequency. Successively larger number of solitons are obtained by applying the coupling drive for a longer time t as indicated.

used to transfer the 2π phase winding from the modulation pattern onto the condensate phase to form a singly quantized vortex. Tuning instead to the n^{th} sideband should transfer an *n-fold* winding of 2π, in other words an $\ell = n$ vortex! A simulation of the second sideband case ($\omega_m = \Omega/2$) is shown in Figure 3.37.

In practice, wavefunction engineering via the second sideband has proven to be unsuccessful because the coupling is strongly reduced compared with the first sideband [Eqn. 3.15]. More complicated modulation patterns might make it possible to create multiply quantized vortices using only the first sideband. Instead, a third method has been attempted to create an $\ell = 2$ vortex. A multi-step engineering process is performed in which two $\ell = 1$ windings are sequentially engineered into the condensate [Figure 3.38]. An $\ell = 2$ vortex is expected to be unstable against decay to two $\ell = 1$ vortices, which is a lower energy configuration [129]. Indeed, two $\ell = 1$ vortices are observed in expansion following the engineering process [Figure 3.38(c)]. Unfortunately, it is more likely that motion of the condensate in the intervening time between engineering stages has led to the direct creation of a pair of offset $\ell = 1$ vortex cores rather than a single $\ell = 2$ state. Recently, vortices with charge $\ell = 2$ have been created in a condensate using a different technique that is nevertheless a form of coherent control [28].

The process of adding more vorticity to a condensate through sequential stages of wavefunction engineering is limited to two iterations because of the 50% transfer

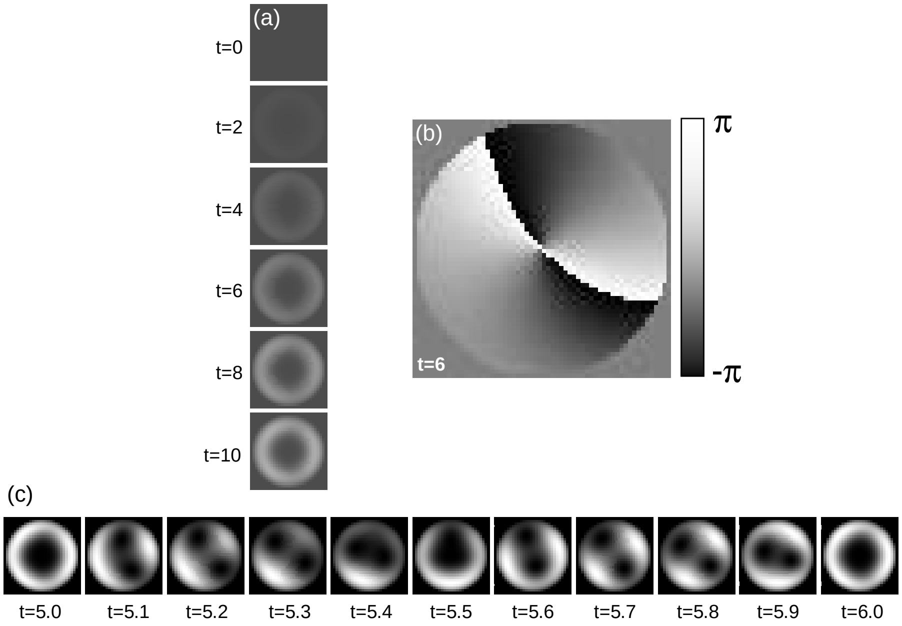

Figure 3.37: Simulation of $\ell = 2$ vortex engineering using the second modulation sideband to control the transfer of population from state $|2\rangle$ to $|1\rangle$. (a) Growth of the vortex population forming a ring of $|1\rangle$ fluid at the condensate perimeter. Time is indicated in units of the average effective Rabi frequency Ω. (b) Relative phase at t=6 between $|2\rangle$ and $|1\rangle$, which may be interpreted as the phase of $|1\rangle$ relative to the flat phase reference of the initial state $|2\rangle$. (c) Transfer dynamics within one Rabi cycle ($2\pi/\Omega$), showing two $\ell = 1$ cores separating, rotating around one another, and re-merging.

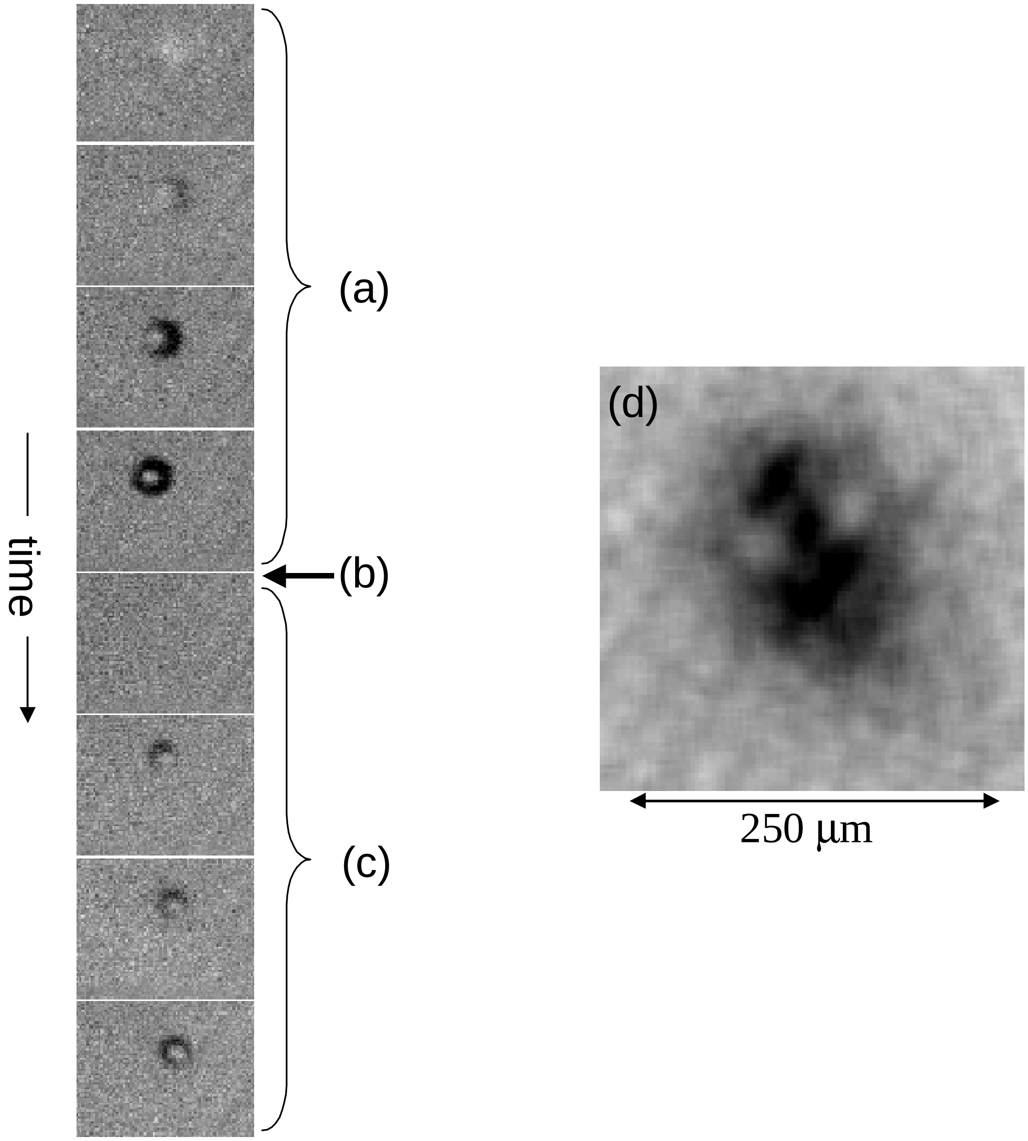

Figure 3.38: Multiple vorticity ($\ell = 2 \times 1$) with multi-step wavefunction engineering. (a) Four sequential nondestructive images show a $|2\rangle$ vortex being engineered into a non-rotating trapped condensate. (b) The $|1\rangle$ fluid filling the vortex core is selectively removed and the remaining $|2\rangle$ vortex transferred into the $|1\rangle$ state with a fast coupling pulse (not shown). (c) A second stage of wavefunction engineering, using the $|1\rangle$ vortex as an initial state, adds another 2π winding to the condensate. (d) An image of the ballistically expanded condensate shows two vortex cores, verifying the creation of a condensate with two units of circulation.

efficiency at each stage. In the next chapter a new approach is taken to introduce large amounts of angular momentum into a condensate in the form of many singly-quantized vortices.

Chapter 4

Vortex Lattices

4.1 From quantum to classical ... and on to quantum

Chapter 3 focused on the creation and behaviour of one quantum of circulation - in other words singly quantized vortices - in a condensate. This chapter deals with the opposite limit of highly rotating condensates containing large amounts of vorticity. The experimental technique has been honed to the point where condensates with large numbers of both atoms and vortices can be made relatively reproducibly. The approach to creating vortex-full condensates is different from that taken in other experimental groups and involves the evaporative cooling of a rotating cold gas to quantum degeneracy. In this way a condensate is created in equilibrium with the rotating environment of the normal gas surrounding it. At high rotation rates, large, well-ordered triangular lattices of vortices are observed in the condensate. In the limit of large amounts of vorticity, the correspondence principle would suggest that the velocity flow in the condensate should mimic classical rigid-body rotation. This of course applies only on a macroscopic scale coarse-grained over the vortex core structure [Figure 4.1]. Classical-like rotational effects, such as centrifugal distortion of the condensate's density, are explored experimentally in this chapter. With direct detection of the vortex cores available, it has also been possible to study the "microscopic" structure of the vortex arrangements, both at equilibrium and under dynamical conditions where applied stress can distort the equilibrium lattice configuration.

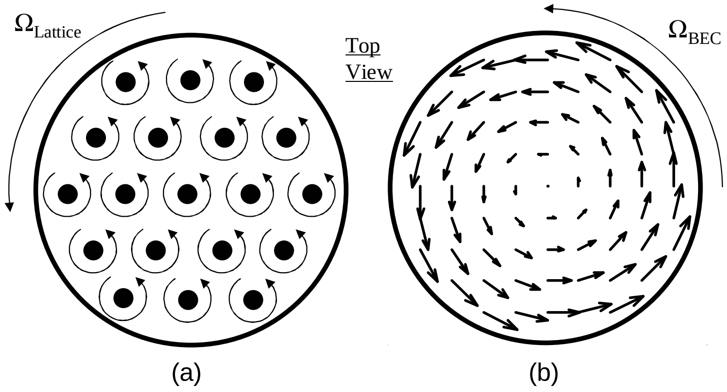

Figure 4.1: (a) Vortex lattice and (b) classical rigid-body rotation.

As a final note, in the rigid-body regime, the areal density n_V of vortices grows linearly with increasing rotation of the condensate. However, even though rotation rates up to 95% of the centrifugal limit are demonstrated in this chapter, the vortex distribution remains in the "dilute limit" where the spacing between vortices $\sim n_V^{-1/2}$ is much larger than the typical core size given by the healing length. Since the core size grows with decreasing atomic density, the limit of a *very* rapidly rotating, distended condensate and reduced atom number allows vortices to begin to approach one another. The "true" quantum limit is ultimately reached where a vortex occupies the same area as an atom in the condensate. Under these circumstances recent theory [63, 133, 101, 146] predicts the transformation of the condensate from a vortex lattice state to a strongly correlated quantum system, associated with quantum Hall physics. The techniques developed in this chapter hopefully will provide the starting point for achieving this new regime of rotating condensate physics.

4.2 Intrinsic vortex nucleation [97]

4.2.1 Abstract

We have developed an evaporative cooling technique that accelerates the rotation of an ultra-cold ^{87}Rb gas, confined in a static harmonic potential. As a normal gas is evaporatively spun up and cooled below quantum degeneracy, it is found to nucleate vorticity in a Bose-Einstein condensate. Measurements of the condensate's aspect ratio and surface-wave excitations are consistent with effective rigid-body rotation. Rotation rates of up to 94% of the centrifugal limit are inferred. A threshold in the normal cloud's rotation is observed for the intrinsic nucleation of the first vortex. The threshold value lies below the prediction for a nucleation mechanism involving the excitation of surface-waves of the ground-state condensate.

4.2.2 Introduction

To paraphrase an ancient riddle, what happens when an irresistible torque meets an irrotational fluid? The answer has been known for more than 50 years: a quantized vortex is nucleated. Vortices alone contribute to a superfluid's rotation, so that the bulk of the fluid may remain curl-free. The nucleation of vortices in bulk superfluid Helium has been the topic of extensive study (for a review see [74]). In the archetypical experiment, a rotatable pot filled with a mixture of superfluid and normal liquid Helium undergoes gradual angular acceleration. The normal fluid and the walls of the pot rotate together as a rigid body, defining a rotating environment. At some threshold angular velocity, a vortex line is nucleated at the circumference of the pot, and then quickly migrates inward until it is collinear with the axis of rotation. Further angular acceleration results in the nucleation of more vortices; eventually the fluid is filled with an array of vortex lines [29]. A central theme [30] of this research is the question: to what extent is the nucleation process "extrinsic," *i.e.* dependent on such details as the roughness of the surface of the walls, and to what extent is it “intrinsic” [31, 32], *i.e.* driven (in the limit of microscopically smooth walls) by the flow of normal fluid along the boundary of the superfluid? In the analogous rotating-potential experiments with a dilute-gas Bose-Einstein condensate (BEC), the confining potential and the normal fluid typically rotate at different rates [94]. In this context, the extrinsic-intrinsic question can be restated as: is it the confining potential or the normal fluid that defines the rotating environment?

Vortices in a BEC have been created with wavefunction engineering [33], through the decay of solitons [50, 75], and in the wake of moving objects [104, 34]. The first rotating-potential experiment to detect vortices in a BEC was performed by the Paris group [118]; results have also been obtained by the MIT [48] and Oxford [103] groups. In these experiments the role of the normal fluid was secondary to that of the rotating potential; it is conceivable the normal fluid was not rotating at all. This section presents vortex nucleation experiments performed in the opposite limit, namely in the environment of a rotating normal gas in a static confining potential. Such an environment allows for the isolated study of the intrinsic mechanism for vortex nucleation.

4.2.3 Evaporative spin-up

Our experiments begin with a magnetically trapped cloud of about $6 \cdot 10^6$ ^{87}Rb atoms, in the $|F = 1, m_F = -1\rangle$ hyperfine state, cooled close to the critical temperature $T_c = 67$nK. The atoms are initially confined in an axially symmetric, oblate and harmonic potential [136] with axis of symmetry along the vertical (‘z’) axis. To induce rotation of the cloud, we first gradually apply an elliptical deformation to the potential in its horizontal plane of symmetry, and then rotate the deformation [109] about the vertical axis at a fixed angular frequency. The rotating potential is characterized by an axial frequency $\omega_z = 2\pi(13.6)$Hz, average radial frequency $\bar{\omega}_\rho = 2\pi(6.8)$Hz and a horizontal ellipticity of 25%. Such a large rotating trap asymmetry, accessible in the oblate configuration of our apparatus, is found to be necessary not only to get the cloud rotating, but also to sustain ongoing rotation. Moreover, in steady state the cloud does not reach the rotation rate of the applied asymmetry. We believe that the stirring process is fighting a small, static asymmetry that acts to despin the cloud [35].

In thermal equilibrium, a normal cloud rotates as a rigid body with the centrifugal force causing the cloud to bulge outwards in the radial direction. In order to detect the rotation, we use a nondestructive phase-contrast technique to image the cloud *in situ* from the side. Four sequential pictures of a given cloud are taken to average over oscillations in the widths and to improve the signal to noise. The cloud temperature is extracted from its vertical width σ_z, which is unaffected by rotation about the vertical axis. The rotation Ω_N of a cylindrically symmetric cloud is determined from the aspect ratio, $\lambda = \sigma_z/\sigma_\rho$, using the relation:

$$\Omega/\omega_\rho = \sqrt{1 - (\lambda/\lambda_o)^2} \tag{4.1}$$

where λ_o is the static aspect ratio. The technique of side-view imaging is crucial for distinguishing between changes in radial size due to temperature and to rotation.

For stirring rates up to 2.5Hz, the rotation of the cloud reaches its steady-state value by 15s or less. After 15s, the rotating trap asymmetry is ramped off, leaving non-condensed clouds a factor of $1.2 - 1.3$ above T_c, for stirring frequencies $0 - 2.5$Hz. Radio frequency (rf) evaporation is then used to cool the normal cloud to BEC. In the oblate configuration of our TOP trap [136], we have found that rf evaporation immediately quenches the rotation, presumably because the selection process, which removes atoms with large radial displacements, preferentially removes atoms with large axial components of their angular momentum. By adiabatically distorting the trap into a prolate geometry with $\{\omega_\rho, \omega_z\} = 2\pi\{8.35, 5.45\}$Hz [78], we can instead cool the cloud by removing atoms with large *axial* displacements and thereby reduce the effect of the evaporation on the axial angular momentum [Figure 4.2]. As the normal

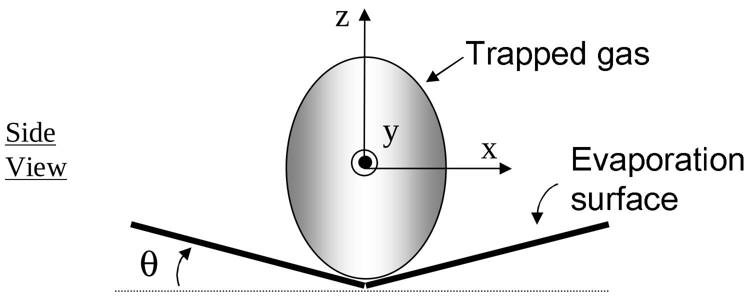

Figure 4.2: Vertical crosssection of the evaporation surface in the prolate confining geometry of the TOP trap. The surface, which represents a contour of magnetic field at which the radio-frequency evaporation is resonant, forms a shallow cone in three dimensions with an angle $\theta \lesssim 10°$ from the horizontal. The prolate shape of the confining potential has the effect of making the evaporation surface effectively shallower ($\theta_{eff} \lesssim 6°$).

cloud is evaporated, its aspect ratio is observed to decrease continuously, indicating a monotonically increasing rotation rate (Fig. 4.3a). During the evaporation, the angular momentum per particle of the normal cloud remains roughly constant, even though the number of atoms is reduced by over a factor of five and temperature, by a factor of four (Fig. 4.3b). As the cloud cools and shrinks, it must spin up for the angular momentum per particle to remain fixed.

To reach significant rotation rates by the end of evaporation requires the lifetime of the normal cloud's angular momentum to be comparable to the evaporation time. The nearly one-dimensional nature of the evaporation together with the low average trap frequencies make cooling to BEC in the prolate trap very slow (∼50s). We obtain angular momentum lifetimes this long [Figure 4.4] by shimming the azimuthal trap symmetry to better than 0.1%.

4.2.4 Highly rotating pure condensates

Towards the end of the evaporation, a condensate begins to appear at the center of the rotating normal cloud [36]. We discuss first the results of experiments in which

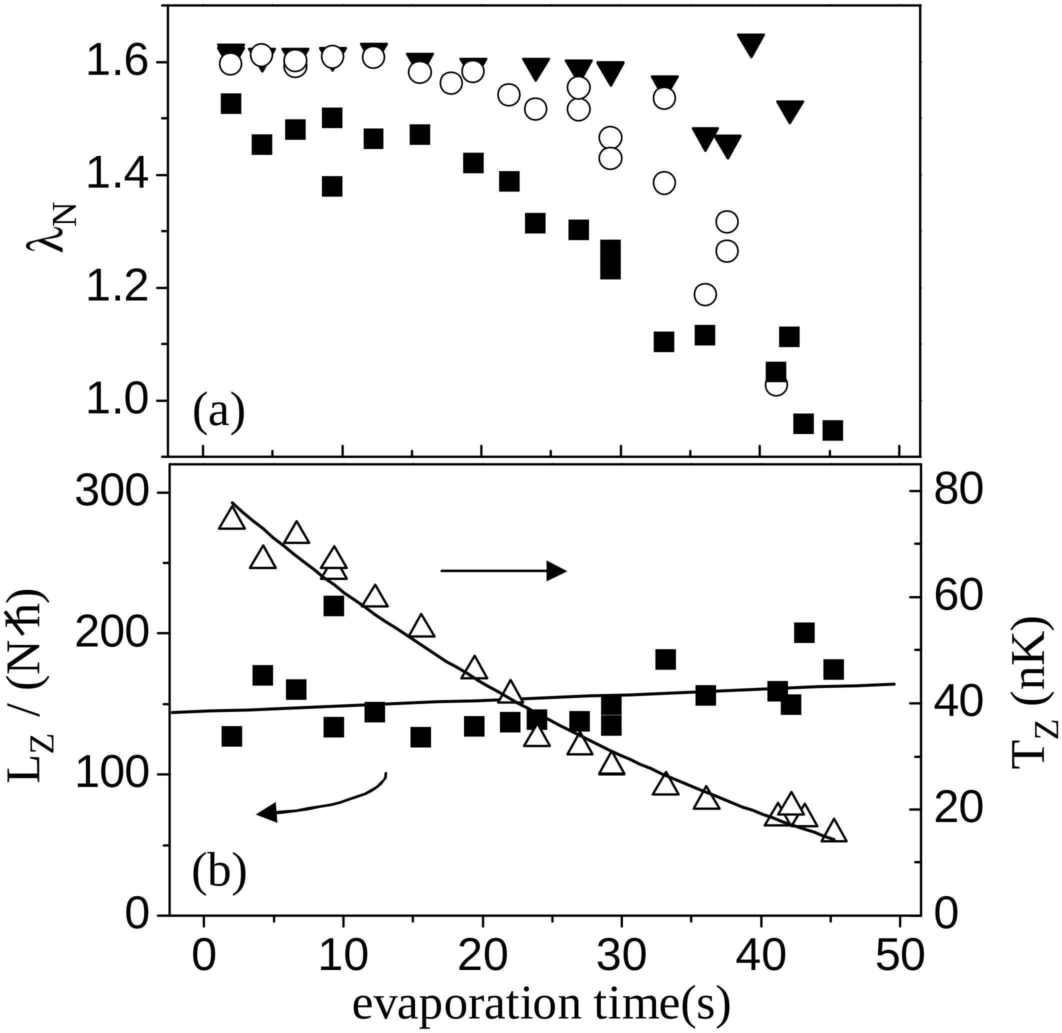

Figure 4.3: (a)Aspect ratio λ_N of a rotating normal cloud during evaporation preferentially along the axis of rotation. Data for three initial cloud rotations are shown, obtained by first stirring for 15s with an applied rotation of $0\bar{\omega}_\rho$ (inverted triangles), $0.07\bar{\omega}_\rho$ (open circles) and $0.37\bar{\omega}_\rho$ (squares). (b)Angular momentum per particle (squares) and temperature (triangles) of the normal cloud during evaporation for the $0.37\bar{\omega}_\rho$ case.

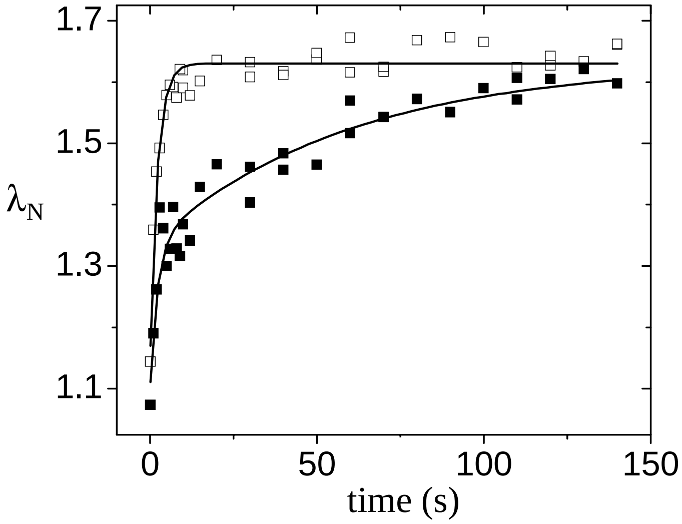

Figure 4.4: Aspect ratio of a normal cloud as a function of time after transfer to the prolate confining geometry. Open (filled) squares indicate the case of a static (rotating) cloud. The lines correspond to exponential decay fits with a single time constant τ_1=2.2(2)s for the static case and two time constants, τ_1=2.2s fixed and τ_2=60(6)s, for the rotating data. The initial rapid decay associated with τ_1 is on the order of the collison rate in the gas and corresponds to rethermalization of the cloud shape to the new confining geometry. The longer decay of the rotating cloud's aspect ratio is associated with the damping of its rotation as a result of residual trap asymmetries.

we continue the evaporation until little or no normal fraction remains. In this case, we find that the rotating normal component has given birth to a condensate distended in its radial dimension, as one would expect for a classical rotating body under the influence of the centrifugal force [Figure 4.5]. This effect is reminiscent of liquid Helium experiments, in which the surface of a rotating bucket of superfluid exhibits the same meniscus curvature as for an ordinary viscous fluid [37]. For large enough numbers of vortices in the condensate, the correspondence principle would suggest that the rotation field, coarse grained over the cloud, should go over to the classical limit of rigid-body rotation. In this limit, the classical Eq. (4.1) should connect condensate aspect ratio to rotation rate.

Alternatively, we can study the angular momentum in the BEC directly by excit-

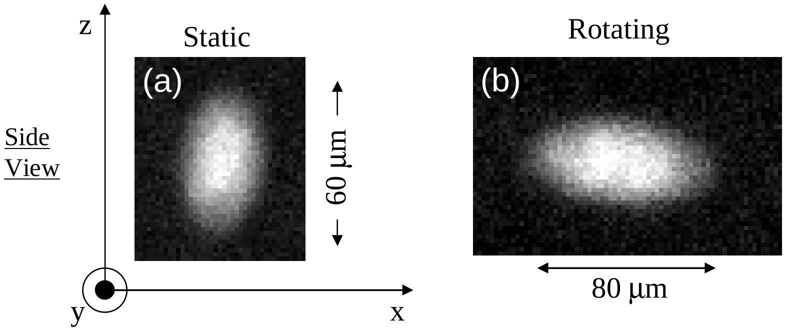

Figure 4.5: Side view images of (a) a static and (b) a highly rotating condensate. The imaged clouds are characterized by atom number $\{3.3{\cdot}10^6,\ 4.5{\cdot}10^6\}$ and aspect ratio $\{1.586,\ 0.5\}$.

ing quadrupolar surface waves [61, 98] with a rotating weak deformity of the magnetic trap. The quadrupolar surfaces waves are characterized by angular momentum quantum number $m_z = +(-)2$ describing an excitation that is co-(counter-)propagating with the rotation of the condensate. By varying the initial stir rate applied to the normal cloud, condensates of different aspect ratio can be accessed for study. In Fig. 4.6a, the frequency of the $m_z = \pm 2$ modes is shown as a function of condensate aspect ratio. The $m_z = +2$ mode is seen to speed up and the $m_z = -2$ to slow down due to the presence of vorticity in the condensate.

For small rotation rates, the splitting between the $m_z = \pm 2$ modes is predicted to be linearly proportional to the mean angular momentum of the condensate [39, 161] (see, though, Section 3.7). In the large-Ω limit of rigid-body rotation, Zambelli and Stringari [161, 38] have used a sum-rule argument to show that the splitting between the modes is simply 2Ω, and, further, that the sum of the squared frequencies of the two modes is independent of rotation rate. Cozzini and Stringari [66] have shown that hydrodynamic equations including a rigid-body rotation field $\vec{\Omega} \wedge \vec{r}$ reproduce the sum-rule result. The frequencies of the $m = \pm 2$ modes are explicitly:

$$\omega_{\pm 2} = \sqrt{2\omega_\rho^2 - \Omega^2} \pm \Omega. \tag{4.2}$$

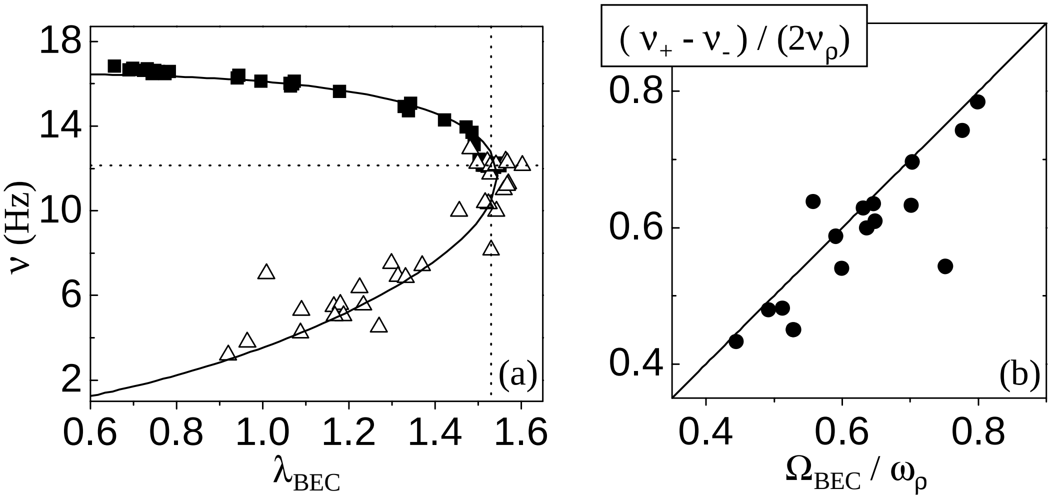

Figure 4.6: Quadrupolar surface-wave spectroscopy of condensates formed in a rotating normal cloud. (a)Quadrupolar frequency as a function of condensate aspect ratio for the $m = +2$ (squares) and $m = -2$ (triangles) surface waves. Solid lines are a single fit to the combined data using the theory of Zambelli and Stringari [161, 38]. Dotted lines indicate average frequency and aspect ratio for a static BEC. (b)The splitting between $m = \pm 2$ frequencies scaled by twice the radial trap frequency, plotted explicitly as a function of BEC rotation rate inferred from the aspect ratio. The solid line is the prediction from the same theory as in (a). Each plotted point is obtained from a single $m = -2$ measurement in (a) combined with a spline interpolation to the relatively quiet $m = +2$ data. Only aspect ratios smaller than 1.43 (corresponding to $\Omega_{BEC}/\omega_\rho \geq 0.35$) are included to avoid obtaining imaginary rotation frequencies due to experimental noise in the aspect ratio.

A best fit of this model to the combined $m = \pm 2$ data is shown in Fig. 4.6a, where the rigid-body rotation rate has been inferred from the condensate aspect ratio and the classical Eq. (4.1). Perhaps more intuitively, the frequency splitting is plotted explicitly versus inferred rotation rate in Fig. 4.6b. The excellent agreement with the model of Zambelli and Stringari is compelling evidence in favor of the reasonableness of using Eq. (4.1) to connect the condensate aspect ratio with its effective rotation rate. This is further born out by extensive 3-D numerical simulations of the Gross-Pitaevskii equation for the parameters of our experiment, by Feder and Clark. Their numerical simulations confirm that a condensate in an environment rotating at frequency $\Omega > 0.5\ \omega_\rho$ will equilibrate close to the aspect ratio given by Eq. (1) [40].

In pure condensate samples we have observed aspect ratios as pronounced as $0.35\ \lambda_o$, corresponding to a rotation rate of $0.94\ \omega_\rho$. The rapid rotation rate, combined with the increased condensate area arising from its radial bulge, mean that the condensate must be supporting a large number of vortices. Feder and Clark [40] calculate 56. With these initial conditions, we have observed continued rotation for at least 140 s.

4.2.5 Mutually rotating condensate and normal cloud

If the evaporation is stopped before the normal cloud has been completely removed, a comparison can be made between the aspect ratios, and hence rotation rates, of the condensate and normal cloud. By adjusting the initial stir rate applied to the normal cloud and the depth of the evaporation, we are able to reach different rotation rates for a given condensate fraction. After the evaporation is stopped, a time of 5 s is allowed for the gas to rethermalize to the last evaporative cut. We then take four nondestructive pictures and fit the images to a two-component distribution. Figure 4.7 shows a plot of the condensate aspect ratio λ_{BEC} compared with the aspect ratio λ_N of the normal cloud where each point represents a single realization of the experiment.

For $\lambda_N < 1.36$ ($\Omega_N > 0.5\ \omega_\rho$), the condensate aspect ratio closely tracks the

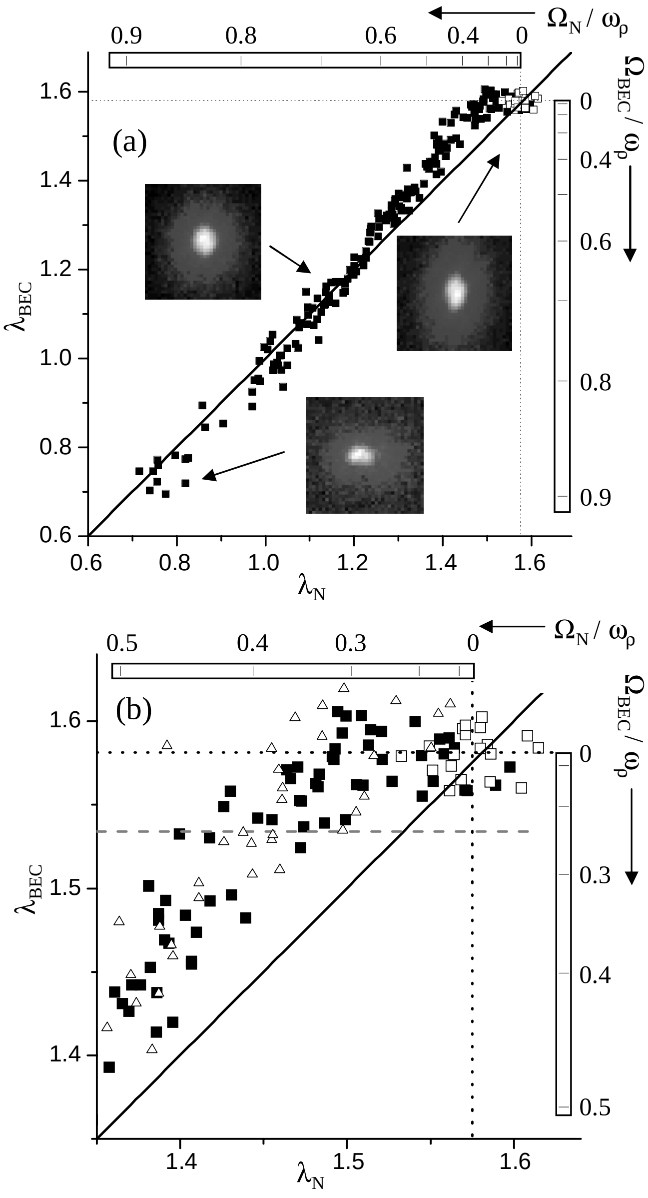

Figure 4.7: (a)Aspect ratio of the BEC vs. that of the normal cloud after evaporation halted. Right and top scales provide a conversion from aspect ratio to classical rigid-body rotation rate for BEC and normal cloud respectively. Data for evaporation of both a static (empty squares) and rotating cloud (filled squares) are shown. Dotted lines indicate average static aspect ratios for both BEC and normal cloud. A solid 1:1 line is superimposed on the data. Three representative integrated density profiles of two-component clouds indicate the range of different aspect ratios observed. (b)A magnified version of the region of high aspect ratio (low rotation rate) in (a). Added to the plot are data (triangles) obtained with evaporative spin-up 3 times slower than for the filled squares. A dashed line indicates the aspect ratio expected for a BEC with a single, centered vortex as calculated by Feder and Clark [40].

normal aspect ratio, providing a further manifestation of the correspondence principle for a highly rotating BEC. In the vicinity of $\lambda_N = 1.48$ ($\Omega_N = 0.35\ \omega_\rho$), we observe threshold behavior in the condensate rotation. At this low value of rotation we don't expect the rigid-body model to be valid for the condensate; but we make use of a numerical calculation by Feder and Clark [40] to indicate the change in condensate aspect ratio associated with the presence of a single, centered vortex (Fig. 4.7b). There is considerable scatter in the data so one cannot make a strong statement about the nature of the threshold shape, but clearly, somewhere between $0.32 < \Omega_N/\omega_\rho < 0.38$ the first vortex is nucleated.

A comparison of the observed threshold with two theoretical rotation rates provides some insight into the nature of the vortex nucleation. The first theoretical value is Ω_c, the critical rotation rate for thermodynamic stability of a single vortex. For our experiment (with $3 - 8{\cdot}10^5$ atoms in the condensate component) Ω_c is $0.2 - 0.25\ \omega_\rho$[41], distinctly lower than our observed threshold for nucleation. The second value is ω_{min}, the frequency at which the slowest surface-wave mode propagates around the circumference of the condensate. The Paris group has shown that for their "extrinsic" nucleation process (vortices nucleated by a rotating asymmetric potential) the key mechanism is the nonlinear excitation of surface waves [118, 117]. Results from MIT [34, 48] and from Oxford [103] are also consistent with such a mechanism. For the parameters of our experiment, $\omega_{min} = 0.4\ \omega_\rho$ [68]. Our observed threshold for "intrinsic" nucleation is clearly under this value; thus, interpreting our effect in terms of a normal "wind" exciting surface waves on the condensate is problematical. However, because the confining potential is not rotating in our case, the vortex nucleation can only arise from interaction with the rotating normal cloud.

The data presented in Fig. 4.7 include a range of condensate fraction from 0.1-0.45 for each rotation rate of the normal cloud, although no segregation relative to either axis is evident for plots of different BEC fractions. Moreover, by reducing the rate of evaporation, we have decreased the rate of acceleration of the normal cloud rotation by a factor of 3, and still observe a threshold for vortex formation between 0.32 and 0.38 (Fig. 4.7b).

Threshold behaviour aside, the rotating normal cloud can create equilibrated condensates with very large rotation rates. This may allow us in future work to approach the regime for which the vortices are so close-packed that their separation becomes comparable to their core size, given by the healing length of the condensate [101].

4.3 Theory responds

The experimental results of the previous section have initiated a discussion in the literature [158, 53, 134, 145] as to the mechanism for vortex nucleation in the presence of a rotating normal cloud. The consensus of the theory to date is that the mechanism is ultimately the same as in the "extrinsic" experiments where vortices are nucleated with a rotating asymmetric potential. In other words, the nucleation is driven in both cases by surface-wave instabilities, which allow a vortex to overcome the energy barrier at the condensate surface and thereby enter into the bulk [68]. For a rotating potential, the rotation threshhold for the onset of vortex nucleation is set by the minimum surface-wave frequency

$$\Omega_S = \min_{\ell} \left[\frac{\omega_\ell}{\ell} \right] \tag{4.3}$$

where $\ell\hbar$ defines the angular momentum of the surface mode with frequency ω_ℓ. The above equation is a generalization of the well-known Landau criterion [113] with the critical velocity now given by $v_c = \Omega_S R$ on a condensate of radius R. For typical experimental parameters, $\ell_{min} \approx 10$ [68, 53, 134]. In an actual experiment, the nucleation threshhold may end up somewhat higher than Ω_S if the surface roughness of the rotating potential does not contain a spherical harmonic order ℓ high enough to couple to the minimum surface wave [68].

In the intrinsic nucleation experiments, one can think heuristically of the "wind" of the normal cloud, instead of the rotating potential, driving the surface-waves on a condensate. More technically, though, one can speak of the gain of a surface mode, which depends on the mode's velocity relative to the normal cloud [158, 134]:

$$\gamma = \gamma^{(0)} \left(\frac{\ell \Omega_N}{\omega_\ell} - 1 \right) \tag{4.4}$$

For a static normal cloud ($\Omega_N = 0$), all of the surface modes experience a negative gain or, in other words, are damped. However, if the normal cloud is brought into rotation, the gain of one or several surface modes on the condensate may become positive leading to an instability. The onset of the first instability will occur when the normal cloud rotation is resonant with the slowest surface wave: $\Omega_N = \Omega_S$. More generally, for an arbitrary rotation rate, Penckwitt et al. [134], using a condensate growth model, have shown that the surface mode with the largest gain will dominate the vortex nucleation. The ℓ value corresponding to maximum gain can be found from $\partial_\ell(\frac{\ell\Omega}{\omega_\ell} - 1) = 0$ and matches ℓ_{min} from Eqn. 4.3 at threshhold.

The primary point of contact between theory and experiment is the location of the threshhold for first vortex nucleation. The experimentally observed threshhold from the previous section lies in the range $0.32 < \Omega_N/\omega_\rho < 0.38$, which is somewhat lower than the slowest surface-wave $\omega_{min}/\omega_\rho = 0.4$ quoted for our experimental parameters [Section 4.2]. Anglin [53] provides an analytical expression for the rotation threshhold based on the local critical velocity at the Thomas-Fermi surface of a condensate. Applied to our experiment, this yields a threshhold value somewhat closer to the observed one - $\Omega/\omega_\rho = 0.41 - 0.36$ for condensate number in the range $3 - 8 \cdot 10^5$. The local surface theory is valid in the limit of short surface-wavelength where the penetration depth δ of the surface waves into the bulk of the condensate is small compared the Thomas-Fermi size of the condensate R. In terms of the radial harmonic oscillator length $a_\rho = (\hbar/(m\omega_\rho))^{1/2}$, the penetration depth is $\delta = (a_\rho^4/R)^{1/3}$. At threshhold, $\delta/R \approx 0.1$ and the theory is expected to reasonably valid.

4.4 Direct observation of vortex lattices

In our initial vortex nucleation experiments [Section 4.2], the vorticity within a condensate was detected indirectly from the centrifugal distortion of the density profile or from the presence of angular momentum sensed with surface-wave spectroscopy. Complementary to these techniques assessing “macroscopic” rotational effects is the direct detection of vortex cores in the density profile of a condensate when observed along the rotation direction (see also chapter 3). There is considerable interest in the “microscopic” structure of large amounts of vorticity, where the term “microscopic” is used to refer to the size scale of the vortex core. In particular, the minimum energy configuration for a reasonably rotating condensate at equilibrium is expected to consist of a large number of singly-quantized vortex cores arranged in a triangular lattice [59, 79, 54].

Triangular vortex lattices were first observed in a condensate at the ENS [118] and somewhat later at MIT [48] and Oxford [103]. Given that the intrinsic nucleation technique can produce highly rotating condensates ($\Omega_{BEC} = 0.95\omega\rho$), the system offers the potential to study large amounts of densely packed vorticity. For this reason as well as the added benefits of direct vortex detection, we were led to add a vertically oriented imaging axis to see down the rotation axis of the condensate. After the usual evaporative spin-up sequence to produce near pure rotating condensates [Section 4.2], the condensate’s confining potential is discontinuously removed and the condensate allowed to ballistically expand [27]. The expansion is continued until the vortex core size is large enough to be resolved with our imaging system at which point the density profile along the axis of rotation is imaged. Figure 4.8 shows typical images of condensates at different rotation rates, or equivalently, with different amounts of vorticity. The highly ordered triangular lattice structure is apparent in the images out to the edge of the

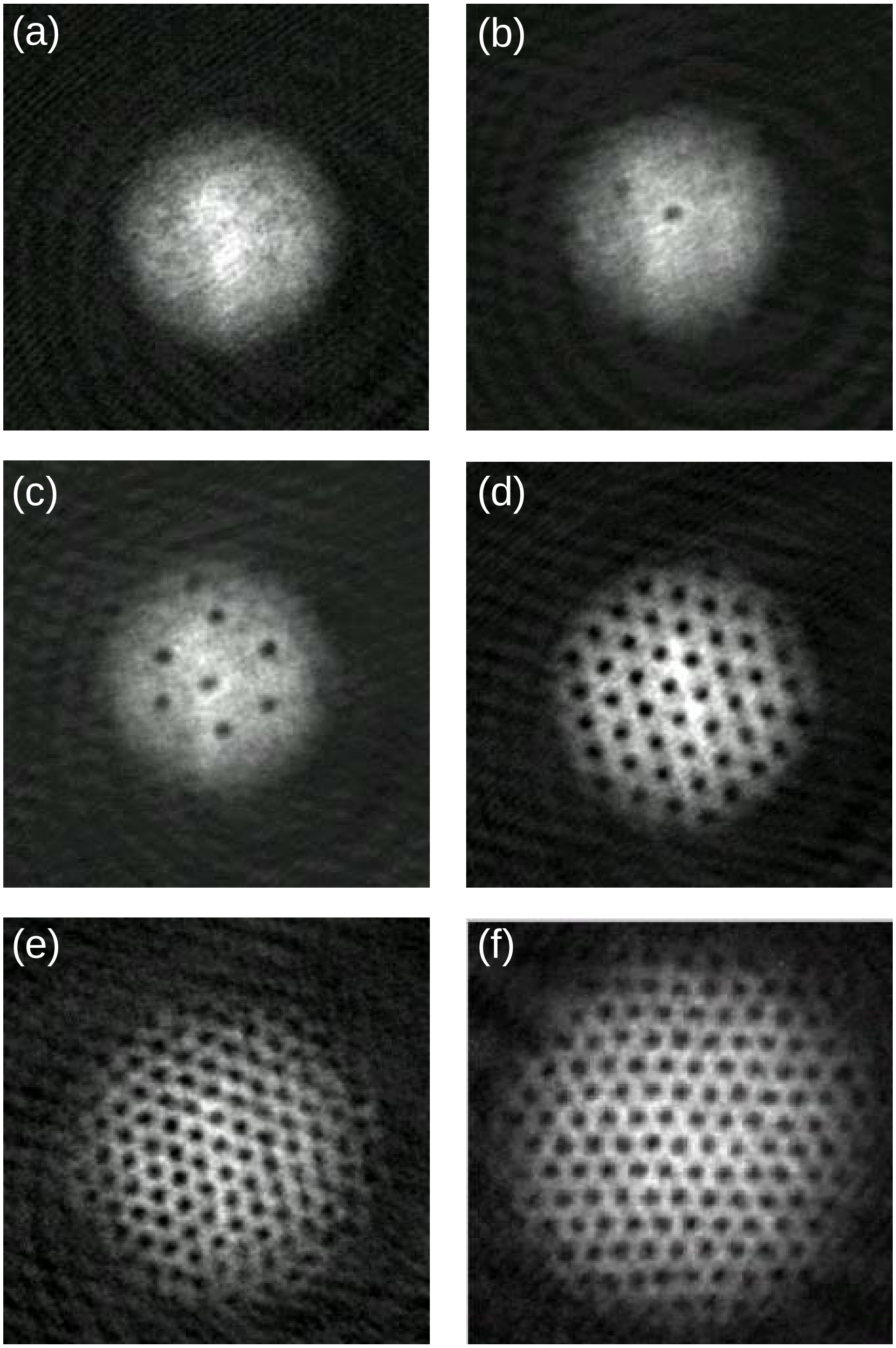

Figure 4.8: (a)…(f) Vortex lattices corresponding to condensate aspect ratio {1.53,1.54,1.42,0.96,0.5,0.54}. For (c)…(f), the corresponding rigid-body rotation rate $\Omega_{BEC}/\omega\rho$ is {0.4,0.8,0.95,0.94}. The condensate in (f) has about the same rotation as case (e) but is larger and contains more vortex cores because the number of atoms is significantly larger.

condensate, even though the density profile is non-uniform due to the inhomogeneous confining potential. It has recently been pointed out [79, 54] that the radially decreasing density profile in fact helps to *preserve* the triangular ordering by suppressing distortions in the lattice structure at the surface of the condensate.

Two applications of vortex core detection are considered here, one at low vorticity and one at high. In the first application, the vortex nucleation process of Section 4.2 has been revisited to verify the amount of vorticity at threshhold. In the original experiment, numerical simulations [79] were relied upon to provide the aspect ratio for a condensate in the presence of small numbers of vortices. This permitted the identification of the nucleation threshhold with the creation of a *single* vortex. The new ability to detect vortex cores in ballistic expansion allows this to be directly confirmed in the experiment.

A set of data has been acquired similar to that in figure 4.7, where a normal cloud is spun up to varying degrees and then evaporatively cooled until a condensate component appears. The average condensate fraction for the data set is $N_{BEC}/N \sim 0.34$. An *in-situ* non-destructive image is taken from the side to permit a comparison of the aspect ratios of the condensate and normal cloud. The sample is then ballistically expanded and imaged from the top to allow for the visual identification of vortex cores in the condensate. In figure 4.9, the aspect ratio of the condensate is plotted against that of the normal cloud near threshhold, where the data points are now identified according to vortex number. The vortex counting for the data set has been performed by eye. It is clear that the nucleation threshhold is indeed associated with the presence of a single vortex in the condensate. In other words, the threshold is low enough that, after nucleation, single vortices are energetically favored. Only at a slightly higher normal cloud rotation ($0.4 \lesssim \Omega_N/\omega\rho \lesssim 0.5$) do two and three vortices begin to appear. This may help to solidify the connection between the experimental data and numerical simulations of the nucleation [134] where single vortices should be found to occur at threshhold.

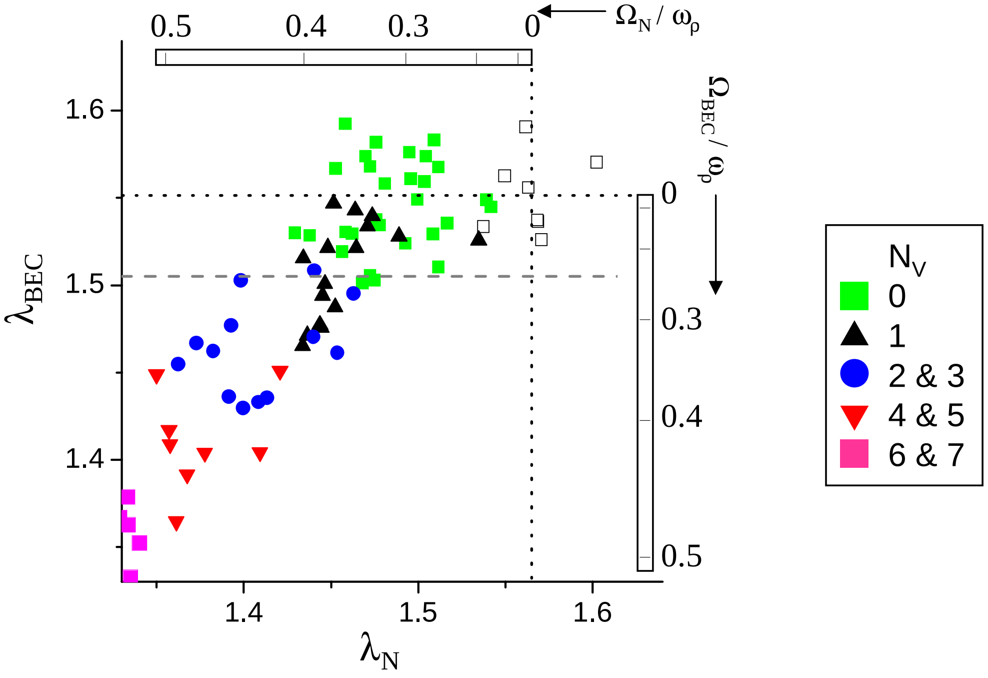

Figure 4.9: The threshhold for vortex nucleation repeated as for figure 4.7, but with direct vortex detection now used to identify the number of vortices for each data point (see legend). The open squares are obtained by evaporative cooling of a static normal cloud. The axes and dashed and dotted lines are as defined in Figure 4.7.

The aspect ratio for a condensate with a single centered vortex, as calculated by Feder [79], is also corroborated by the data in figure 4.9. Notwithstanding the measurement noise inherent in the data, it is not surprising that several single vortex points appear in the plot region between static and single vortex aspect ratios: if a vortex is offset from the condensate center, it will have less of a centrifugal effect on the radial size. Indeed, by and large, the single vortices were not found to be perfectly centered on the condensate. This effect not only helps to explain the smoothness of the nucleation threshhold when plotted in terms of aspect ratio but also substantiates the position of the threshhold, $0.32 < \Omega_N/\omega_\rho < 0.38$, as originally identified. Further refinement of the measured critical rotation rate can be achieved only by reducing systematic errors and noise in the determination of the normal cloud's aspect ratio.

The data set has been continued to higher rotation rates of the normal cloud where more and more vortices enter into the condensate. Under these circumstances it is possible to study the number of vortices in the condensate as a function of its effective rigid-body rotation rate Ω_{BEC}, which can be inferred from its aspect ratio λ_{BEC} in the usual way [Eqn. 4.1]. Since the condensates are formed in equilibrium with a rotating normal cloud, the vortex number is expected to correspond to the equilibrium value. The limit of effective rigid-body rotation is characterized by a uniform distribution of vorticity with areal density $n_V = 2\Omega/\kappa$ [155]. Here $\kappa = h/m$ is the quantized circulation of a single vortex and m is the mass of a condensate atom. For a condensate with a radial size given by Thomas-Fermi radius R_ρ, the number of vortices in the rigid-body approximation is $\pi R_\rho^2 n_V$, which can be expressed explicitly as:

$$N_V^{rb} = \frac{2\mu_0}{\hbar\omega_\rho}\frac{\Omega/\omega_\rho}{(1-\Omega/\omega_\rho)^{3/5}} \tag{4.5}$$

In the previous equation, $\mu_0 = m\omega_\rho^2 R_\rho(0)^2$ is the chemical potential of the condensate in the absence of rotation, expressed in terms the static Thomas-Fermi radius $R_\rho(0)$ in the radial direction. There is a weak dependence on the number of atoms in the condensate through $R_\rho(0)^2 \sim N^{2/5}$. It is also worth noting that, in the rigid-body approximation, the number of vortices included in a Thomas-Fermi condensate is related to the angular momentum per particle [66] by

$$N_V = \frac{7}{2}\frac{\langle \ell_z \rangle}{\hbar} \tag{4.6}$$

In figure 4.10, the raw number of vortices for the current experimental data set is plotted as a function of the aspect ratio of the condensate. Additionally, data from a later run using a more efficient spin-up technique [Section 4.7] is included and involves experimental conditions that are significantly different in the following ways: The evaporation has proceeded until little normal cloud is visible; higher rotation rates are included; and the condensates have larger number, corresponding to a static Thomas-Fermi radius R$_\rho$ $\sim$30μm compared with 21μm for the current set of data. The static chemical potential μ_0 has a correspondingly larger value of $33\hbar\omega_\rho$ compared with $16\hbar\omega_\rho$. As a result, it is not surprising that the later data set shows a larger number of vortices for a given rotation rate [Figure 4.10(a)]. However, by plotting the reduced vorticity $N_V\hbar\omega_\rho/2\mu_0$, the dependence of N_V on condensate number can be removed [Figure 4.10(b)]. The fit Thomas-Fermi radius for each plotted point is used to calculate the chemical potential μ_0 in order to remove intra-data-set fluctuations as well. Expressed in terms of the reduced vorticity, the data sets are now seen to match over a wide range of aspect ratio.

The rigid body prediction [Eqn. 4.5] has also been included in the plot for comparison. It is quite clear that the experimental data tracks but consistently lies below the rigid-body value. Possible systematic errors will be discussed below; however, a numerical calculation by Feder and Clark [79] for a condensate with $2 \cdot 10^5$ atoms in a similar confining potential matches the data extremely well over the entire range of aspect ratio shown in figure 4.10(b). In their numerical simulations of rotating condensates, Feder and Clark have found that the aspect ratio and moment of inertia $\langle L_z \rangle/\Omega$ approach their classical rigid-body values with increasing rotation, but the number of vortices lags considerably behind the expectation according to Eqn. 4.5. For example, in the case of a condensate rotating at 95% of the centrifugal limit ($\Omega_{BEC}/\omega_\rho = 0.95$), the aspect ratio and moment of inertia are found to be within a few percent of the rigid body predictions, even though the vortex number is 65 compared to the rigid-body value of 89. The simulations further show that the vortex density does agree with the rigid-body distribution in the bulk of the condensate; only at the edge of the condensate does a discrepancy arise where at least one hexagonal ring of the triangular vortex lattice is missing. The lattice is nevertheless stationary in the rotating frame which raises the question: what provides the extra rotation to make up for the missing vorticity? The answer lies with the inhomogeneous confining potential. The resulting non-uniform density profile of the condensate contributes a radial force that, according to the Magnus

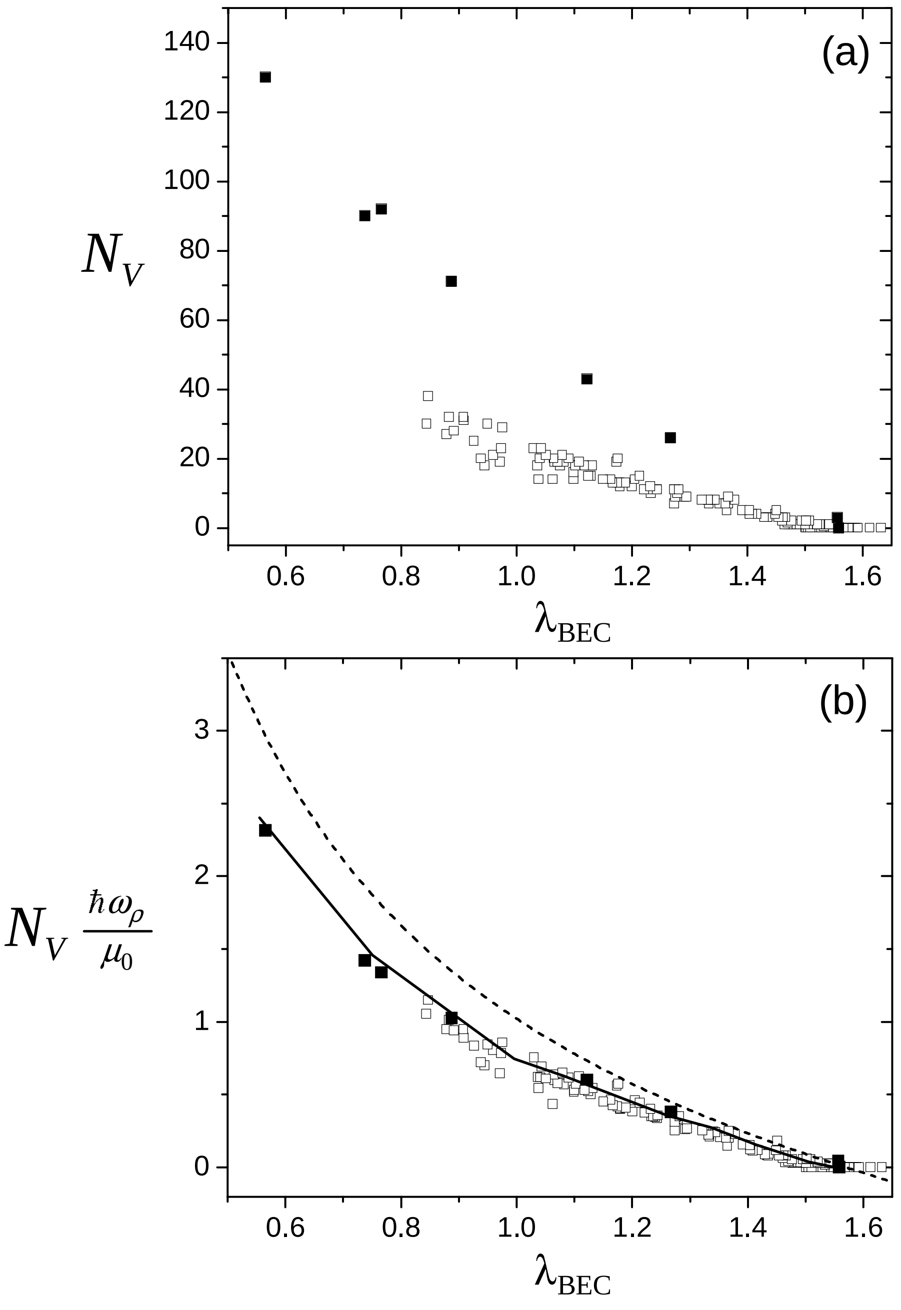

Figure 4.10: (a)Vortex number as a function of BEC aspect ratio for two different experimental runs, in particular with an average condensate number of $0.4 \cdot 10^6$(open squares) and $2 \cdot 10^6$(filled squares). A lower aspect ratio indicates a faster effective rigid-body rotation rate. (b) Reduced vortex number plotted as a function of BEC aspect ratio. The uniform rigid-body prediction (dotted line) and a numerical simulation by Feder and Clark [79](solid line) are added for comparison.

force [155], causes the vortices to rotate a little faster about the axis of the condensate. This additional rotational motion is precisely the core precession observed for single offset vortices in Chapter 3. Recent analytical results [54] show the same "conspiracy" of two microscopic rotational contributions to yield the overall macroscopic rigid body rotation field.

The natural question arises whether the disagreement between the data and rigid body prediction can be due to systematic errors in evaluating the reduced vorticity. The main dependence on experimental numbers is $N_V/(\omega_\rho R_\rho(0)^2)$. In figure 4.11, the ratio of the observed vorticity to the rigid body expectation N_V/N_V^{rb} is plotted as a function of aspect ratio and is found to be roughly a constant around $\sim 0.75 - 0.8$. This could be accounted for by a systematic error of 25% in the radial trap frequency $\omega_\rho = 2\pi 8.45$Hz, which can be ruled out, or a 12% systematic error in the determination of the condensate size R_ρ, which cannot be immediately ruled out at this time. The final possibility for error is in the actual counting of vortices present in the condensate. Because of the vanishing density at the edge of the cloud, the low signal-to-noise makes it difficult to identify vortices in this region of the image, particularly in the case of large vortex number.(Compare figures 4.8(c)&(f)). It may simply not be possible to conclude definitively whether or not there are vortices at the edge of the condensate contributing to a rigid-body rotation field. An automated vortex counting algorithm, not yet applied to the data presented here, may help and will at least provide an unbiased estimate of the counting error arising at the condensate surface.

In conclusion, direct vortex detection has been used to verify the single vortex character of the intrinsic nucleation threshhold and to study ordered triangular lattices composed of variable amounts of vorticity. The observed vortex number in a rotating condensate agrees with the rigid-body prediction within a constant factor of ~25%. Two possible systematics in the determination of condensate size and vortex number preclude a definitive statement regarding the observed deviation from the rigid-body

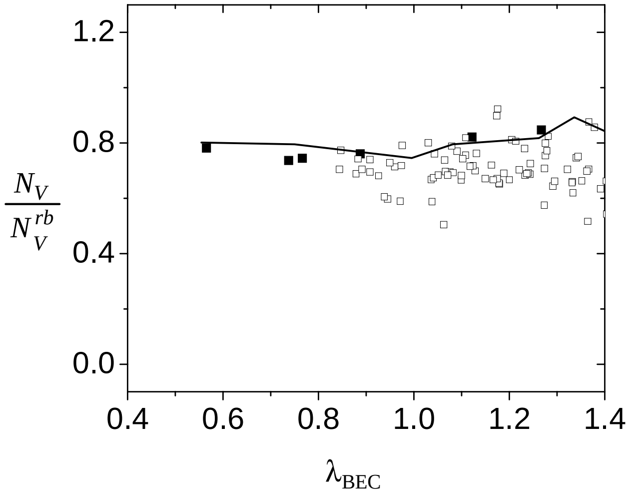

Figure 4.11: Ratio between observed vortex number with respect to rigid body prediction. Two separate data sets as in figure 4.10 are indicated by open and filled squares. The solid line represents the numerical simulation by Feder and Clark [79].

prediction. Nevertheless, the tantalizing agreement with theory justify further work in the future, including more data at higher vortex number and a comparison of the vortex lattice constant (vortex spacing) with theoretical predictions [79, 54]. It represents an interesting application of the correspondence principle to understand how the microscopic quantum vortex structure reacts in the presence of an inhomogeneous confining potential to mimic the macroscopic classical limit of effective rigid-body rotation.

4.5 Rotational suppression of the quantum degeneracy temperature

So far in this chapter, the phase boundary between vortex-free and vortex-full condensates has been considered as a function of the normal cloud rotation rate Ω_N. Another albeit simpler effect of the rotation is to suppress the quantum degeneracy temperature T_C, which forms the boundary between normal and condensed phases [149]. This effect may be accounted for by the centrifugal weakening of the radial harmonic confinement, $\tilde{\omega}_\rho = \sqrt{\omega_\rho^2 - \Omega^2}$, which leads to a reduction in the normal gas density n_{th} relative to the non-rotating case. As a result, a lower temperature must be reached before the phase space density ($\sim n_{th}/T^{3/2}$) is sufficiently high to bring about the BEC transition. The expression for T_C as a function of the rigid-body rotation rate Ω of the gas sample is

$$T_C = T_C^{(0)} \left(1 - \frac{\Omega^2}{\omega_\rho^2}\right)^{1/3} \tag{4.7}$$

In the above equation, $T_C^{(0)}$ is the static critical temperature. For a non-interacting gas in a harmonic potential, $T_C^{(0)} = 0.94\hbar\omega_{ho}N^{1/3}$ where N is the number of atoms in the sample and $\omega_{ho} = (\omega_\rho^2\omega_z)^{1/3}$ is the average trap frequency. In figure 4.12, the data originally from figure 4.7 have been used to plot condensate fraction versus temperature for three different ranges of sample rotation rate. All quantities are obtained from fits to the non-destructive *in-situ* images of the trapped gas clouds. As usual, the rotation rate has been assessed from the changing aspect ratio of the normal cloud according to Eqn. 4.1. It is qualitatively clear from figure 4.12 that a lower temperature is required at higher rotation rates to reach a given condensate fraction. For each data point, the temperature and condensate fraction can be used together to infer a value for the critical temperature of the sample. To remove shot-to-shot variation in T_C due to atom-number fluctuations, the value of the inferred transition temperature can be scaled by the static value $T_C^{(0)}$ calculated from the measured atom number. The scaled value of T_C is plotted against rotation rate in figure 4.13 for three ranges of temperature: "hot," "medium" and "cold," corresponding to three different ranges of condensate fraction.

Each group of data clearly show the suppression of T_C towards higher rotation. The *overall* suppression of T_C is roughly consistent with an effect associated with the interatomic interactions [69] although there may also exist systematic errors in the number or temperature calibrations.

The centrifugal suppression of T_C is perhaps less interesting than that due to many-body interaction effects; nevertheless, from a technical stand point, centrifugal effects are an important consideration in the evaporative cooling and spin-up process.

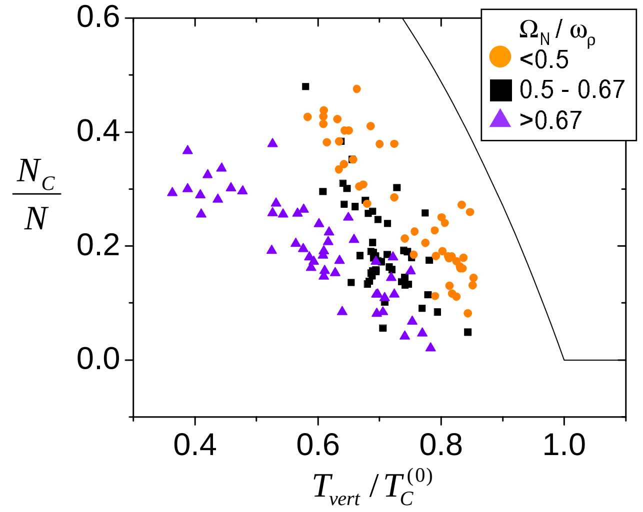

Figure 4.12: Condensate fraction versus temperature for various sample rotation rates. Condensate number N_C and total number N are obtained from fits to cloud images. The temperature T_{vert} is extracted from the vertical width of the normal cloud while the centrifugal distortion in the normal cloud's aspect ratio yields its rotation Ω_N. The temperature is scaled by the static critical temperature $T_C^{(0)}$ for an ideal gas (see text). The data has been grouped according to three different ranges of Ω_N (see legend). The solid line is the theoretical dependence expected for a static ideal gas.

As the gas rotation is continually increased during evaporative spin-up, it affects not only the critical temperature but also the collision rate $\gamma_{coll} \sim N/(T\tilde{\omega}_\rho^2)$. The effect of the weakening effective trap frequency $\tilde{\omega}_\rho$ is indeed a significant effect. Whereas the temperature decreases by a factor of $\sim$ 10 during an evaporation proceeding to a rotation of $\Omega/\omega_\rho = 0.95$, the value of $\tilde{\omega}_\rho^2$ changes by a factor of $\sim$ 20 such that the density and collision rate change little. Therefore the evaporative process lacks the hallmark "runaway" characteristic of an ever-increasing collision rate. In addition, the evaporative process operates in a weak confining potential ($\omega_{ho} \approx 2\pi 8$Hz) and removes atoms along only one dimension [Section 4.2]. In spite of violating the cherished rules of successful evaporation, the current typical evapoartion can produce highly rotating condensates ($\Omega/\omega_\rho \approx 0.95$) with sizeable atom number ($N \approx 2 \cdot 10^6$)! Of course the evaporation, starting not too far above T_C, takes several minutes to make a pure condensate.

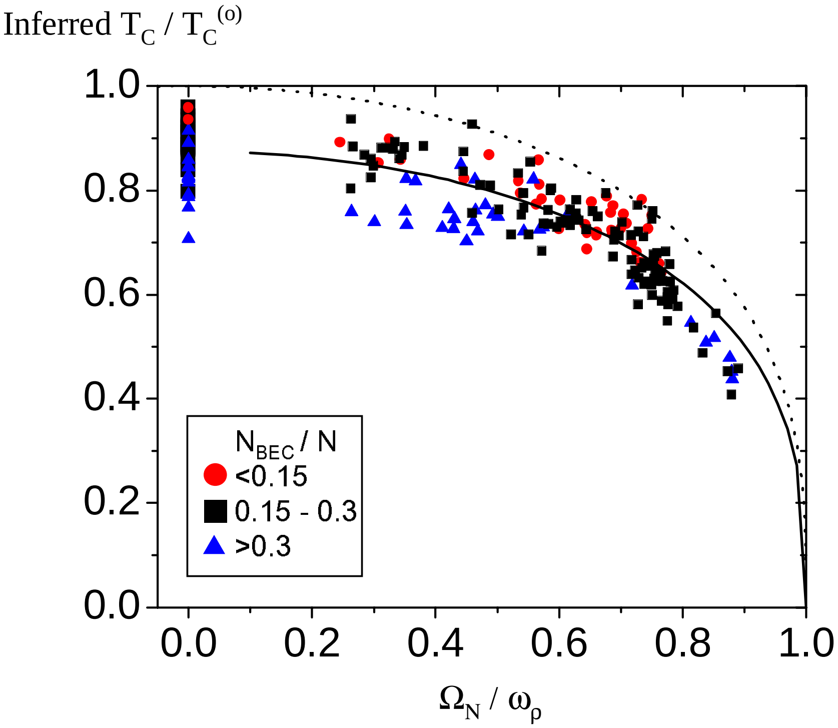

Figure 4.13: Inferred critical temperature T_C, scaled by the non-rotating expectation $T_C^{(0)}$ for an ideal gas, as a function of normal gas rotation Ω_N/ω_ρ. For each data point, T_C is inferred from the measured condensate fraction and temperature of a sample. The total number of atoms is used to obtain $T_C^{(0)}$. The data has been grouped according to three different condensate fractions as shown. A set of static points, where the normal cloud is not stirred before evaporation, are deliberately plotted at zero rotation. Otherwise, the rotation rate Ω_N is obtained from the normal cloud's aspect ratio. The rotating data has been cropped at a minimum threshhold $0.2 < \Omega_N$ to avoid imaginary rotation values arising from noise in near-static aspect ratios. The dotted line is the theoretical expectation according to Eqn. 4.7 with $T_C^{(0)}$ as for an ideal gas. The solid line is a fit of the data to Eqn. 4.7 with an arbitrary overall scaling of the vertical axis. The fit result is equivalent to assuming an effective $T_C^{(0)}$ that is 87(1)% of the ideal gas value.

4.6 Vortex lattice decay

Rounding out the “life cycle” of vortex lattices, a qualitative description of their decay from the condensate is presented here. The decay of vortex lattices [47] and single vortex lines [142] have also been studied in other experimental groups. As already mentioned in section 3.7, a rotating condensate spins down by passing vortices out to its edge where they decay in a shower of phonons. Since the vortex cores in a lattice are rotating about the condensate center, they reach the edge by spiraling outward. The radial damping of the vortices is driven by the frictional drag from collisions with the normal cloud [82]. If a vortex lattice is rotating in equilibrium with the normal cloud, the drag force on the vortices vanishes. If the normal cloud is faster, it pushes vortices into the condensate to bring it into rotational equilibrium. If slower, the normal cloud pulls vortices out of the condensate. In the macroscopic limit of large vorticity where the condensate and normal component may be characterized by rotation rates Ω_{BEC} and Ω_N respectively, the effect of the normal cloud can be summed up by a mutual friction $\gamma(\Omega_N - \Omega_{BEC})$, which is proportional to the relative velocity between the components [162] (see also Section 4.3). The phenomenological constant γ includes, among other effects, the temperature dependence.

The evaporative spin-up process initially forms a condensate and normal cloud rotating together (about the vertical $\vec{z}$-axis). In order to induce a decay in the rotation of the sample, a “surface roughness” must be present in the confining potential to break its rotational symmetry. Angular momentum is then no longer conserved in the system. The walls of our magnetic trap are essentially infinitely smooth, except for the lowest order ($\ell = 2$) roughness corresponding to an elliptical asymmetry [Figure 4.14]. This can be significantly reduced with some care, though residual asymmetries in our confining potential still cause relatively cold condensates to lose their rotation over the

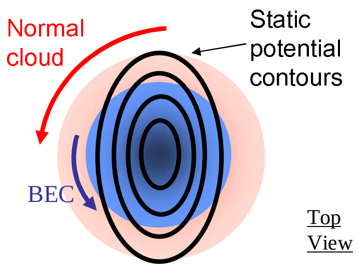

Figure 4.14: An ellipticity ("surface roughness") applied to the confining potential breaks rotational symmetry. This leads to the rotational relaxation of the initially co-rotating normal cloud and condensate.

span of minutes [1] . A theoretical model of angular momentum decay in the presence of a trap asymmetry is detailed in [162]. In a loose sense, the rotating condensate is a frictionless superfluid and is not slowed by the surface roughness of the potential (see, though, section 4.8). The rotation of the normal cloud will, however, damp due to the friction imparted by the roughness. With the condensate and normal fluid no longer in rotational equilibrium, the mutual friction will in turn damp the condensate's rotation. Thus, there are two relevant times scales τ_V and τ_R characterizing the transfer of angular momentum, first, from the condensate to normal fluid and, second, from the normal fluid to the trap walls, respectively. The value of τ_R in general depends on the atomic collision rate in the normal gas (typically ∼1Hz for our experimental parameters) and the strength of the static elliptical deformation $\epsilon = (\omega_x^2 - \omega_y^2)/(\omega_x^2 + \omega_y^2)$ present in the confining potential. (ω_x and ω_y are the harmonic trap frequencies in the horizontal directions). By controlling the strength of the ellipticity, it is possible to explore two regimes of rotational decay corresponding to a rapid ($\tau_R \ll \tau_V$) or gentle ($\tau_V \ll \tau_R$) stopping of the normal cloud's rotation.

In figure 4.15(a), the first of these situations is shown where a "strong" horizontal ellipticity $\epsilon \approx 0.02$ has been applied to mostly stop the normal cloud's rotation after ∼1-

---

[1] The loss of rotation can be countered in steady state by the continuous application of rf evaporation, which tends to spin up the cloud.

2s. Non-destructive, *in-situ* images are then taken of the trapped gas from the side and fit to extract the simultaneous aspect ratio of the condensate and normal component. While the value for the normal cloud lies near the static value after the stopping, the low value for the condensate indicates that it continues to rotate initially. Eventually the rotation of the condensate itself damps, presumably under the influence of the mutual friction from the static normal cloud. In figure 4.15(b) the rather different scenario of a weak applied asymmetry ($\epsilon \sim 10^{-3}$) is shown where the rotation of the condensate and normal component decay together at the same rate. If the trap ellipticity is sufficiently small, the mutual friction between the components is expected to dominate the friction between the normal component and trap walls. In this case, the condensate and normal fluid lock together as one system. The additional contribution of the condensate's moment of inertia to the total will cause the rotational relaxation of the system to proceed a little slower [162]. The quantitative analysis of the degree of "locking" for our experimental conditions as well as a detailed comparison with theoretical models is left to a future publication.

The aspect ratio analysis of figure 4.15 provides a convenient method to assess the macroscopic rotational decay of the condensate and normal cloud. A complimentary viewpoint can obtained by directly imaging the vortex cores in a condensate over the course of the decay. Several experimental runs have been made in which the rotational decay is allowed to proceed for a variable amount of time. The usual *in-situ* image is first made from the side to obtain aspect ratio information. The sample is then ballistically expanded and imaged vertically to reveal the vortex cores in the condensate. In figure 4.16, the rotation rate of the condensate as obtained from its aspect ratio is shown as function of time in conjunction with the corresponding expansion images of the vortex distribution. An automated program is used to identify the vortex cores in the density profile and to obtain their average spacing, which is also plotted as function of time. Figure 4.16 visually unifies the different perspectives of a condensate spinning

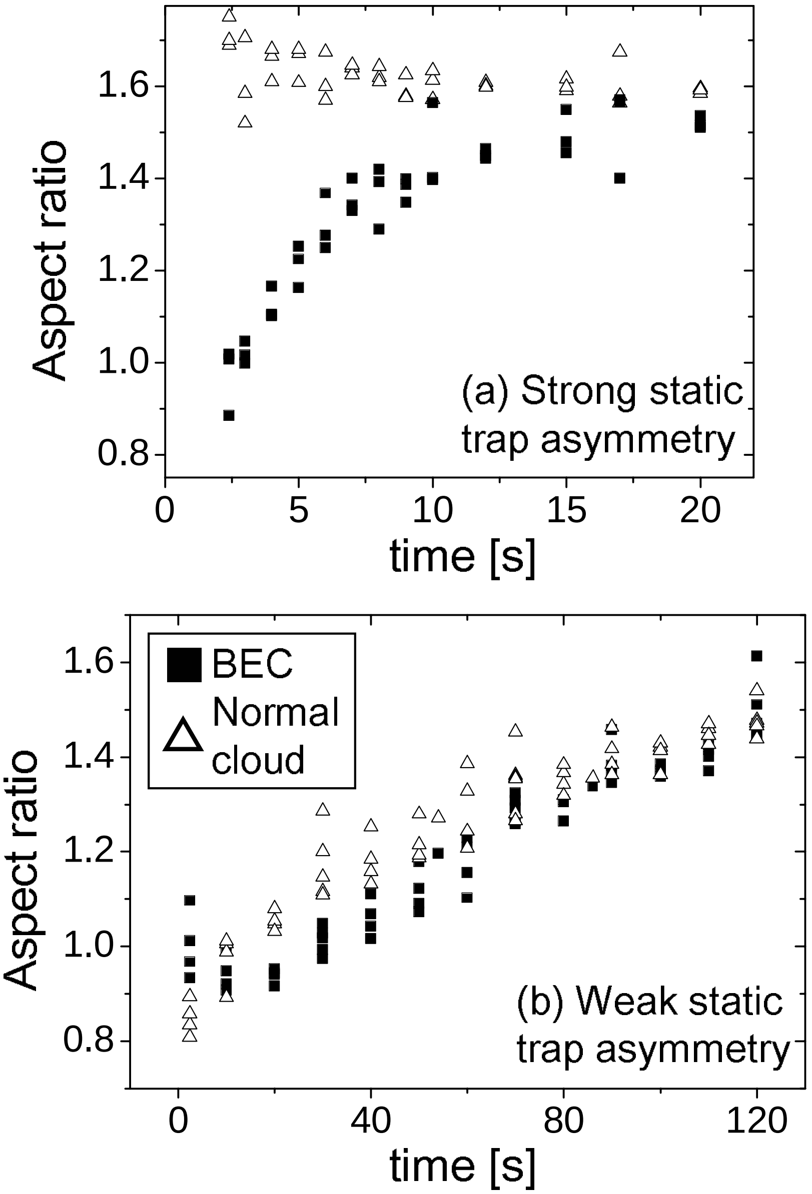

Figure 4.15: Rotational relaxation of an initially co-rotating condensate and normal component in an asymmetric confining potential. The simultaneously obtained aspect ratio is plotted for each of the components in the case of (a) a strong asymmetry and (b) a weak asymmetry applied at $t = 0$s. The aspect ratio allows a rigid-body rotation rate to be inferred through Eqn. 4.1. An aspect ratio of ~1.6 corresponds to a static cloud, while a lower value indicates more rotation. The initial stopping of the normal component is not included in graph (a); the data only begins after ~1-2s when the normal cloud's aspect ratio has already reached the static value.

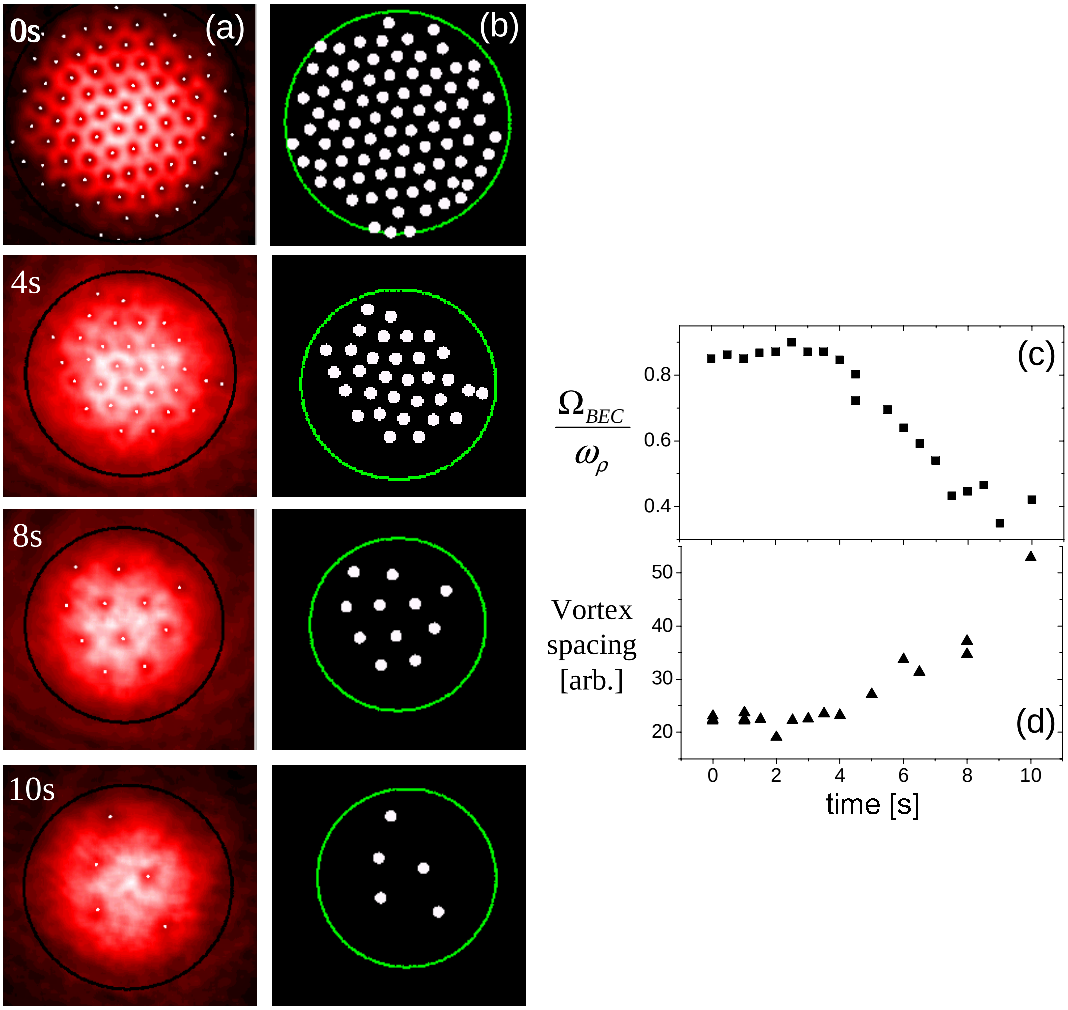

Figure 4.16: Rotational relaxation of a condensate from different perspectives. (a) Expansion images of the condensate at successively longer times after an asymmetry has been applied to the confining potential. (b) Vortex cores identified by an automated search algorithm. The large circle in both cases indicates the Thomas-Fermi radius of the condensate. (c) The rotation rate of the condensate as inferred from its aspect ratio. The aspect ratio is determined from a non-destructive image of the trapped sample before ballistic expansion. (d) The average vortex spacing as calculated from the expansion analysis in (b).

down: the loss of vortex number, the decrease in their density and the decrease in rotation rate as inferred from centrifugal distortion.

4.7 Spinning up even faster: large lattices and rotation

In the rotational decay experiments of the previous section, the application of a strong, static ellipticity to the confining potential was used to stop the rotation of the normal cloud. A closer inspection of the initial behaviour in this case revealed that the cloud had also been excited into damped, rotational scissors-mode oscillations [95, 119]. The behaviour of these oscillations is shown in figure 4.17 for a pure normal cloud above T_C. The torque from the applied static asymmetry brings the initially rotating gas to a stop with the density forming an elongated shape at $\sim 45°$ to the trap deformation [Figure 4.17(c)]. At this point, the angular momentum from the rotation has been stored as potential energy due to angular displacement. The motion then rebounds leading to the reverse rotation. This behaviour is reminiscent of the motion of a two-dimensional pendulum with slightly different frequencies of oscillation along two orthogonal directions. An equal superposition of pendulum motion in the two dimensions leads to a slow beating between circular and linear oscillation. By analogy, the period $\tau_s = 2\pi/\Delta\omega_\rho$ of the scissors mode depends on the asymmetry in the confining potential, $\Delta\omega_\rho \approx \epsilon\bar{\omega}_\rho$ for $\epsilon \ll 1$. Underdamped oscillations will only occur for an ellipticity larger than a critical value $\epsilon_C = 1/4\omega_\rho\tau$ [94] such that the time between atomic collisions τ is longer than the time τ_s for a single particle trajectory to feel the potential asymmetry.

The behaviour of the scissors mode suggested the idea of using it in the first stage of vortex nucleation to induce rotation in the normal gas. Before the evaporative cooling to quantum degeneracy, a step-wise sequence is used to excite the scissors mode in the normal cloud [Figure 4.18]. The excitation occurs in the same oblate configuration of the TOP potential as was used for stirring in section 4.2. The cloud is

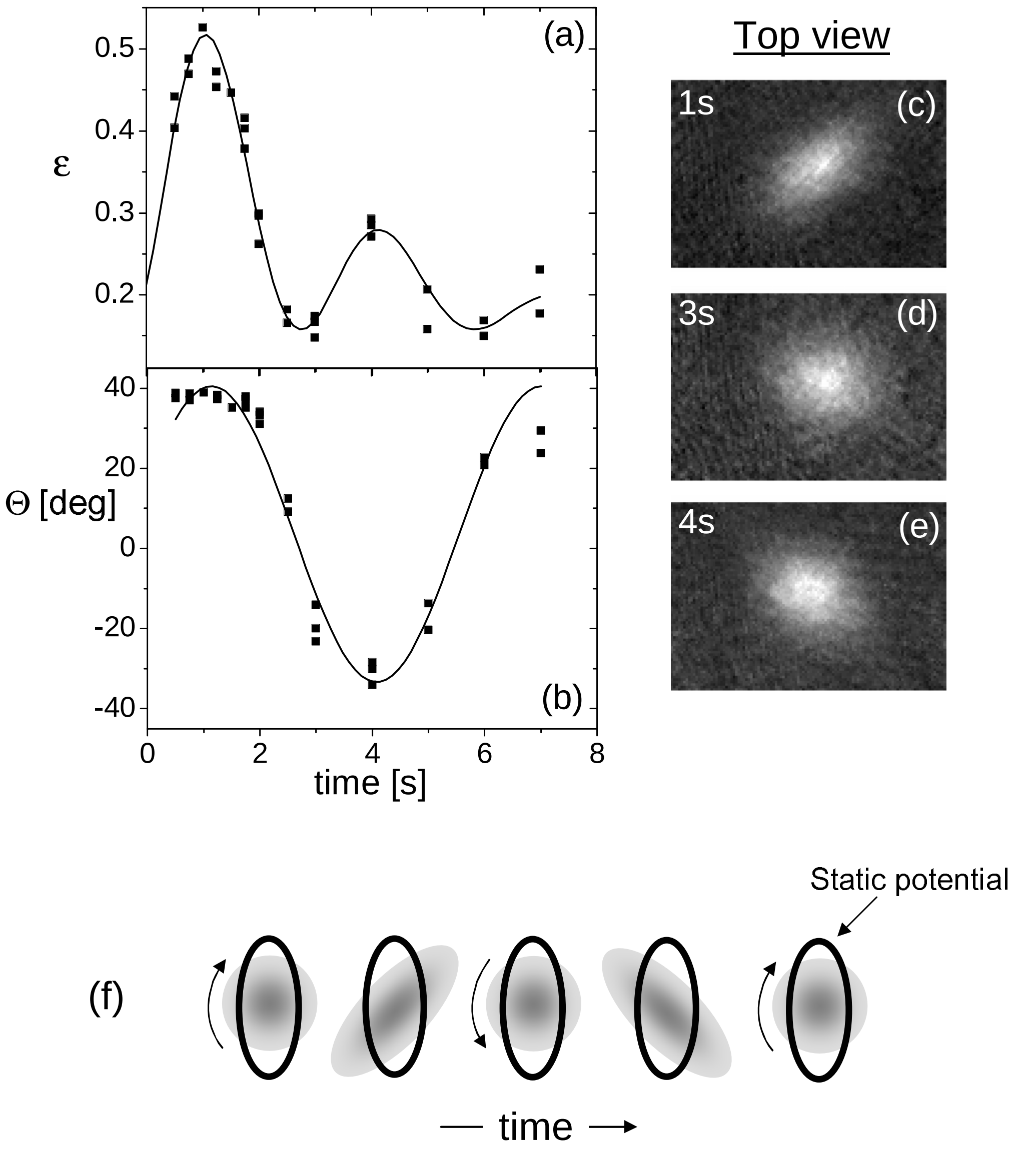

Figure 4.17: Rotational scissors mode of an initially rotating normal gas subjected to a sudden trap asymmetry. (a) Ellipticty ϵ of the cloud and (b) orientation θ of its major axis as a function of time. The damped sinusoidal fit to (a) and sinusoidal fit to (b) yield a scissors oscillation period of τ_s=5.7(8)s and τ_s=5.9(2)s, respectively. (c...e) A sampling of the in-trap images taken along the axis of scissors rotation and used to obtain graphs (b)&(c). Times indicated correspond to the horizontal axis of (b)&(c). (f) Sketch of one complete scissors cycle including the direction of fluid rotation. The elliptical line represents one contour of the asymmetric confining potential.

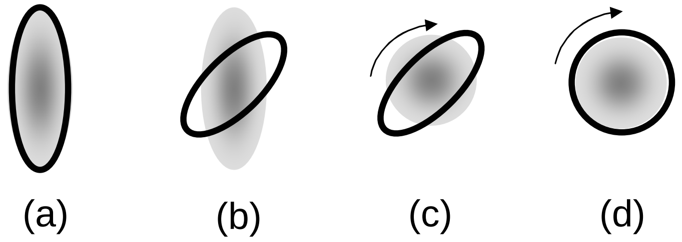

Figure 4.18: Stepwise excitation of the rotational scissors mode to impart angular momentum to a cold gas. (a) The gas is allowed to thermalize to an asymmetric TOP potential. (b) The orientation of the trap asymmetry is suddenly jumped by 45°. (c) After a quarter period of the scissors mode, the gas is maximally rotating. (d) The trap is quickly resymmetrized to preserve the angular momentum imparted to the gas.

first adiabatically deformed to an elliptical shape by changing the shape of the potential. An extra 2s (of the order of the rethermalization time) is allowed for the cloud to thoroughly equilibrate to the new trapping geometry. Subsequently, the orientation of the potential asymmetry is suddenly changed by 45° to excite the scissors mode. The strength of the trap asymmetry is also discontinuously changed at this point to a value $\epsilon_{mid} \approx 0.25$ independent of the initial conditions. After a short period of time, the potential is made symmetric and the evaporative spin-up is implemented as before. The excitation sequence generates the largest angular momentum, as assessed by the ultimate rotation of the condensate formed after evaporation, around an excitation time of $\tau \approx \tau_s/4 = 150$ms, as expected for $\epsilon = \epsilon_{mid}$ and $\bar{\omega}_\rho = 2\pi 6.8$Hz [2] . In a single particle model, the angular momentum imparted from the excitation depends on the initial shape of the cloud through $\sim \epsilon_i \langle x^2 + y^2 \rangle$. By controlling the initial trap deformity in the first stage of the excitation sequence, we can achieve good control over the angular momentum imparted to the normal cloud and, by extension, the vortex number generated in the condensate [Figure 4.19]. The maximum available trap ellipticity ($\epsilon_i \approx 0.41$) is used to obtain the most highly rotating condensates ($\Omega_{BEC}/\omega\rho \approx 0.95$) with the largest

---

[2] The step-wise drive excites both a rotational and irrotational scissors mode at a low and high frequency respectively. The irrotational component is ignored here since a simulation shows that the bulk of the angular momentum imparted to the gas is due the rotational component.

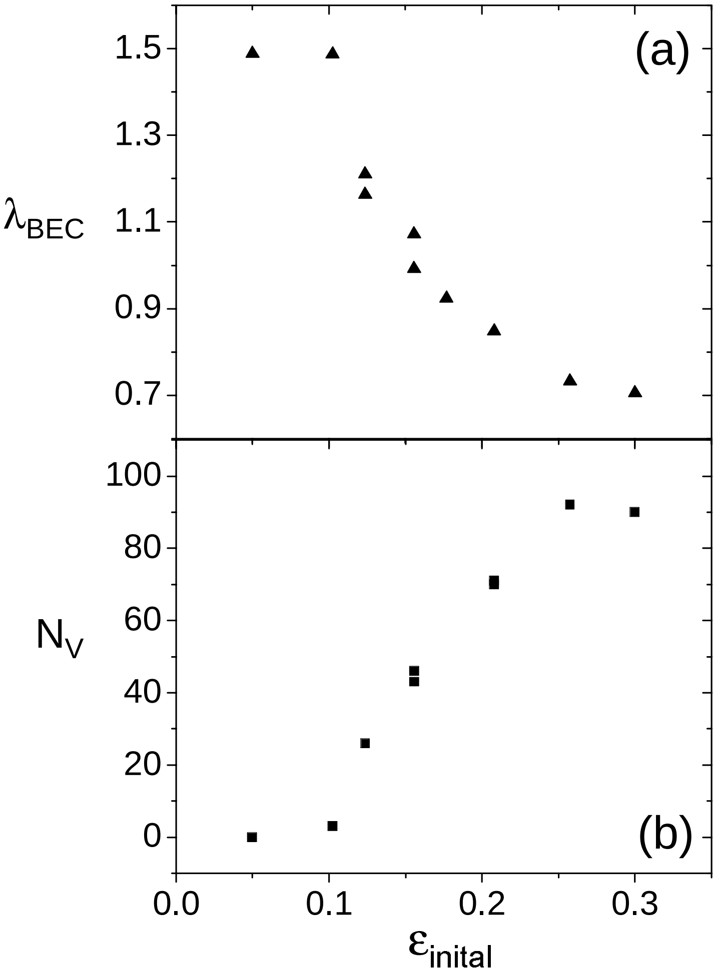

Figure 4.19: Dependence of (a) condensate aspect ratio (in other words rotation) and (b) vortex number on the initial ellipticity used in the scissors excitation.

vorticity ($N_V \approx 150$).

Perhaps the most significant feature of the scissors technique is that it allows the formation of highly rotating condensates with larger atom number than the original stirring technique. In the case of stirring, the normal cloud needs to start quite close in temperature to T_C, otherwise the evaporation cannot achieve condensation. The main issue is the amount of heating and center of mass motion ("slosh") induced by the 15s of stirring required to reach steady state rotation. Both processes worsen due to resonant effects as the trap is rotated at higher frequencies. In the case of the scissors technique, the rotation is induced rapidly over 150ms. Slosh is straight forward to minimize over the step-wise excitation sequence, leaving only the heating due to spurious shape excitations generated by the sudden trap changes. Therefore, it is not surprising that the evaporation is successful for initial clouds further from T_C. In fact, it is found beneficial to both final condensate number and rotation to start at a higher temperature initially, presumably because of the associated larger number of atoms present($17 \cdot 10^6$ versus $6 \cdot 10^6$ for the stirring case). A successful evaporation in terms of final rotation rate has always proven to be intimately tied with the performance in terms of condensate number.

The ability to reproducibly make highly rotating condensates with large numbers of vortices and large atom number makes an ideal starting point for a whole range of experiments, one of which is considered in the following section.

4.8 Nonequilibrium dynamics of large vortex lattices [77]

4.8.1 Abstract

We have studied the dynamics of large vortex lattices in a dilute-gas Bose-Einstein condensate. While undisturbed lattices have a regular triangular structure, large-amplitude quadrupolar shape oscillations of the condensate are shown to induce a wealth of nonequilibrium lattice dynamics. When exciting an m = -2 mode, we observe shifting of lattice planes, changes of lattice structure, and sheet-like structures in which individual vortices appear to have merged. Excitation of an m = +2 mode dissolves the regular lattice, leading to randomly arranged but still strictly parallel vortex lines.

4.8.2 Introduction

The experimental study of vorticity in a dilute-gas Bose-Einstein condensate (BEC) provides an useful perspective on superfluidity. While the focus of early work was on the study of single or few vortices [42, 118], recent advances in technique have made it possible to create BECs containing large amounts of vorticity [117, 48, 97, 103]. In a rapidly rotating BEC, a lattice of vortices is the lowest energy state in the rotating frame[59]. Experimental studies of lattices to date have concentrated on formation and decay processes [118, 117, 48, 97, 103, 138, 47]. In this section we study the nonequilibrium behavior of vortex lattices under large-amplitude, anisotropic strain.

4.8.3 Experimental technique

For creating large amounts of vorticity in condensates, we use a modified version of the spin-up technique described in our previous paper [97]. The starting point is a magnetically trapped cloud of 17×10^6 ^{87}Rb atoms in the $|F = 1, m_F = -1\rangle$ state with a temperature approximately three times above the critical temperature for the BEC phase transition, $T_c = 67$ nK. By manipulating the ellipticity of the confining potential, we can resonantly pump angular momentum into the as yet uncondensed cloud [43]. We then tune the trapping potential to near perfect axial symmetry with trap frequencies $\{\omega_\rho, \omega_z\} = 2\pi\{8.35, 5.45\}$Hz. In this round trap the cloud continues to rotate, and by performing a nearly one-dimensional evaporation along the axis of rotation (z-axis) as described in Ref. [97], we cool down and further spin up the cloud until a highly rotating condensate is born out of the rotating normal cloud. For the experiments described in this paper, the evaporation is continued to a point where little or no thermal fraction remains. As a result of this procedure, we obtain highly rotating condensates with typically 1×10^6 atoms and a Thomas-Fermi radius of $R_\rho = 51\mu m$, $R_z = 26\mu m$, containing 130 vortices or more.

To study these condensates we can image along the x, y, or z directions. When the condensate is held in the trap, the core size of the vortices is close to the resolution limit of our optical detection system so that individual vortices are not resolved by in-trap imaging. However, by nondestructively imaging a trapped condensate from the side (along the x-direction) and measuring its aspect ratio, the rotation rate of the condensate can be determined [97, 138]. For our highly rotating condensates we determine typical aspect ratios of 0.5, which is markedly different from the static aspect ratio of the magnetic trap, 1.53, because of centrifugal forces. Typical condensate rotation rates of $0.95\omega_\rho$ are inferred.

To resolve individual vortices, we can release a condensate from the trap and image it 50 ms later after it has expanded by a factor of 5 [118, 51]. Such expansion pictures taken along the z-direction reveal a triangular lattice of vortex cores in highly rotating condensates [Fig. 4.20(a)]. The lattice structure is remarkably regular even at the outer regions of the condensate, and is observed with very good contrast as shown by the cross section in Fig. 4.20(b).

When looking at such vortex lattices in expansion from the side (i.e., along the x or y direction), good contrast is only obtained if the lattice is oriented in such a way that vortices line up behind each other along the direction of view, or in other words when the direction of view is parallel to lattice planes. The vortex lattices are not stationary in the lab frame, but are rotating with the condensate, and furthermore the initial orientation of the lattice in the xy plane cannot be controlled in current experiments. Therefore the times when vortices line up along the direction of sight are unpredictable, and images revealing lattice planes are only obtained in a random subset of all trials.

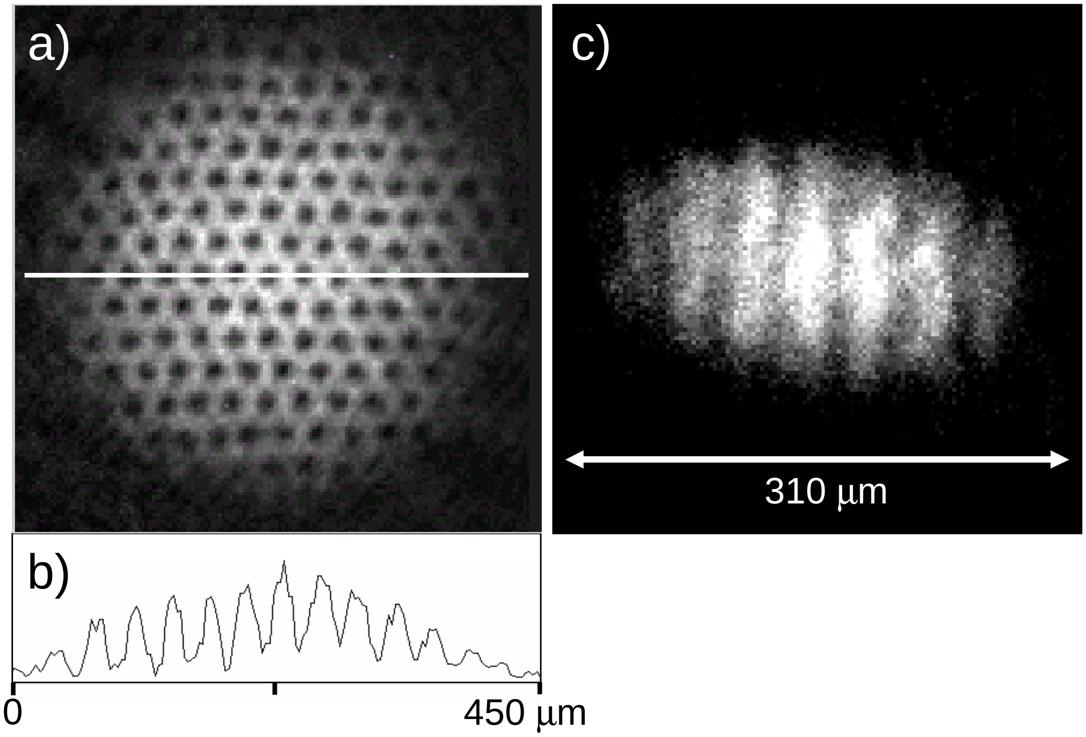

Figure 4.20: (a) Expansion picture of a vortex lattice seen along the rotation axis. (b) One pixel wide cross section along the white line in (a). (c) Expansion picture of a different condensate rotating at $0.75\omega_\rho$, i.e. more slowly than in (a), seen from the side.

One example is shown in Fig. 4.20(c), where the vortex planes are clearly visible as dark vertical lines. These images are direct verifications of the theoretical prediction that vortex lines are only marginally bent for our experimental parameters [89, 79], as is also confirmed by the good contrast seen in the topview picture of Fig. 4.20(a).

Vortex lattices such as the one shown in Fig. 4.20 are the starting point for our studies of the effects of dynamically generated strain. We apply the distortion by resonantly driving quadrupolar shape modes in the vortex-filled condensate [61, 98]. In the large-amplitude limit, the $m_z = +2$ and $m_z = -2$ modes distort the circular cross-section of the condensate into an ellipse and cause the major axis of the ellipse to rotate along with, or against, the sense of the condensate rotation, respectively. The generated strain is considerable – the ratio of major to minor axis of the condensate can be larger than three to one. The frequencies of the $m_z = \pm 2$ modes may be calculated using the sum rule argument given by Refs.[161, 44]. Our condensates are rotating typically at $0.95\omega_\rho$, just 5% under the centrifugal limit. At the centrifugal limit, the $m_z = +2$ ellipse is fixed in the rotating condensate frame, and the $m_z = -2$ shape is fixed in the lab frame. At our rotation rate of $0.95\omega_\rho$, the distortion, as seen in the frame of the lattice, rotates at only 0.4 Hz for the $m_z = +2$ mode, compared with 8.34 Hz for the $m_z = -2$ mode. For this reason, we expect very different resulting lattice dynamics in the presence of either of the two modes. We emphasize as well that the two different modes result in very different fluid-flow patterns. In the centrifugal limit, the $m_z = +2$ mode very closely approximates rigid-body rotation, while much of the $m_z = -2$ velocity field is provided by an irrotational, quadrupole flow pattern. This distinction may provide a parallel explanation for the correspondingly distinct observed effects [see Section 4.9].

4.8.4 Lattice dynamics in the presence of an $m_z = -2$ surface mode

Because the $m_z = -2$ mode is almost stationary in the lab frame for the parameters of our experiment, this mode can be excited conveniently and nearly resonantly by a static trap deformation. Indeed we observe that by jumping from the round trap described above to a trap that has the same mean horizontal frequency, but a horizontal ellipticity of 3.6% [45], the ellipticity of the condensate increases over a time scale of 300 ms from approximately 0 to 40%, thereby exceeding the trap ellipticity by more than an order of magnitude. Since the vortex lattice is rotating quickly with respect to this almost static deformation, it is an interesting and nontrivial question to ask whether or not a lattice structure is maintained, and, if so, how it rearranges in the presence of the excitation.

Experimentally, vortex lattices can indeed be observed in expansion images up to 400 ms after the start of the continuously applied trap deformation (Fig. 4.21).

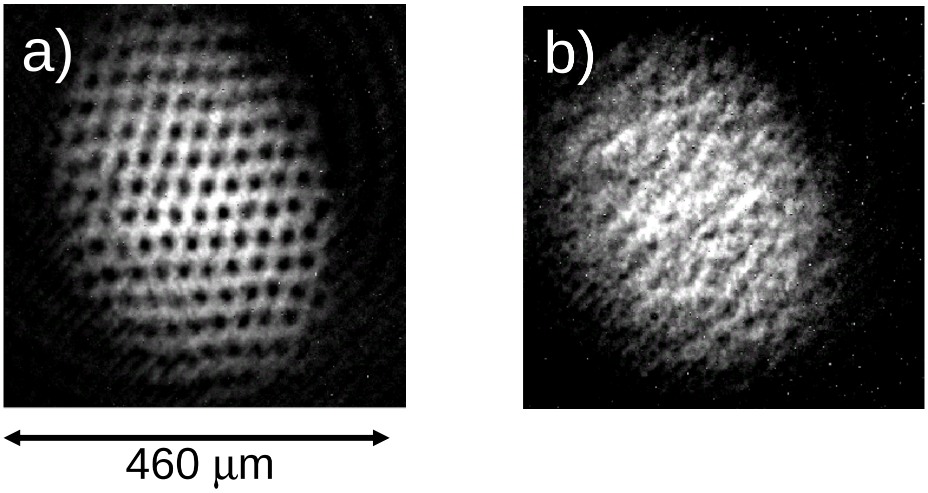

Figure 4.21: Evolution of the lattice and condensate density profile after (a) 173 ms and (b) 873 ms in the presence of an $m_z = -2$ excitation. Pictures taken along axis of rotation.

Subsequently, long range order is lost and vortex visibility becomes low, presumably due to tilting [98] or bending of the vortex lines [48]. A closer look at the first 400 ms of this evolution reveals a wealth of intriguing vortex dynamics. As the vortex lattice rotates in the deformed condensate, the lattice planes must continuously shift relative to each other to accommodate to the elliptical shape of the condensate. One consequence of this is transient changes of the lattice structure. In Fig. 4.22 the lattice has changed from the triangular structure of an undisturbed lattice to a near rectangular structure.

The most striking observation, however, is of condensates containing sheet-like structures rather than individual vortex cores, as shown in Fig. 4.23(a). We interpret these sheets as rows of vorticity along which individual vortex cores have essentially merged. Given the near perfect contrast of these sheets, as shown by the cross section in Fig. 4.23(b), we can exclude the possibility that the sheets are merely formed by a collective tilting of vortices along a lattice plane, which would result in an intermediate contrast. Similarly, we can rule out that this is an effect merely of imaging resolution - had the vortices retained their original structure but come so close together that we

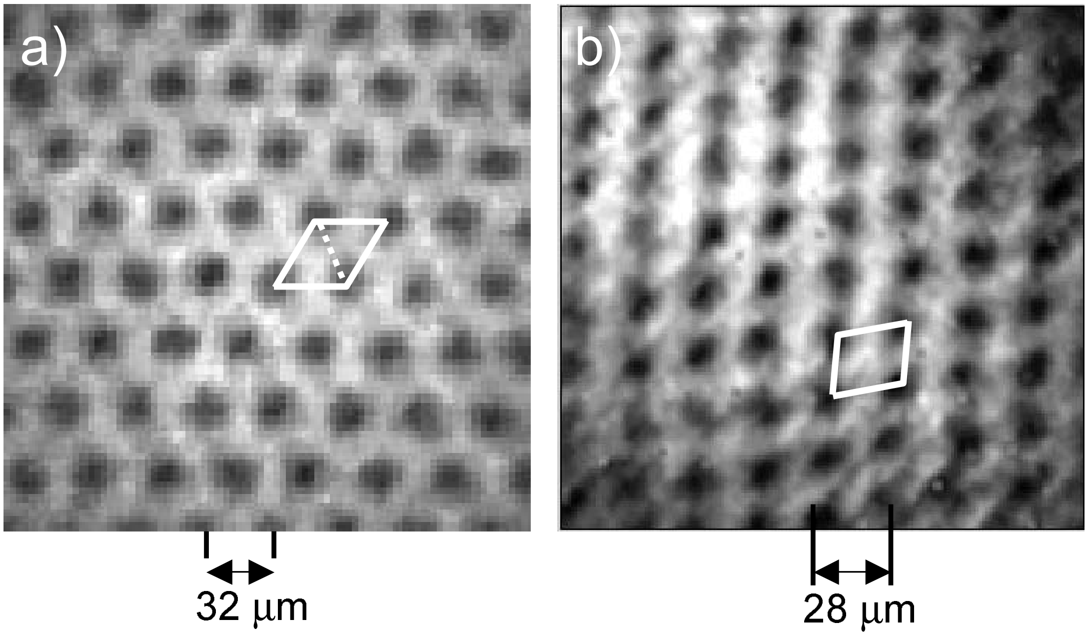

Figure 4.22: Change of lattice structure seen along rotation axis. (a) Triangular structure in an undisturbed lattice. (b) Near rectangular structure seen transiently during lattice evolution after 273 ms in the presence of an $m_z = -2$ quadrupolar surface mode.

could not spatially resolve them, we again would see white stripes set off by grey troughs, rather than the near 100% alternating stripes of white and black. If there continue to exist wispy fingers of condensate that cross the stripes and differentiate individual vortices, they must be very tenuous indeed to be consistent with the observed contrast. The clouds have been continuously distorted from their original hexagonal symmetry, so the observation of 16 stripes along the major axis of the BEC in Fig. 4.23(a) tells us that there must also be the equivalent of 16 units of vorticity along the length of the stripes through the center of the cloud. By measuring the in-trap height of the condensate, the ellipticity in the xy-plane and the number of atoms, we can infer the ratio of unit vorticity spacing (along the minor axis) to healing length (given by $\frac{1}{\sqrt{8\pi na}}$, where n is the mean density and a the scattering length) to be on the order of 5.

In fact the contrast of this sheet-like phase is so deep that the structure can be detected by looking at condensates *in trap* (along the x or z direction), even though the structure is close to our optical resolution limit. By taking a time series of ten nondestructive images of a single condensate along the x direction, we see that the sheet structure appears and disappears periodically with a period of about 21.2 ms for a condensate rotating at a frequency of $0.95\omega_\rho$ [Fig. 4.24].

This periodicity can be understood as follows: The sheet structure forms when a lattice vector lies along a minor axis of the cloud, presumably since this is when the vortices are closest together. As that vector rotates past the minor axis, structure along the vector is reestablished, the two-dimensional (2D) pattern of individual vortices reemerges, and the high-contrast stripes disappear from the in-trap images. A lattice vector aligns with the minor axis six times per lattice rotation period due to the sixfold symmetry of the unperturbed lattice, consistent with the observed frequency of periodic stripe formation. This interpretation is bolstered by the expansion images, which show high contrast sheets when a lattice vector lies close to the minor axis, but 2D lattices (albeit distorted) for other orientations. We find it remarkable that this lattice-to-sheet-

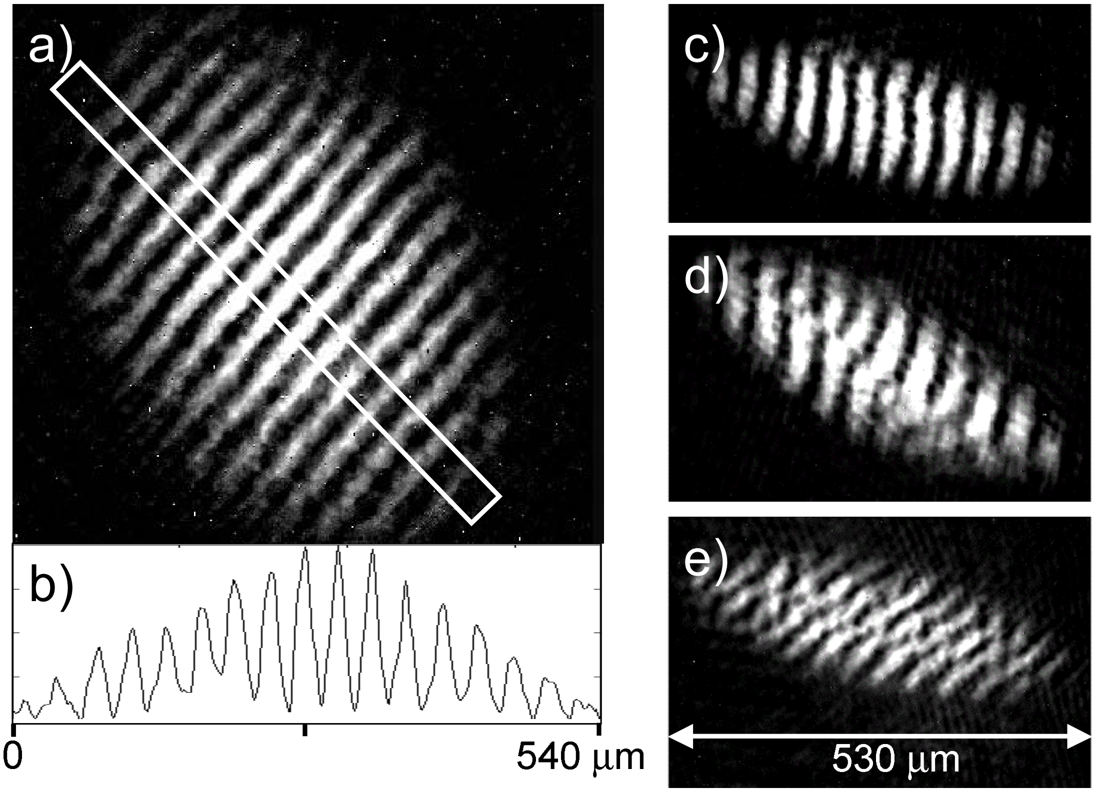

Figure 4.23: (a) Sheet-like structure seen after 173 ms in the presence of an $m_z = -2$ quadrupolar surface mode. (b) Cross section integrated over the white box in (a). Even though the box is wider than the calculated vortex core spacing, the observed contrast is nearly perfect. (c-e) Same as (a), but observed within the first tens of ms in a more deformed trap with $\{\omega_{x,y,z}\} = 2\pi\{6.0, 8.6, 13.8\}$Hz. All pictures taken along axis of rotation.

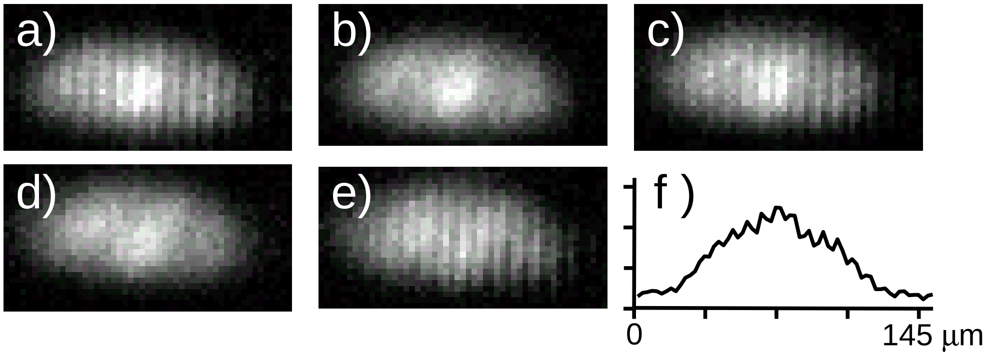

Figure 4.24: (a-e) Nondestructive in-trap images of the sheet-like structures seen along the x-direction [conditions similar to Fig. 4.23(a)]. Spacing between images 10.6 ms. Note the very different spatial scale from expansion images (e.g., Fig. 4.20). (f) Cross section of (a), integrated over the condensate.

to-lattice sequence persists through multiple cycles before long range order and visibility are compromised.

Using a trap with a stronger distortion of 34% as in Fig. 4.23(c-e), we also observe sheets breaking apart in the center. In Fig. 4.23(c), the density distribution along the lattice vector that we see near-parallel with the minor axis is nearly featureless. Figure 4.23(d,e) hint at the succeeding lattice evolution: Fig. 4.23(d) represents a small rotation from Fig. 4.23(c), and we see that the sheets have begun to reconnect across the cloud. Figure 4.23(e) appears to be a continuation of that process, with considerable evidence of uniformity in the repeating structure.

4.8.5 Lattice dynamics in the presence of an $m_z = +2$ surface mode

We excite the $m_z = +2$ mode by elliptically deforming the magnetic trap and rotating that ellipse around in the xy plane. When the $m_z = +2$ mode is driven approximately 1 Hz away from its resonance, the ellipticity of the condensate increases from 0 to 50% over a timescale of 250 msec. Under the influence of an on-resonant drive, the ellipticity increases continuously, even passing beyond 90% after 700 msec

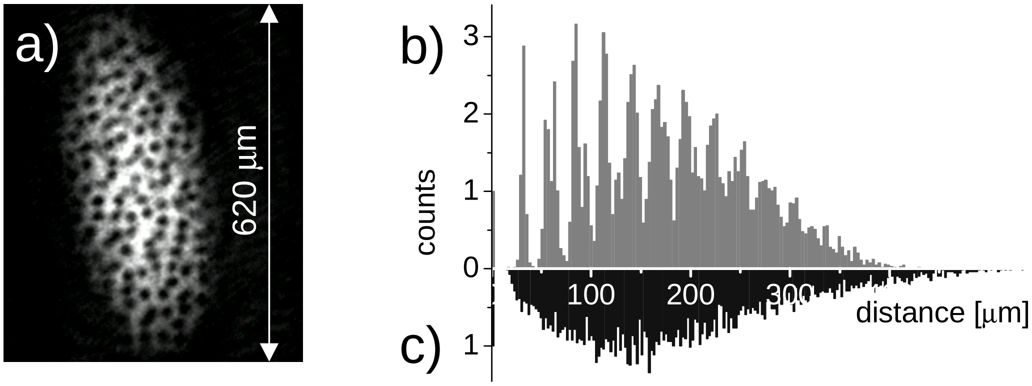

Figure 4.25: (a) Irregular assembly of vortex cores as observed along rotation axis after 500 ms in the presence of an $m_z = +2$ quadrupolar surface mode. (b) Histogram of distances between each pair of vortices in the regular triangular lattice shown in Fig. 4.20a. The visibility of separate peaks reveals the high degree of long-range order. (c) Same as (b) but calculated for the BEC of Fig. 4.25a. Peaks are barely visible here, meaning that the lattice has almost reached a random disorder.

and approaching 100% [46]. As discussed above, the distortion rotates only very slowly with respect to the lattice, and thus we expect it to be correspondingly "gentle" with respect to its action on the lattice.

Indeed, as we show in Fig. 4.25(a), we do not see the lattices squeezed into sheets for the $m_z = +2$ mode. Instead we observe a gradual increase of disorder in the lattice. 400 msec after we start driving the excitation on resonance, we see a complete loss of long-range order in the vortex structure. The imaging contrast of individual vortices remains high, so we know they remain parallel to the line of sight (in contrast for instance to the case of Fig. 4.21), but otherwise they appear to have liquified (see the correlation histogram of Fig. 4.25). This behavior confirms our expectation of the $m_z = +2$ mode being a gentler disturbance for the lattice than the $m_z = -2$ mode.

4.8.6 Conclusions

In conclusion we have succeeded in observing a wealth of nonequilibrium vortex lattice dynamics in a BEC under anisotropic compression. Key observations include the

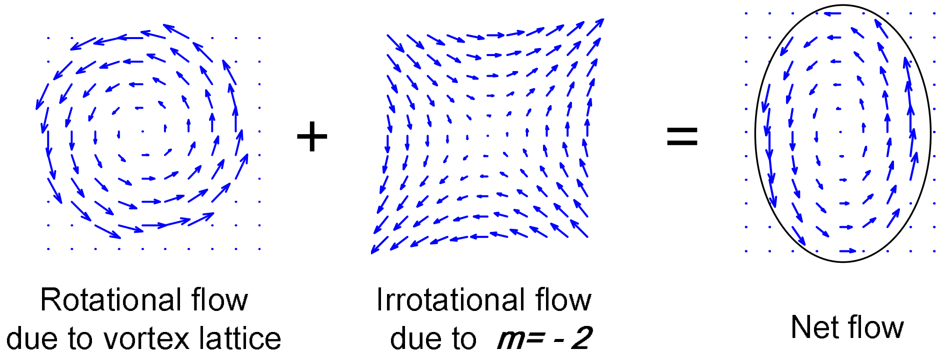

Figure 4.26: Macroscopic velocity field of a rotating condensate in the presence of a counter-propagating $m = -2$ surface wave. The net flow induces lattice shear along the major axis of the quadrupolar deformation.

shifting of lattice planes relative to each other, leading to transient changes of the lattice structure, the formation of an unexpected and very pronounced sheet structure, and finally, a gradual transition from an ordered lattice to a rather liquid-like arrangement in which vortex cores remain visible, but their relative positions are irregular. The observed sheet structure is of particular interest: at present the behavior of densely packed vortex lattices is in the center of theoretical discussions about vortices [101, 63, 86, 133]. While most of these theoretical discussions propose to enter this regime by having high rotation rates almost inaccessible to experiment or inconveniently low atom numbers in the condensate, this section demonstrates an alternative and unexpected way of bringing vortices close together. We hope that the results presented here will stimulate further theoretical discussions in the field of vortex lattices.

4.9 Theory responds

Following the publication of the experimental results from the previous section, several theory groups [127, 66, 91] have investigated the origin of the dynamical distortions of the lattice structure in the presence of the counter-propagating $m = -2$ mode. Although using different approaches, both Mueller and Ho [127] and Cozzini and Stringari [66] reproduce the transient orthorhombic lattice structure as well as the periodic appearance of sheet structures aligned with the short axis of the quadrupolar deformation. Both theoretical approaches confirm that the irrotational flow pattern of the quadrupolar mode applies a shear to the lattice and thus drives the rearrangement of the vortices [Figure 4.26]. Furthermore, it is interesting to note in this context that the velocity field describing the sheet-like phase of the condensate really *requires* the presence of a quadrupolar flow field [Figure 4.27].

Finally, on a macroscopic level, both refs. [127] and [66] predict the time evolution of the amplitude and orientation of the $m = -2$ deformation in the presence of a constant applied trap asymmetry. The predicted behaviour is qualitatively seen in the experiment and has already been briefly described in section 4.8. A direct quantitative comparison between experiment and theory will be forthcoming in the future [67].

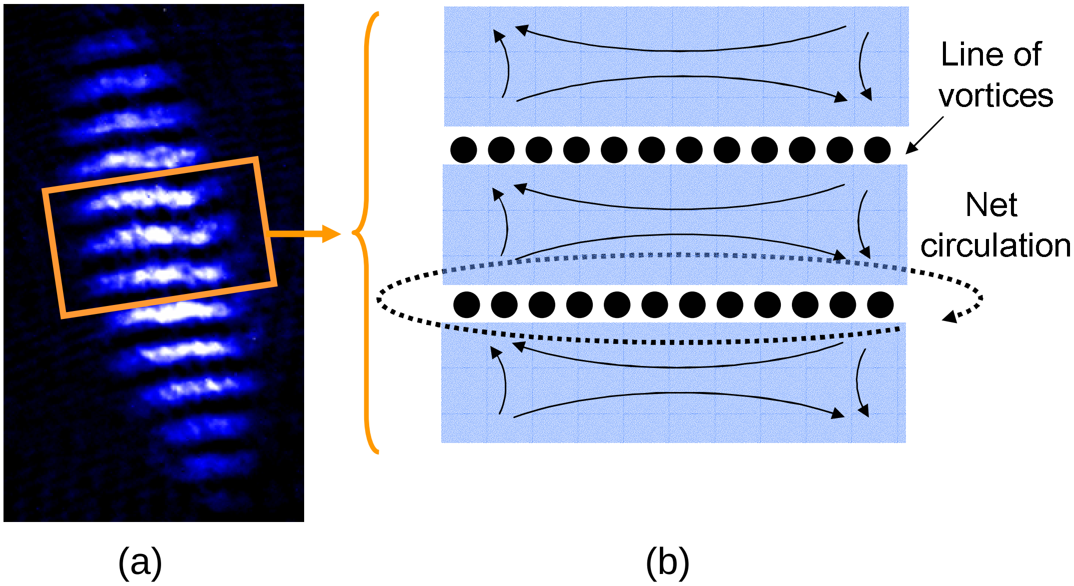

Figure 4.27: (a)Expanded condensate density profile at the time when stripes of vorticity form aligned with the minor axis of the $m = -2$ deformation. (b) Inferred microscopic velocity field in the region of the two central stripes of vorticity surrounded by three regions of condensate fluid. Note the circulation about each stripe of vorticity composed of a row of > 10 vortex cores. The irrotational flow pattern characteristic of a quadrupolar mode is required in the regions of condensate density to knit the vortex stripes together with a continuous velocity field.

Bibliography

[1] H. Traeuble and U. Essmann, J. Appl. Phys. **25**, 273 (1968); N. V. Sarma, Philos. Mag. 17, 1233 (1968); H. F. Hess *et al.*, Phys. Rev. Lett. **62**, 214216 (1989).

[2] F. Zernike, in Nobel Lectures, Physics (Elsevier, Amsterdam,1964), p.239, text of 1953 Nobel Prize lecture.

[3] Atomic, Molecular, & Optical Physics Handbook, ed. Gordon W. F. Drake, American Institute of Physics 1996.

[4] P. Schwindt, private communication.

[5] D.M. Harber, H.J. Lewandowski, J.M. McGuirk and E.A. Cornell, cond-mat/9912308.

[6] D. A. Butts and D. S. Rokhsar, Nature **397**, 327 (1999); H. Pu, C. K. Law, J. H. Eberly, and N. P. Bigelow, Phys. Rev. A **59**, 1533 (1999); T. Isoshima and K. Machida, Phys. Rev. A **59**, 2203 (1999); J. J. García-Ripoll and V. M. Pérez-García, Phys. Rev. A **60**, 4864 (1999).

[7] The core-filling material is removed slowly enough (100 ms) that the vortex core has time to shrink adiabatically to its final bare size, but rapidly enough that the initial location of the bare core is well correlated with the location of the original filled core.

[8] We use phase-contrast imaging for both the in-trap and expansion images to simplify imaging procedures. When imaging the expanded atom cloud, we obtain good signal when the probe is detuned 3 linewidths from resonance.

[9] Because of our low trapping frequencies (7.8 Hz), expansions are correspondingly slow. We get larger final spatial distributions by giving the atoms a 6-ms preliminary “squeeze”at high spring constant, followed by a 50-ms expansion period.

[10] Tin-Lun Ho and V. B. Shenoy, Phys. Rev. Lett. **77**, 3276 (1996); D. S. Hall *et. al.*, Phys. Rev. Lett. **81**, 1539 (1998).

[11] G. B. Hess, Phys. Rev. **161**, 189 (1967).

[12] Our measurements were performed at temperatures of $T = 23(6)$nK, and relative temperatures of $T/T_c = 0.8(1)$, where T_c is the BEC critical temperature. Temperatures were measured using fits to trapped bare vortices where the core was not resolvable.

[13] P. C. Haljan, B. P. Anderson, C. E. Wieman, and E. A. Cornell, abstract QPD1, Quantum Electronics and Laser Science Conference 2000, San Francisco, May 2000.

[14] The vortex is formed in the $|F = 1, m_F = -1\rangle$ hyperfine state.

[15] S. Sinha, Phys. Rev. A **55**, 4325 (1997); R. J. Dodd, K. Burnett, M. Edwards, and C. W. Clark, Phys. Rev. A **56**, 587 (1997); A. A. Svidzinsky and A. L. Fetter, Phys. Rev. A **58**, 3168 (1998); F. Zambelli and S. Stringari, Phys. Rev. Lett. **81**, 1754 (1998).

[16] A 10% tightening of the spherical trap is achieved by turning off the component of the rotating TOP bias field along the direction of the imaging axis. This leaves an oscillating bias field perpendicular to the line of sight. The BEC equilibrium position is sagged so far vertically that the oscillating quadrupole zero of the squeezed TOP trap does not pass through the cloud.

[17] The confining potential is squeezed over 200 ms, slow enough to prevent large-amplitude shape oscillations of the BEC but fast enough so as not to interfere significantly with the tilting dynamics.

[18] D. S. Rokhsar, Phys. Rev. Lett. **79**, 2164 (1997); P. O. Fedichev and G. V. Shlyapnikov, Phys. Rev. A **60**, R1779 (1999); A. A. Svidzinsky and A. L. Fetter, Phys. Rev. Lett. **84**, 5919 (2000).

[19] F. Zambelli and S. Strigari, private communication.

[20] See for example, P. G. Drazin and R. S. Johnson, *Solitons: an Introduction* (Cambridge University Press, Cambridge, 1989).

[21] S. Burger *et al.*, Phys. Rev. Lett. **83**, 5198 (1999); J. Denschlag *et al.*, Science **287**, 97 (2000).

[22] See for example the review article by Y. S. Kivshar and B. Luther-Davies, Phys. Rep. **298**, 82 (1998).

[23] V. Tikhonenko *et al.*, Opt. Lett. **21**, 1129 (1996); A. V. Mamaev, M. Saffman, and A. A. Zozulya, Phys. Rev. Lett. **76**, 2262 (1996); A. V. Mamaev *et al.*, Phys. Rev. A **54**, 870 (1996).

[24] A. E. Muryshev, H. B. van Linden van den Heuvell, and G. V. Shlyapnikov, Phys. Rev. A **60**, R2665 (1999); P. O. Fedichev, A. E. Muryshev, and G. V. Shlyapnikov, Phys. Rev. A **60**, 3220 (1999).

[25] Th. Busch and J. R. Anglin, cond-mat/0012354.

[26] The spatial width of a bare dark soliton or vortex sample is on the order of the BEC healing condensates.

[27] Condensates expand slowly when released from our weak trap. We get larger final spatial distributions by giving the atoms a 6-ms preliminary “squeeze” at high spring constants, followed by a 50-ms expansion period. Dynamical soliton

evolution and decay begins during the $|2\rangle$ removal, and continues through about the first few milliseconds of expansion; thereafter, the decay pattern is essentially frozen into the expanding sample.

[28] A. E. Leanhardt, cond-mat/0206303.

[29] V. K. Tkachenko, Zh. Eksp. Teor. Fiz. **50**, 1573 (1966) [Sov. Phys. JETP **23**, 1049 (1966)]; E. J. Yarmchuk, M. J. V. Gordon, and R. E. Packard, Phys. Rev. Lett. **43**, 214 (1979).

[30] V. M. H Ruutu, U. Parts, J. H. Koivuniemi, N. B. Kopnin, and M. Krusius, JLTP **107**, 93 (1997).

[31] J. S. Langer and M. E. Fisher, Phys. Rev. Lett. **19**, 560 (1967); S. V. Iordanskii, Zh. Exsp. Theor. Fiz. **48**, 708 (1965) [Sov. Phys. JETP **21**, 467 (1965).].

[32] E. Varoquaux, M. W. Meisel, and O. Avenel, Phys. Rev. Lett. **57**, 229 (1986); J.C. Davis *et al.*, Phys. Rev. Lett. **69**, 323 (1992).

[33] M. R. Matthews *et al.*, Phys. Rev. Lett. **83**, 2498 (1999); B. P. Anderson, P. C. Haljan, C. E. Wieman, and E. A. Cornell, Phys. Rev. Lett. **85**, 2857 (2000).

[34] C. Raman *et al.*, cond-mat/0106235.

[35] Small static trap asymmetries can have a disproportionately large effect compared to much larger rotating asymmetries. This is related to the fact (pointed out by Guery-Odelin [94]) that spin-up and spin-down times are very different for a given ($m = 2$) trap asymmetry.

[36] In L.He. experiments, one expects very different behavior if one either (i) cools below T_c before crossing the threshold rotation for vortex nucleation or (ii) vice versa. In our experiment, the harmonic "pot" means that case (i) applies: the new-born condensate is initially too small to support a vortex.

[37] D. V. Osborne, Proc. Phys. Soc. (London) **A63**, 909 (1950); R. Meservey, Phys. Rev. **133**, A1472 (1964).

[38] S. Stringari, private communication.

[39] S. Sinha, Phys. Rev. A **55**, 4325 (1997); R. J. Dodd, K. Burnett, M. Edwards, and C. W. Clark, Phys. Rev. A **56**, 587 (1997); A. A. Svidzinsky and A. L. Fetter, Phys. Rev. A **58**, 3168 (1998).

[40] D. L. Feder and C. W. Clark, unpublished.

[41] S. Sinha, Phys. Rev. A **55**, 4235 (1997), E. Lundh. C. J. Pethick, and H. Smith, Phys. Rev. A **55**, 2126 (1997), Y. Castin and R. Dum, Eur. Phys. J. D **7**, 399 (1999).

[42] M. R. Matthews *et al.*, Phys. Rev. Lett. **83**, 2498 (1999); B. P. Anderson, P. C. Haljan, C. E. Wieman, and E. A. Cornell, Phys. Rev. Lett. **85**, 2857 (2000).

[43] We impart angular momentum to the noncondensed cloud by stepwise driving a quarter cycle of a scissors mode [119].

[44] S. Stringari, private communication. For an alternative approach, see also A. A. Svidzinsky and A. L. Fetter, Phys. Rev. A **58**, 3168 (1998).

[45] We define ellipticity as $\frac{\omega_x^2-\omega_y^2}{\omega_x^2+\omega_y^2}$ with ω_x and ω_y being the trap frequency along the minor and major axes of the ellipse, repectively.

[46] For related work on the evolution of the ellipticity see also P. Rosenbusch *et al.*, Phys. Rev. Lett. **88**, 250403 (2002).

[47] J. R. Abo-Shaeer, C. Raman, and W. Ketterle. Formation and decay of vortex lattices in Bose-Einstein condensates at finite temperatures. Phys. Rev. Lett., 88:070409, February 2002.

[48] J. R. Abo-Shaeer, C. Raman, J. M. Vogels, and W. Ketterle. Observation of vortex lattices in Bose-Einstein condensates. Science, 292:476, March 2001.

[49] L. Allen and J. H. Eberly. Optical Resonance and Two-level Atoms. Dover, 1987.

[50] B.P. Anderson, P.C. Haljan, C.A. Regal, D.L. Feder, L.A. Collins, C.W. Clark, and E.A. Cornell. Watching dark solitons decay into vortex rings in a Bose-Einstein condensate. Phys. Rev. Lett., 86(14):2926, April 2001.

[51] B.P. Anderson, P.C. Haljan, C.E. Wieman, and E.A. Cornell. Vortex precession in Bose-Einstein condensates: Observations with filled and empty cores. Phys. Rev. Lett., 85(14):2857, October 2000.

[52] M.R. Andrews, M.-O. Mewes, N.J. van Druten, D.S. Durfee, D.M. Kurn, and W. Ketterle. Direct, nondestructive observation of a Bose condensate. Science, 273(0):84, July 1996.

[53] J. R. Anglin. Local vortex generation and the surface mode spectrum of large Bose-Einstein condensates. Phys. Rev. Lett., 87:240401, December 2001.

[54] J.R. Anglin and M. Crescimanno. condmat/0210063.

[55] Eric L. Bolda, Sze M. Tan, and Dan F. Walls. Measuring the quantum state of a Bose-Einstein condensate. Phys. Rev. A, 57(6):4686, June 1998.

[56] Satyendra Bose. Plancks Gesetz und Lichtquantenhypothese. Z. Phys., 26(3):178, 1924.

[57] P. Bouyer and M.A. Kasevich. Heisenberg-limited spectroscopy with degenerate Bose-Einstein gases. Phys. Rev. A, 56(2):R1083, August 1997.

[58] S. Burger, K. Bongs, S. Dettmer, W. Ertmer, K. Sengstock, A. Sanpera, G.V. Shlyapnikov, and M. Lewenstein. Dark solitons in Bose-Einstein condensates. Phys. Rev. Lett., 83(25):5198, December 1999.

[59] D.A. Butts and D.S. Rokhsar. Predicted signatures of rotating Bose-Einstein condensates. Nature, 397(6717):327, January 1999.

[60] Lincoln D. Carr, Mary Ann Leung, and William P. Reinhardt. Dynamics of the Bose-Einstein condensate: quasi-one-dimension and beyond. J. Phys. B, 33:3983, 2000.

[61] F. Chevy, K.W. Madison, and J. Dalibard. Measurement of the angular momentum of a rotating Bose-Einstein condensate. Phys. Rev. Lett., 85(11):2223, September 2000.

[62] N. R. Claussen, E. A. Donley, S. T. Thompson, and C. E. Wieman. Microscopic dynamics in a strongly interacting Bose-Einstein condensate. Phys. Rev. Lett., 89:010401, July 2002.

[63] N. R. Cooper, N. K. Wilkin, and J. M. F. Gunn. Quantum phases of vortices in rotating Bose-Einstein condensates. Phys. Rev. Lett., 87:120405, September 2001.

[64] E.A. Cornell, D.S. Hall, M.R. Matthews, and C.E. Wieman. Having it both ways: Distinguishable yet phase-coherent mixtures of Bose-Einstein condensates. J. Low Temp. Phys., 113(3/4):151, 1998.

[65] K. L. Corwin, Z.-T. Lu, C. F. Hand, R. J. Epstein, and C. E. Wieman. Frequency-stabilized diode laser with the zeeman shift in an atomic vapor. Appl. Opt., 37:3295, May 1998.

[66] M. Cozzini and S. Stringari. cond-mat/0211294.

[67] M. Cozzini and S. Stringari. to be published.

[68] F. Dalfovo and S. Stringari. Shape deformations and angular-momentum transfer in trapped Bose-Einstein condensates. Phys. Rev. A, 63:011601 (R), December 2000.

[69] Franco Dalfovo, Stefano Giorgini, Lev P. Pitaevskii, and Sandro Stringari. Theory of Bose-Einstein condensation in trapped gases. Rev. Mod. Phys., 71(3):463, April 1999.

[70] Franco Dalfovo and Michele Modugno. Free expansion of Bose-Einstein condensates with quantized vortices. Phys. Rev. A, 61:023605, January 2000.

[71] Diego A. R. Dalvit, Jacek Dziarmaga, and Roberto Onofrio. Measurement-induced squeezing of a Bose-Einstein condensate. Phys. Rev. A, 65:033620, February 2002.

[72] Wolfgang Demtröder. Laser Spectroscopy. Springer, 1981.

[73] J. Denschlag, J.E. Simsarian, D.L. Feder, Charles W. Clark, L.A. Collins, J. Cubizolles, L. Deng, E.W. Hagley, K. Helmerson, W.P. Reinhardt, S.L. Rolston, B.I. Schneider, and W.D. Phillips. Generating solitons by phase engineering of a Bose-Einstein condensate. Science, 287:97, January 2000.

[74] R. Donnelly. Quantized vortices in helium II. University Press, Cambridge, 1991.

[75] Z. Dutton, M. Budde, C. Slowe, and L. V. Hau. Observation of quantum shock waves created with ultra- compressed slow light pulses in a Bose-Einstein condensate. Science, 293:663, June 2001.

[76] A. Einstein. Quantentheorie des einatomigen idealen Gases: Zweite Abhandlung. Sitzungber. Preuss. Akad. Wiss., 1925(0):3, January 1925.

[77] P. Engels, I. Coddington, P. C. Haljan, and E. A. Cornell. Nonequilibrium effects of anisotropic compression applied to vortex lattices in Bose-Einstein condensates. Phys. Rev. Lett., 89:100403, September 2002.

[78] Jason R. Ensher. The First Experiments with Bose-Einstein Condensation of ^{87}Rb. PhD thesis, University of Colorado (Boulder), 1998.

[79] David L. Feder and Charles W. Clark. Superfluid-to-solid crossover in a rotating Bose-Einstein condensate. Phys. Rev. Lett., 87(19):190401, November 2001.

[80] David L. Feder, Anatoly A. Svidzinsky, Alexander L. Fetter, and Charles W. Clark. Anomalous modes drive vortex dynamics in confined Bose-Einstein condensates. Phys. Rev. Lett., 86:564, January 2001.

[81] D.L. Feder, M.S. Pindzola, L.A. Collins, B.I. Schneider, and C.W. Clark. Dark-soliton states of Bose-Einstein condensates in anisotropic traps. Phys. Rev. A, 62:053606, October 2000.

[82] P.O. Fedichev and G.V. Shlyapnikov. Dissipative dynamics of a vortex state in a trapped Bose-condensed gas. Phys. Rev. A, 60(3):R1779, September 1999.

[83] A. L. Fetter and A. A. Svidzinsky. Vortices in a trapped dilute Bose-Einstein condensate. J. Phys.-Condens. Mat., 13(12):R135, March 2001.

[84] Alexander L. Fetter and John Dirk Walecka. Theoretical mechanics of particles and continua. McGraw-Hill, 1980.

[85] R. P. Feynman. Progress in Low Temperature Physics, ed. C. J. Gorter, vol. 1 ch. 2, Amsterdam:New Holland (1955).

[86] U. R. Fischer and G. Baym. condmat/0111443.

[87] Jr. G. A. Swartzlander and C. T. Law. Optical vortex solitons observed in Kerr nonlinear media. Phys. Rev. Lett., 69(17):2503, 1992.

[88] J.J. García-Ripoll, Gabriel Molina-Terriza, V.M. Pérez-García, and Lluis Torner. Structural instability of vortices in Bose-Einstein condensates. Phys. Rev. Lett., 87:140403, October 2001.

[89] J.J. García-Ripoll and V.M. Pérez-García. Vortex bending and tightly packed vortex lattices in Bose-Einstein condensates. Phys. Rev. A, 64:053611, October 2001.

[90] Juan J. García-Ripoll and Víctor M. Pérez-García. Stable and unstable vortices in multicomponent Bose-Einstein condensates. Phys. Rev. Lett., 84(19):4264, May 2000.

[91] C. Gardiner. unpublished.

[92] R. J. Gorndon and S. A. Rice. Active control of the dynamics of atoms and molecules. Anuu. Rev. Phys. Chem., 84:601, 1997.

[93] Markus Greiner, Olaf Mandel, Tilman Esslinger, Theodor W. Hänsch, and Immanuel Bloch. Quantum phase transition from a superfluid to a Mott insulator in a gas of ultracold atoms. Nature, 415:39, January 2002.

[94] D. Guéry-Odelin. Spinning up and down a Boltzmann gas. Phys. Rev. A, 62:033607, August 2000.

[95] D. Guéry-Odelin and S. Stringari. Scissors mode and superfluidity of a trapped Bose-Einstein condensed gas. Phys. Rev. Lett., 83(22):4452, November 1999.

[96] M. Guilleumas and R. Graham. Off-axis vortices in trapped Bose-condensed gases: Angular momentum and frequency splitting. Phys. Rev. A, 64:033607, September 2001.

[97] P. C. Haljan, I. Coddington, P. Engels, and E. A. Cornell. Driving Bose-Einstein-condensate vorticity with a rotating normal cloud. Phys. Rev. Lett., 87:210403, November 2001.

[98] P.C. Haljan, B.P. Anderson, I. Coddington, and E.A. Cornell. Use of surface-wave spectroscopy to characterize tilt modes of a vortex in a Bose-Einstein condensate. Phys. Rev. Lett., 86(14):2922, April 2001.

[99] D.S. Hall, M.R. Matthews, J.R. Ensher, C.E. Wieman, and E.A. Cornell. Dynamics of component separation in a binary mixture of Bose-Einstein condensates. Phys. Rev. Lett., 81(8):1539, August 1998.

[100] G. Hechenblaikner, E. Hodby, S. A. Hopkins, O. M. Marago, and C. J. Foot. Direct observation of irrotational flow and evidence of superfluidity in a rotating Bose-Einstein condensate. Phys. Rev. Lett., 88:070406, February 2002.

[101] T. L. Ho. Bose-Einstein condensates with large number of vortices. Phys. Rev. Lett., 87:060403, August 2001.

[102] Tin-Lun Ho and V.B. Shenoy. Binary mixtures of Bose condensates of alkali atoms. Phys. Rev. Lett., 77(16):3276, October 1996.

[103] E. Hodby, G. Heckenblaikner, S.A. Hopkins, O.M. Maragó, and C.J. Foot. Vortex nucleation in Bose-Einstein condensates in an oblate, purely magnetic potential. Phys. Rev. Lett., 88(1):010405, December 2001.

[104] S. Inouye, S. Gupta, T. Rosenband, A.P. Chikkatur, A. Görlitz, T.L. Gustavson, A.E. Leanhardt, D.E. Pritchard, and W. Ketterle. Observation of vortex phase singularities in Bose-Einstein condensates. Phys. Rev. Lett., 87(8):080402, August 2001.

[105] Tomoya Isoshima and Kazushige Machida. Bose-Einstein condensation in a confined geometry with and without a vortex. J. Phys. Soc. Jpn., 66(11):3502, November 1997.

[106] B. Jackson, J.F. McCann, and C.S. Adams. Vortex line and ring dynamics in trapped Bose-Einstein condensates. Phys. Rev. A, 61:013604, December 1999.

[107] B. Jackson, J.F. McCann, and C.S. Adams. Vortex rings and mutual drag in trapped Bose-Einstein condensates. Phys. Rev. A, 60(6):4882, December 1999.

[108] B. Jackson, J.F. McCann, and C.S. Adams. Dissipation and vortex creation in Bose-Einstein condensed gases. Phys. Rev. A, 61:051603(R), April 2000.

[109] D.S. Jin, J.R. Ensher, M.R. Matthews, C.E. Wieman, and E.A. Cornell. Collective excitations of a Bose-Einstein condensate in a dilute gas. Phys. Rev. Lett., 77(3):420, July 1996.

[110] C. A. Jones, S. J. Putterman, and P. H. Roberts. Stability of solitary wave solutions of nonlinear schrodinger-equations in 2 and 3 dimensions. J. Phys. A, 19(15):2991, October 1986.

[111] C. Josserand and Y. Pomeau. Generation of vortices in a model of superfluid he-4 by the kadomtsev-petviashvili instability. Europhys. Lett., 30(1):43, April 1995.

[112] Yuri S. Kivshar, Jason Christou, Vladimir Tikhonenko, Barry Luther-Davies, and Len M. Pismen. Dynamics of optical vortex solitons. Optics Communications, 152:198, 1998.

[113] L. D. Landau. J. Phys.(Moscow) **5**, 71 (1941).

[114] A.J. Leggett. Superfluidity. Rev. Mod. Phys., 71(2):S318, 1999.

[115] Fritz London. The λ-phenomenon of liquid helium and the Bose-Einstein degeneracy. Nature, 141(3571):643, April 1938.

[116] Emil Lundh and P. Ao. Hydrodynamic approach to vortex lifetimes in trapped Bose condensates. Phys. Rev. A, 61:063612, June 2000.

[117] K.W. Madison, F. Chevy, V. Bretin, and J. Dalibard. Stationary states of a rotating Bose-Einstein condensate: Routes to vortex nucleation. Phys. Rev. Lett., 86(20):4443, May 2001.

[118] K.W. Madison, F. Chevy, W. Wohlleben, and J. Dalibard. Vortex formation in a stirred Bose-Einstein condensate. Phys. Rev. Lett., 84(5):806, January 2000.

[119] O.M. Maragó, S.A. Hopkins, J. Arlt, E. Hodby, G. Heckenblaikner, and C.J. Foot. Observation of the scissors mode and evidence for superfluidity of a trapped Bose-Einstein condensed gas. Phys. Rev. Lett., 84(10):2056, March 2000.

[120] M. R. Matthews. Two-component Bose-Einstein Condensation. PhD thesis, University of Colorado (Boulder), 1999.

[121] M.R. Matthews, B.P. Anderson, P.C. Haljan, D.S. Hall, M.J. Holland, J.E. Williams, C.E. Wieman, and E.A. Cornell. Watching a superfluid untwist itself: Recurrence of Rabi oscillations in a Bose-Einstein condensate. Phys. Rev. Lett., 83(17):3358, October 1999.

[122] M.R. Matthews, B.P. Anderson, P.C. Haljan, D.S. Hall, C.E. Wieman, and E.A. Cornell. Vortices in a Bose-Einstein condensate. Phys. Rev. Lett., 83(13):2498, September 1999.

[123] S.A. McGee and M.J. Holland. Rotational dynamics of vortices in confined Bose-Einstein condensates. Phys. Rev. A, 63:043608, March 2001.

[124] Harold J. Metcalf and Peter van der Straten. Laser Cooling and Trapping. Springer, 1999.

[125] Gabriel Molina-Terriza, Jaume Recolons, Juan P. Torres, and Lluis Torner. Observation of the dynamical inversion of the topological charge of an optical vortex. Phys. Rev. Lett., 87:023902, July 2001.

[126] Olivier Morice, Yvan Castin, and Jean Dalibard. Refraction index of a dilute Bose gas. Phys. Rev. A, 51(5):3896, May 1995.

[127] E. J. Mueller and T.-L. Ho. cond-mat/0210276.

[128] C.J. Myatt, E.A. Burt, R.W. Ghrist, E.A. Cornell, and C.E. Wieman. Production of two overlapping Bose-Einstein condensates by sympathetic cooling. Phys. Rev. Lett., 78(4):586, January 1997.

[129] P. Noziéres and D. Pines. The Theory of Quantum Liquids, vol. II, volume 2. Addison-Wesley Publishing Co., 1990.

[130] R. Onofrio, C. Raman, J.M. Vogels, J.R. Abo-Shaeer, A.P. Chikkatur, and W. Ketterle. Observation of superfluid flow in a Bose-Einstein condensed gas. Phys. Rev. Lett., 85(11):2228, September 2000.

[131] L. Onsager. Nuovo Cimento **6** suppl **2**, 249 (1949).

[132] C. Orzel, A. K. Tuchman, M. L. Fenselau, M. Yasuda, and M. A. Kasevich. Squeezed states in a Bose-Einstein condensate. Science, 291:2386, March 2001.

[133] B. Paredes, P.O. Fedichev, J.I. Cirac, and P. Zoller. 1/2-Anyons in small atomic Bose-Einstein condensates. Phys. Rev. Lett., 87(1):010402, July 2001.

[134] A. A. Penckwitt, R. J. Ballagh, and C. W. Gardiner. condmat/0205037.

[135] Víctor M. Pérez-García and Juan J. García-Ripoll. Two-mode theory of vortex stability in multicomponent Bose-Einstein condensates. Phys. Rev. A, 62:033601, August 2000.

[136] Wolfgang Petrich, Michael H. Anderson, Jason R. Ensher, and Eric A. Cornell. Stable, tightly confining magnetic trap for evaporative cooling of neutral atoms. Phys. Rev. Lett., 74(17):3352, April 1995.

[137] H. Pu and N.P. Bigelow. Collective excitations, metastability, and nonlinear response of a trapped two-species Bose-Einstein condensate. Phys. Rev. Lett., 80(6):1134, February 1998.

[138] C. Raman, J. R. Abo-Shaeer, J. M. Vogels, K. Xu, and W. Ketterle. Vortex nucleation in a stirred Bose-Einstein condensate. Phys. Rev, Lett., 87:210402, November 2001.

[139] G.W. Rayfield and F. Reif. Quantized vortex rings in superfluid helium. Phys. Rev., 136(5A):A1194, November 1964.

[140] William P. Reinhardt and Charles W. Clark. Soliton dynamics in the collisions of Bose-Einstein condensates: an analogue of the Josephson effect. J. Phys. B, 30(0):L785, 1997.

[141] D.S. Rokhsar. Vortex stability and persistent currents in trapped Bose gases. Phys. Rev. Lett., 79(12):2164, September 1997.

[142] P. Rosenbusch, V. Bretin, and J. Dalibard. Dynamics of a single vortex line in a Bose-Einstein condensate. Phys. Rev. Lett., 89:200403, November 2002.

[143] B.E.A Saleh and M.C. Teich. Fundamentals of Photonics. John Wiley & Sons, 1991.

[144] Anthony E. Siegman. Lasers. University Science Books, 1986.

[145] T.P. Simula, S. M. M. Virtanen, and M.M. Salomaa. Stability of multiquantum vortices in dilute Bose-Einstein condensation. Phys. Rev. A, 65:033614, February 2002.

[146] Jairo Sinova, C. B. Hanna, and A. H. MacDonald. Quantum melting and absence of Bose-Einstein condensation in two-dimensional vortex matter. Phys. Rev. Lett., 89:030403, July 2002.

[147] Dmitry V. Skryabin. Instabilities of vortices in a binary mixture of trapped Bose-Einstein condensates: Role of collective excitations with positive and negative energies. Phys. Rev. A, 63:013602, December 2000.

[148] S. Stringari. Collective excitations of a trapped Bose-condensed gas. Phys. Rev. Lett., 77(12):2360, September 1996.

[149] S. Stringari. Phase diagram of quantized vortices in a trapped Bose-Einstein condensed gas. Phys. Rev. Lett., 82(22):4371, May 1999.

[150] S. Stringari. Superfluid gyroscope with cold atomic gases. Phys. Rev. Lett., 86(21):4725, May 2001.

[151] Anatoly A. Svidzinsky and Alexander L. Fetter. Dynamics of a vortex in a trapped Bose-Einstein condensate. Phys. Rev. A, 62:063617, December 2000.

[152] Anatoly A. Svidzinsky and Alexander L. Fetter. Stability of a vortex in a trapped Bose-Einstein condensate. Phys. Rev. Lett., 84(26):5919, June 2000.

[153] J. Tempere, F. Brosens, L.F. Lemmens, and J.T. Devreese. Condensation and interaction range in harmonic boson traps: A variational approach. Phys. Rev. A, 61:043605, March 2000.

[154] D. J. Thouless, Ping Ao, Qian Niu, M. R. Geller, and C. Wexler. Quantized vortices in superfluids and superconductors. Int. J. Mod. Phys. B, 13(5/6):675, 1999.

[155] D. R. Tilley and J. Tilley. Superfluidity and superconductivity, 3rd ed. IOP Publishing Ltd, 1990.

[156] W. F. Vinen. Proc. R. Soc. A, 260:218, 1961.

[157] T. C. Weinacht, J. Ahn, and P. H. Bucksbaum. Controlling the shape of a quantum wavefunction. Nature, 397:233, January 1999.

[158] J. E. Williams, E. Zaremba, B. Jackson, T. Nikuni, and A. Griffin. Dynamical instability of a condensate induced by a rotating thermal gas. Phys. Rev. Lett., 88:070401, January 2002.

[159] J.E. Williams and M.J. Holland. Preparing topological states of a Bose-Einstein condensate. Nature, 401:568, October 1999.

[160] E. J. Yarmchuk, M. J. V. Gordon, and R. E. Packard. Observation of stationary vortex arrays in rotating superfluid helium. Phys. Rev. Lett., 43:214, July 1979.

[161] Francesca Zambelli and Sandro Stringari. Quantized vortices and collective oscillations of a trapped Bose-Einstein condensate. Phys. Rev. Lett., 81(9):1754, August 1998.

[162] O.N. Zhuravlev, A.E. Muryshev, and P.O. Fedichev. Dissipative dynamics of vortex arrays in anisotropic traps. Phys. Rev. A, 64:053601, October 2001.